
Characterization of Gravity Waves in the Lee of the Southern Andes utilizing an Autonomous Rayleigh Lidar System

Robert Jaroslav Reichert



München 2022

Characterization of Gravity Waves in the Lee of the Southern Andes utilizing an Autonomous Rayleigh Lidar System

Robert Jaroslav Reichert

Dissertation
an der Fakultät der Physik
der Ludwig-Maximilians-Universität
München

vorgelegt von
Robert Jaroslav Reichert
aus Hamburg

München, den 20. Dezember 2021

Erstgutachter: Prof. Dr. Markus Rapp

Zweitgutachter: Prof. Dr. Franz-Josef Lübken

Tag der mündlichen Prüfung: 18. März 2022

Wir stehen selbst enttäuscht und sehen betroffen
Den Vorhang zu und alle Fragen offen.
- BERTOLT BRECHT (1898 – 1956)

Contents

Zusammenfassung	ix
Abstract	x
1 Introduction	1
1.1 Vertical Temperature Structure of the Atmosphere	2
1.2 Waves in the Atmosphere	5
1.3 Previous Measurements at the Southern Andes Gravity Wave Hotspot	6
1.4 Thesis Objectives and Outline	10
2 Temperature Measurements in the Middle Atmosphere	13
2.1 Lidar Principle	13
2.1.1 The Compact Rayleigh Autonomous Lidar	15
2.1.2 Temperature Retrieval	17
2.2 CORAL Data Set	19
2.2.1 Nightly Mean Temperature Profiles	20
2.2.2 Monthly Mean Temperature Profiles	21
3 Atmospheric Temperature Background	25
3.1 Theory and Methods	27
3.1.1 Seasonal Oscillations	27
3.1.2 Planetary Waves and Tides	27
3.2 Results	39
3.2.1 Amplitudes and Phases of Diurnal Tides	39
3.2.2 Planetary Wave Disturbances	39
3.2.3 Amplitudes and Phases of Seasonal Oscillations	40
3.3 Discussion	44
3.3.1 Diurnal Tides	44
3.3.2 Semi-diurnal Tides	44
3.3.3 Stationary Wave-1	45
3.3.4 Seasonal Oscillations	45
3.4 Summary and Answer to Research Question (R1)	48
4 Internal Gravity Waves	51
4.1 Linear Gravity Wave Theory and Methods	52
4.1.1 Dispersion Relation	52

4.1.2	Phase and Group Velocity	54
4.1.3	Gravity Wave Potential Energy	55
4.1.4	Conservation of GW Momentum	56
4.1.5	1D Wavelet transformation	58
4.1.6	2D Wavelet transformation	59
4.1.7	WAVELET-SCAN	60
4.1.8	2D Kernel Density Estimation	64
4.2	Results	65
4.2.1	Identification of Stationary and Apparently Upward and Downward Propagating Waves in Austral Winter	65
4.2.2	Distribution of Vertical Wavelengths	66
4.2.3	Seasonal Variation of Gravity Wave Potential Energy	68
4.2.4	Potential Energy as Function of Altitude	70
4.3	Discussion	74
4.3.1	Distribution of Vertical Wavelengths	74
4.3.2	Gravity Wave Activity in the Stratosphere	74
4.3.3	Gravity Wave Activity in the Mesosphere	76
4.3.4	Comparison of Wave Energies based on different Cutoffs	78
4.4	Summary and Answer to Research Question (R2)	83
5	Propagation of Hydrostatic Rotating Mountain Waves	85
5.1	Ray Theory	85
5.2	GROGRAT Simulations	86
5.2.1	Approximation of the Mountain Ridge of the Southern Andes	87
5.2.2	Initialization of Waves	88
5.2.3	Ray Analysis	90
5.3	Forcing of Mountain Waves and Subsequent Propagation	90
5.4	Horizontal Propagation of Quasi-Stationary Mountain Waves	94
5.5	Summary and Answer to Research Question (R3)	99
6	Conclusions and Outlook	101
A	CORAL's workflow	111
B	Testing of WAVELET-SCAN with artificial temperature data	113
C	Uncertainty calculations	115
	Bibliography	117
	Acknowledgement	133

Zusammenfassung

Die weltweit größten Gebirgswellen werden an den südlichen Anden angeregt, wo sie anschließend vertikal und horizontal ins Lee propagieren und dort in der mittleren Atmosphäre ihren Impuls auf den Grundstrom übertragen. Viele Fragen im Bezug auf Anregung, genaue Ausbreitung, Wechselwirkung und Dissipation dieser Wellen sind immer noch unbeantwortet. Aus diesem Grund wurde im Auftrag des DLR in Río Grande (53,7° S, 67,7° W), Argentinien, ein Rayleigh Lidarsystem installiert, das vertikale Temperaturprofile aufnimmt, um Schwerewellensignaturen zu detektieren. Die Analyse des Lidar-Datensatzes, der automatisiert zwischen November 2017 und Oktober 2020 erhoben wurde, ist der Kern dieser Doktorarbeit. Neu ist hierbei nicht nur die Messung an diesem geographischen Ort, sondern auch die hohe Kadenz der Messungen. Die Messabdeckung von durchschnittlich zwei Messungen innerhalb drei Nächten ermöglicht es einen Temperaturhintergrund zu definieren, der zeitliche Skalen von 9 Tagen bis hin zu einem Jahr und vertikale Skalen ab 15 km abdeckt. Zusätzlich werden tägliche Gezeiten aus den Nachtmessungen des Lidars mit einer neuen Methodik extrahiert, die zur Validierung auch auf Reanalyse-Daten des ECMWF angewandt wird. Der Vergleich zeigt gute Übereinstimmungen, wobei die Amplituden der täglichen Gezeit in den Lidardaten in der Mesosphäre größer sind und auch wesentlich stärker variieren als in den Reanalyse-Daten. Zudem führt Gezeiten-Aliasing wahrscheinlich zu unerwartet kleinen/großen Amplituden in den jährlichen/halbjährlichen Schwingungen.

Die untersuchten Wellenenergien sind die größten, die je in der Stratosphäre gemessen wurden und erreichen ein Sättigungslimit bei 60 km Höhe. Das Erreichen eines Sättigungslimits in derart niedrigen Höhen wurde so bisher nicht beobachtet und lässt darauf schließen, dass Wellen bereits mit sehr großen Amplituden erzeugt werden und auch während der vertikalen Propagation gute Wachstumsbedingungen vorfinden. In Zusammenhang mit der Sättigung steht auch eine beobachtete Abnahme der Schwerewellenintermittenz in der Mesosphäre. Die Entwicklung eines neuen spektralen Werkzeugs hilft bei der Bestimmung von Wellenlängen. Hierbei wird deutlich, dass etwa 50 % der Wellen vertikale Skalen von über 16,5 km aufweisen. Dies ist ein wichtiges Ergebnis, wenn man bedenkt, dass bisherige Lidar-Studien sich meist auf vertikale Wellenlängen <15 km fokussiert haben.

In Einzelfällen wird ein Energiezuwachs in der Stratosphäre beobachtet, der das erwartete exponentielle Wachstum übersteigt. Dies könnte ein Hinweis darauf sein, dass die Wellen horizontal durch das Beobachtungsvolumen des Lidars hindurch propagieren. Um die Propagation der Wellen zusammen mit ihrem Anregungsmechanismus zu untersuchen, wurde eine Raytracing-Studie durchgeführt. Es wird zum einen deutlich, dass gemessene Wellenenergien in der mittleren Atmosphäre in erster Linie von den Eigenschaften der Hintergrundatmosphäre abhängen und erst in zweiter Linie von der Stärke der Anregung. Zweitens hat sich herausgestellt, dass die Anregung die Ausbreitungsrichtung der Gebirgswellen definiert. Dreht der Wind mit der Höhe, kommt es verstärkt zu lateraler Ausbreitung teilweise über mehrere 100 km leewärts. Ein horizontaler Windgradient vermag dies durch Drehung des Wellenvektors nicht zu kompensieren. Dies ist ein wichtiges Ergebnis und sollte in zukünftigen Parametrisierungs-Schemata von Klimamodellen berücksichtigt werden.

Abstract

The largest mountain waves worldwide are excited at the southern Andes where they subsequently propagate vertically and horizontally downwind and transfer their momentum to the mean flow in the middle atmosphere. Many questions regarding excitation, exact propagation, interaction and dissipation of these waves are still unanswered. For this reason, a Rayleigh lidar system was installed on behalf of DLR at Río Grande (53.7° S, 67.7° W), Argentina, to record vertical temperature profiles, to detect gravity wave signatures. Analysis of the lidar data set, collected in an automated manner between November 2017 and October 2020, is the core of this dissertation. What is new here is not only the measurement at this geographic location, but also the high cadence of the measurements. The measurement coverage of an average of two measurements within three nights allows to define a temperature background, which covers temporal scales from 9 days up to one year and vertical scales from 15 km. In addition, diurnal tides are extracted from nighttime lidar measurements using a new methodology that is also applied to ECMWF reanalysis data for validation. The comparison shows good agreement, although the amplitudes of the diurnal tide in the lidar data are larger in the mesosphere and vary much more than in the reanalysis data. Tidal aliasing likely results in unexpected small/large amplitudes in the annual/semi-annual oscillations.

The wave energies studied are the largest ever measured in the stratosphere, reaching a saturation limit at 60 km altitude. Reaching a saturation limit at such low altitudes has not been observed before in that way and suggests that waves are already generated with very large amplitudes and also find good growth conditions during vertical propagation. Also related to saturation is an observed decrease in gravity wave intermittency in the mesosphere. The development of a new spectral tool helps in the determination of wavelengths. Here it becomes clear that about 50 % of the waves have vertical scales greater than 16,5 km. This is an important result considering that previous lidar studies have mostly focused on vertical wavelengths <15 km.

In isolated cases, energy growth in the stratosphere is observed to exceed the expected exponential growth. This may indicate that the waves are propagating horizontally through the lidar's observation volume. To investigate the propagation of the waves along with their excitation mechanism, a ray tracing study was carried out. It becomes clear, first, that measured wave energies in the middle atmosphere depend primarily on the properties of the background atmosphere and only secondarily on the strength of the forcing. Second, it has been found that the excitation defines the direction of propagation of the mountain waves. If the wind turns with altitude, lateral propagation occurs more strongly, sometimes leeward for several 100 km. A horizontal wind gradient is not able to compensate this by rotating the wave vector. This is an important result and should be considered in future parameterization schemes of climate models.

Publications

Parts of the results presented in this thesis have been published in the following peer-reviewed articles:

- **High-Cadence Lidar Observations of Temperature and Gravity Waves at the Southern Andes Hot Spot.**

Robert Reichert, Bernd Kaifler, Natalie Kaifler, Markus Rapp, Andreas Dörnbrack, Jose Luis Hormaechea,
Journal of Geophysical Research: Atmospheres, 126:e2021D034683, 2021,
doi: <https://doi.org/10.1029/2021JD034683>.

Sections **2.1.1**, **2.2**, **4.1.3 – 4.1.8**, and **4.2 – 4.4** of this thesis are literal excerpts of this paper.

- **SOUTHTRAC-GW: An Airborne Field Campaign to Explore Gravity Wave Dynamics at the World's Strongest Hotspot.**

Markus Rapp, Bernd Kaifler, Andreas Dörnbrack, Sonja Gisinger, Tyler Mixa, Robert Reichert, Natalie Kaifler, Stefanie Knobloch, Ramona Eckert, Norman Wildmann, Andreas Giez, Lukas Krasauskas, Peter Preusse, Markus Geldenhuys, Martin Riese, Wolfgang Woiwode, Felix Friedl-Vallon, Björn-Martin Sinnhuber, Alejandro de la Torre, Peter Alexander, Jose Luis Hormaechea, Diego Janches, Markus Garhammer, Jorge L. Chau, J. Federico Conte, Peter Hoor and Andreas Engel,
Bulletin of the American Meteorological Society, 102(4):E871–E893, 2021,
doi: <https://doi.org/10.1175/BAMS-D-20-0034.1>.

- **Retrieval of intrinsic mesospheric gravity wave parameters using lidar and airglow temperature and meteor radar wind data.**

Robert Reichert, Bernd Kaifler, Natalie Kaifler, Markus Rapp, Pierre-Dominique Pautet, Michael J. Taylor, Alexander Kozlovsky, Mark Lester and Rigel Kivi,
Atmospheric Measurement Techniques, 12(11):5997–6015, 2019,
doi: <https://doi.org/10.5194/amt-12-5997-2019>.

Parts of the presented results are submitted for publication:

- **Gravity Wave Driven Seasonal Variability of Temperature Differences between ECMWF IFS and Rayleigh Lidar Measurements in the Lee of the Southern Andes.**

Sonja Gisinger, Inna Polichtchouk, Andreas Dörnbrack, Robert Reichert, Bernd Kaifler, Natalie Kaifler, Markus Rapp, Irina Sandu,

Journal of Geophysical Research: Atmospheres,

doi: <https://doi.org/10.1002/essoar.10508969.1>.

Chapter 1

Introduction

We live at the bottom of an ocean of air (Walker, 2008). It surrounds our Earth protectively and contains the vital oxygen we breathe. To us, this ocean seems infinitely deep, but compared to the diameter of the Earth it is as thin as the top layer of an onion. This comparison illustrates the vulnerability of this ocean, which we call *atmosphere*. In recent decades, it has become increasingly clear that human activity is responsible for climatic changes on our planet. The overwhelming majority of scientific studies agree that the natural greenhouse effect has been amplified by the increased burning of fossil fuels and the subsequent emission of potent greenhouse gas CO₂ since the Industrial Revolution (e.g. Harries et al., 2001, Feldman et al., 2015, Zeebe et al., 2016). We are in a global *climate change*. To detect and mitigate tipping points early we must learn to understand the Earth system. To do this, scientists around the world are developing global numerical models whose outputs are regularly compared with measurements for validation. Long-term predictions of climate change for decades or centuries in advance are especially challenging as the numerical integration relies on an initial value problem, and the temporal evolutions of many parameters are unknown. Since these are very complex calculations that are already pushing the limits of modern high-performance computing, the resolution of the models is limited to coarse grids (Palmer and Stevens, 2019). Large-scale weather patterns can be predicted well in the short and medium range, but a short rain shower tends to take us by surprise (Bauer et al., 2021).

Once we leave the lower atmosphere and head upwards, dynamical processes are dominated by internal waves. Large-scale waves, whose spatial dimensions correspond to fractions of the Earth's circumference, can be predicted well by global circulation models, while small-scale ($\lambda_h = 10 \text{ km} - 1000 \text{ km}$) waves are rarely resolved and therefore must be parameterized. Internal waves with such horizontal wavelengths are called *gravity waves* (GW) because Earth's gravity is the acting restoring force. They can be excited by airflow over mountains, by convection, or in regions of large wind shear to name just a few sources (Fritts and Alexander, 2003). Their propagation occurs in space and time, depending strongly on the wind and thermal structure of the atmosphere. For example, horizontally short GWs excited by airflow over isolated islands are often reflected at a gradient in the thermal stability and become *trapped lee waves*, some of which can be seen in striped cloud patterns (see Fig. 1.1). Other parts of the GW spectrum can advance unhindered to high altitudes where they encounter unstable conditions that eventually

cause them to break, like ocean waves breaking on the beach. Here, at the end of their life cycle, they release their momentum and energy to the mean flow, altering the global circulation and temperature structure of the atmosphere.

1.1 Vertical Temperature Structure of the Atmosphere

The vertical temperature profile of the atmosphere depends strongly on latitude and season. [Figure 1.2](#) shows a temperature profile from the atmospheric reference model MSIS¹ for winter solstice at 67° N. The MSIS profile from Río Grande (54° S, 68° W), Argentina, on 31 May which is close to winter solstice at the southern hemisphere looks different. It becomes evident from both profiles that the atmosphere is generally not isothermal, but the temperature depends on latitude and altitude. Within the first 10 km above the ground the temperature decreases due to adiabatic cooling. This lowest layer of the atmosphere is called the *troposphere* and contains over 80 % of the atmosphere's mass ([Wallace and Hobbs, 2006](#)).

The *ozone layer* extends between 15 km and 35 km and heats up the atmosphere by the absorption of ultra-violet (UV) solar radiation ([Wallace and Hobbs, 2006](#)). The temperature increase results in enhanced thermal stability which is represented by the Brunt-Väisälä or buoyancy frequency

$$N = \sqrt{\frac{g}{T} \left(\frac{dT}{dz} + \frac{g}{c_p} \right)} > 0, \quad (1.1)$$

where T is temperature, z refers to altitude, g is acceleration due to Earth's gravity, and c_p is the heat capacity of dry air, respectively. This layer of enhanced stability is called the *stratosphere*, and the tropopause at its base confines convection and limits the exchange of trace gases such as water vapor. Convective instability occurs as soon as the temperature gradient becomes more negative than the dry adiabatic lapse rate $-g/c_p = -9.8 \text{ K km}^{-1}$. If that is the case, the atmosphere is no longer stably stratified, and overturning as well as subsequent turbulence take place until stability is restored. The stratosphere is followed by the *mesosphere* at an altitude of about 50 km (stratopause). Therein temperatures decrease again due to thermal emission from CO_2 and we find the coldest place in the temperature profile at about 90 km (mesopause). The polar summer mesopause is in fact the coldest place in the entire atmosphere where temperatures reach approximately 130 K ([Lübken, 1999](#)). In presence of water vapor, the low temperatures lead to the formation of thin ice clouds which have the illustrious name *noctilucent clouds* (e.g. [Fogle and Hawrwitz, 1966](#)).

The mesopause is followed by the *thermosphere* which exhibits rising temperatures with altitude due to absorption of extreme ultraviolet solar radiation ($\lambda < 242 \text{ nm}$). The lower thermosphere, mesosphere and stratosphere are commonly referred to as the *middle atmosphere*.

In addition to the MSIS profiles, [Figure 1.2](#) depicts a temperature sounding obtained by the COmpact Rayleigh Autonomous Lidar (CORAL) on 31 May 2018 at 04 UTC at Río

¹(Mass Spectrometer - Incoherent Scatter) Model of the Upper Atmosphere

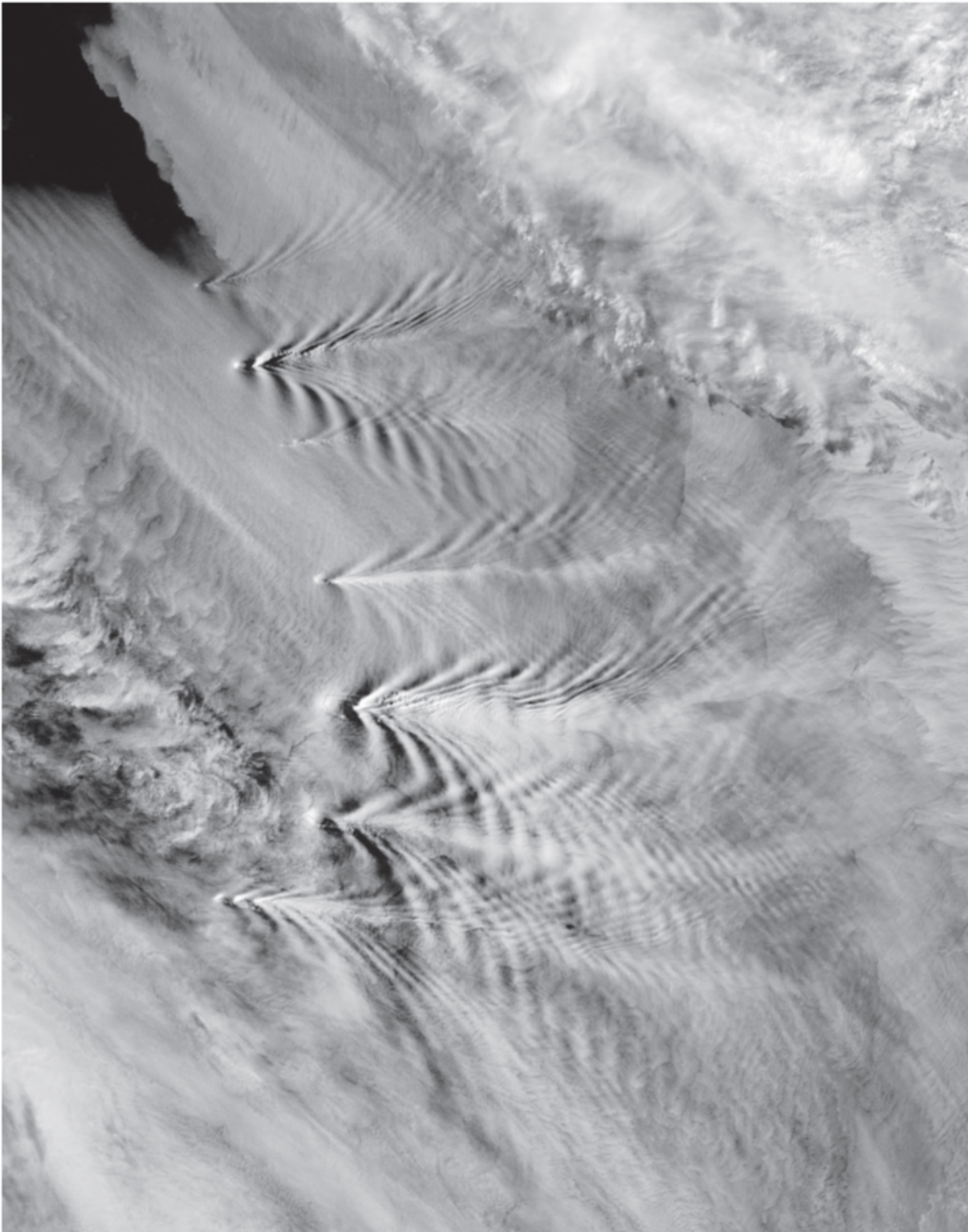


Figure 1.1: Trapped lee waves can be recognized in cloud patterns downstream the Sandwich Islands. The figure is taken from [Nappo \(2002\)](#).

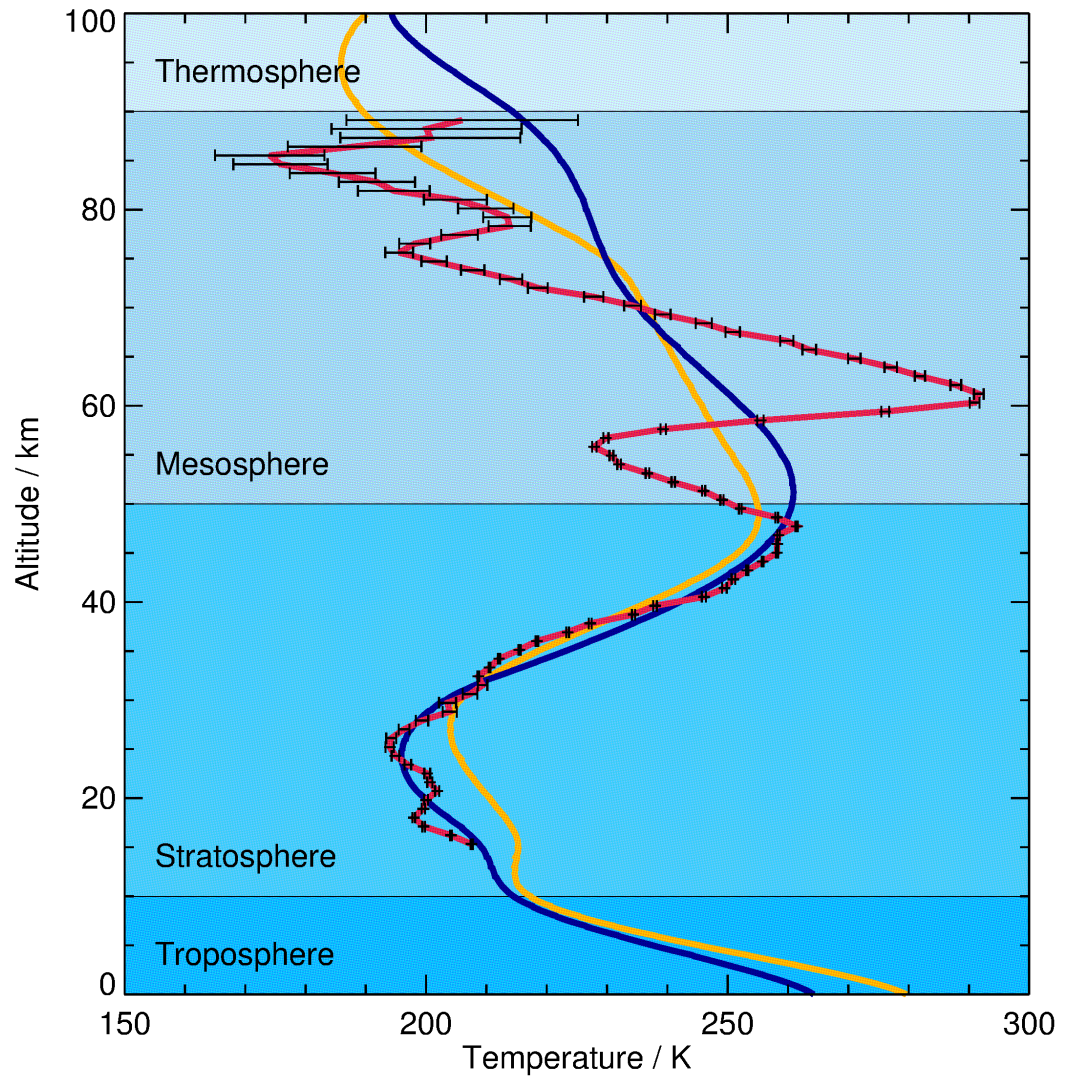


Figure 1.2: Two profiles from the atmospheric reference model MSIS depict the temperature for winter solstice at 67° N (blue) and for 31 May at 54° S (orange). The third temperature profile was measured by the CORAL lidar system at Río Grande (54° S, 68° W), Argentina, on 31 May 2018 at 04 UTC (red and black error bars).

Grande. The recorded profile roughly follows the MSIS profile from Río Grande, but shows a large variation with altitude, with temperature deviations of up to 40 K. In fact, temperature gradients above 60 km are close to the dry adiabatic lapse rate, indicating convective instability and therefore an atmosphere out of balance. These extreme temperature deviations are caused by dynamic processes, in particular wave motions.

1.2 Waves in the Atmosphere

Atmospheric wave motions can be classified based on their intrinsic frequency $\hat{\omega}$ and spatial extent. Waves with frequencies $\hat{\omega} < f$ - where f is the Coriolis frequency - and with horizontal wavelengths λ_h corresponding to a non-negligible fraction of the circumference of the Earth are called *planetary waves* (PW). They also represent eigenmodes of the atmosphere. They can be excited, for example, by orography and arise due to the conservation of vorticity which is linked to a meridional gradient in the Coriolis frequency. Under the right circumstances, these waves propagate up to the middle atmosphere, where they eventually break and decelerate the zonal circulation. Waves with periods of an integer fraction of a solar day, specifically 24 h, 12 h and 8 h are called *tides* (Chapman and Lindzen, 1970, Forbes et al., 1995). They arise primarily due to the absorption of solar radiation rather than due to gravity effects and have different properties depending on where they are excited. While PWs and tides appear on global scales, GWs are found on much smaller spatial scales (typically $\lambda_h < 1000$ km). They have frequencies in the range $N \gtrsim \hat{\omega} \gtrsim f$, i.e. their periods vary roughly between 5 min and 15 h at mid-latitudes. Long ($\lambda_h > 200$ km) GWs are well resolved in state of the art numerical weather prediction models (e.g. Ehard et al., 2017), but the effects of their shorter ($\lambda_h < 200$ km) counterparts need to be parameterized. However, it is of striking importance to capture the life cycle and effects of these shorter GWs as they carry the majority of energy and momentum (Nastrom and Fritts, 1992, Liu, 2019, Schumann, 2019).

GWs excited by airflow past orography are called *mountain waves* (MW) and are stationary above their sources as long as the excitation and propagation conditions remain steady and the waves remain linear (e.g. Queney, 1973, Schoeberl, 1985, Eckermann and Preusse, 1999, Nappo, 2002, Jiang et al., 2003). However, due to temporally as well as spatially variable atmospheric background conditions, MWs become transient and can be refracted and advected or end up as trapped waves. This can result in horizontal propagation extending up to thousands of kilometers (Dunkerton, 1984, Hills and Durran, 2012, Sato et al., 2012, Ehard et al., 2017, Portele et al., 2018, Dörnbrack, 2021). MWs can be sorted into different wave regimes which were derived initially by Queney (1948) and later named by Gill (1982). For this work, the most relevant ones are the rotating and nonrotating hydrostatic wave regimes. While nonrotating hydrostatic MWs have small horizontal scales (< 100 km) and propagate merely vertically (e.g. Hecht et al., 2018, Pautet et al., 2021), rotating hydrostatic MWs have large horizontal scales (> 100 km) and propagate also in the horizontal (e.g. Ehard et al., 2017). The vertical extent of MWs depends on the stratification and wind structure of the middle atmosphere. When their phase speed equals the horizontal wind speed, MWs reach a critical level, which causes them to break and thereby deposit their momentum on the background flow (Lindzen, 1981). This mo-

momentum deposition which is also known as GW drag contributes to the deceleration and ultimately to the reversal of the *polar night jet* (PNJ) enclosing the polar vortex (Teixeira, 2014) and drives the mesospheric circulation (Dunkerton, 1978).

The majority of observed modes excited by strong air flow across the Andean topography are MWs. During austral winter, favourable propagation conditions due to the prevailing stratospheric westerlies lead to exceptional large stratospheric GW momentum fluxes (GWMF) which are on average ten times larger than anywhere else on the globe (Hindley et al., 2020). The Southern Andes and also the Antarctic Peninsula are nowadays considered to be the strongest hotspot for stratospheric GWs in the world (Hoffmann et al., 2013). Downstream, a band of enhanced momentum flux extends all along 60° S (see Fig. 1.3). As this so-called *GW belt* is still not sufficiently reproduced by general circulation models (GCM), the models tend to overestimate the strength of the southern hemisphere polar vortex which ultimately leads to the *cold-pole problem* (e.g. Butchart et al., 2011, McLandress et al., 2012, Preusse et al., 2014). One of the reasons for this lack of wave activity in the models is that current parametrizations do not consider horizontal propagation of MWs (Preusse et al., 2002, Sato et al., 2009, 2012, Kalisch et al., 2014) but use a single column approximation. To better quantify the GW drag at the hotspot and downstream, MW generation at the Southern Andes and their subsequent propagation in the vertical and horizontal domain must be investigated.

1.3 Previous Measurements at the Southern Andes Gravity Wave Hotspot

GWs in the middle atmosphere over the Southern Andes have been the focus of multiple studies (e.g. Eckermann and Preusse, 1999, Preusse et al., 2002, Hoffmann et al., 2013, Hindley et al., 2015, Wright et al., 2016, 2017, Hindley et al., 2020). Recently, Hindley et al. (2020) have shown that the GW momentum flux points into a southwestward direction (see also Fig. 1.3), a result confirming previous momentum flux measurements by Wright et al. (2017). This indicates that MWs propagate meridionally towards the core of the stratospheric PNJ. These observations are confirmed by raytracing simulations and numerical modelling (Preusse et al., 2002, Sato et al., 2009, Jiang et al., 2013). The mechanism of a propagation that is more or less perpendicular to the prevailing wind direction is explained by Sato et al. (2012) and described as *lateral* or oblique propagation. It is this lateral propagation that is not considered by GCM. The raytracing study by Sato et al. (2012) and the earlier work by Dunkerton (1984) also show that meridional gradients in the zonal wind play an important role when it comes to the propagation of quasi-stationary MWs. A comprehensive overview over GW properties in the Southern Andes region is given by Wright et al. (2016), who found evidence for wave dissipation in the mid-stratosphere in summer and conservative, non-dissipative vertical propagation in winter.

The aforementioned observations are predominantly based on satellite data. Depending on the viewing geometry, the resolution is high in the vertical but coarse in the horizontal direction (limb soundings) or vice versa (nadir soundings) (Eckermann and Preusse, 1999, Ern et al., 2004, Alexander and Barnett, 2007, Alexander et al., 2008). Due to the ob-

1.3 Previous Measurements at the Southern Andes Gravity Wave Hotspot 7

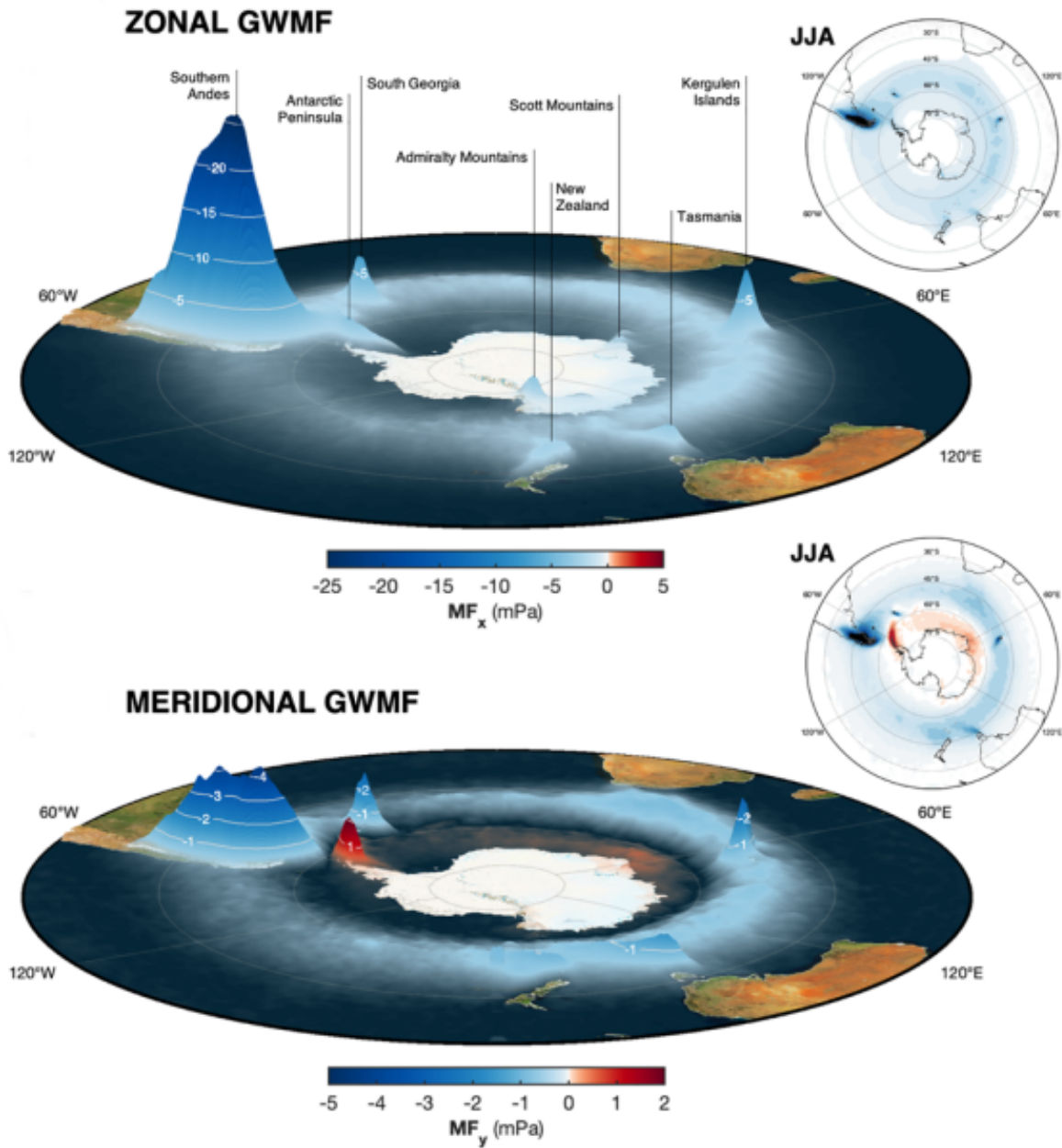


Figure 1.3: Stratospheric zonal and meridional GWMF are illustrated on top of a map of the southern hemisphere. GWMF is derived from Atmospheric Infrared Sounder (AIRS) measurements between 2002 and 2019. Illustrated is the average over the austral winter months June – August. The figure is taken from [Hindley et al. \(2020\)](#).

servation through various atmospheric layers, detected GW signatures are smoothed and amplitudes are damped. In addition, most polar-orbiting satellites only perform measurements twice a day above the same location and thus lack information on the temporal evolution of wave events. High-resolution long-term lidar measurements, such as those presented in this thesis, can capture both seasonal evolution and diurnal variability of GWs in the middle atmosphere that are not available from satellite measurements. In addition, the ground-based lidar measurements provide an ideal data set for comparison with the results of high-resolution numerical modeling (e.g. Ehard et al., 2017, Kaifler et al., 2020b).

The CORAL lidar system was deployed to the *Estación Astronómica Río Grande* (EARG) on Tierra del Fuego in late November 2017. CORAL is a transportable Rayleigh/Raman lidar which was utilized in previous campaigns in Finland (Kaifler et al., 2017, Reichert et al., 2019) and Germany (Kaifler et al., 2018). As part of the deployment to Río Grande, CORAL obtained measurements during the SOUTHTRAC-GW² airborne campaign and documented the evolution of the stratospheric temperature in 2019 (see Figure 6 in Rapp et al. (2021)). It was specifically designed for fully automatic observations of middle atmospheric temperature between 15 km and 100 km altitude. Since no operators are needed to run the instrument, it probes the atmosphere whenever the night sky is clear (Kaifler and Kaifler, 2020). For the first time, these high-cadence observations allow for the investigation of variations in temperature and GW activity in the middle atmosphere on a broad range of time scales, ranging from seasonal over day-to-day to hourly variations. Recently, Kaifler et al. (2020b) investigated a long-lasting large-amplitude MW event that CORAL observed in June 2018. They calculated momentum fluxes and GW drag, compared them to high-resolution ECMWF data, and found that the stratospheric circulation was significantly affected even far downwind. They concluded that 8% of the GW events occurring during winter are responsible for 30% of the total GW potential energy.

The GW potential energy can be derived from the lidar temperature measurements. The values depend primarily on the ratio between the temperature disturbances and the background as well as the stability. Multiple approaches exist in order to separate the atmospheric background from GW signatures (Whiteway and Carswell, 1995, Gardner and Taylor, 1998, Yamashita et al., 2009, Ehard et al., 2015, Baumgarten et al., 2017). All of these approaches have to redefine the temperature background from night to night as the measurement cadence is usually too low to take previous or subsequent measurements into account. The extremely high wind speeds in the southern hemispheric PNJ pose special challenges because they shift the spectrum of vertical scales of GWs and lead to greater overlap with tidal and PW spectra. A greater effort must be expended to cleanly separate GWs from a temperature background at the Southern Andes region. After all, the definition of the temperature background is crucial in order to derive realistic GW potential energies. The temporal as well as vertical evolution of GW potential energy contains information about the GW activity in general and, within certain limitations, regions of conservative propagation and of wave dissipation can be determined. Baumgaertner and McDonald (2007) report on log-normally distributed wave energies in the stratosphere with only a few events contributing large portions to the total energy. Here,

²Southern Hemisphere Transport, Dynamics, and Chemistry - Gravity Waves

1.3 Previous Measurements at the Southern Andes Gravity Wave Hotspot 9

the CORAL measurements are ideally suited to document the seasonal development of the energy spectra. Furthermore, due to the high temporal resolution of the CORAL data, the intermittency of GWs can be quantified.

If few GW events are responsible for the majority of the total GW energy, its frequency distribution becomes uneven. In this context, the community speaks of GW intermittency which describes the irregular occurrence of large-energy bursts that interrupt the dynamics of a periodic system (Strogatz, 1996). One measure to estimate GW intermittency is the Gini coefficient (Plougonven et al., 2013, Wright et al., 2013, Alexander et al., 2016, Minamihara et al., 2020). GW intermittency is an important parameter because it indicates the extent to which the GW momentum flux deviates from a continuous mean flux. Based on SABER measurements, Wright et al. (2013) have shown that the Gini coefficient is larger above the southern tip of South America than above the southern ocean but barely changes between 25 km and 65 km altitude.

1.4 Thesis Objectives and Outline

Until recently, there were no high-cadence ground-based lidar temperature measurements in the middle atmosphere above the southern tip of South America which is in fact a hotspot for stratospheric GWs in austral winter. The aim of this thesis is to characterize GWs in the lee of the Southern Andes utilizing an autonomous Rayleigh lidar system. In consideration of the previously mentioned wave regimes by [Queney \(1948\)](#) and [Gill \(1982\)](#) the hypothesis of this work is formulated as follows and illustrated in [Figure 1.4](#).

In the lee of the Southern Andes observed waves in austral winter are large-scale rotating hydrostatic mountain waves.

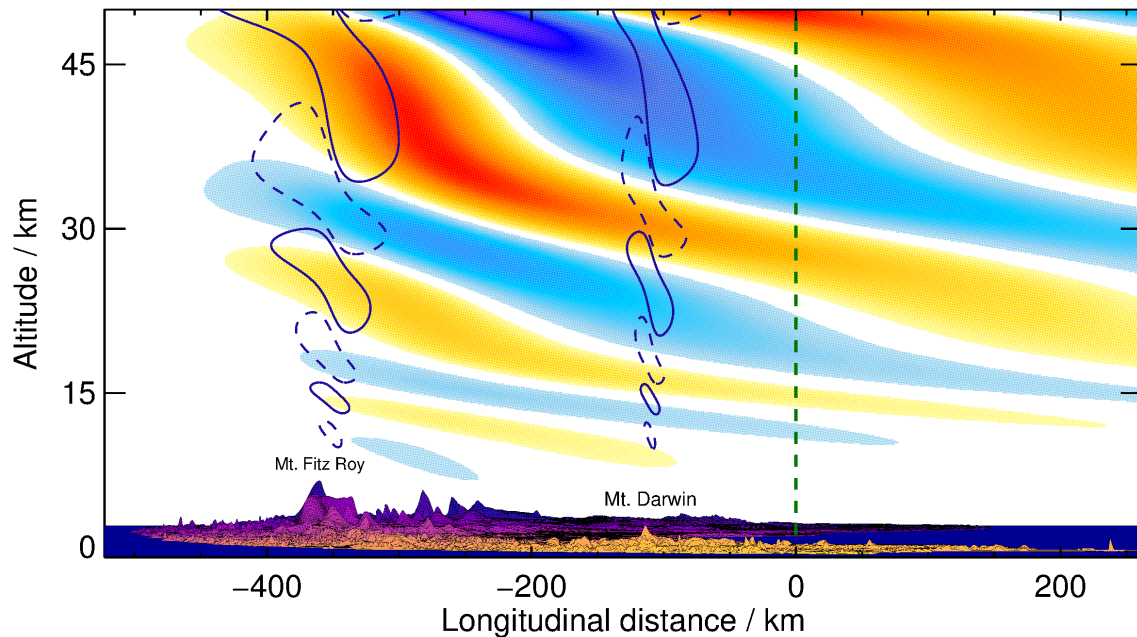


Figure 1.4: Depiction of MWs above the Southern Andes. The orange-purple colormap indicates latitudinal distance of the topography and the red-blue colormap symbolizes the wave field associated with hydrostatic rotating waves. Contour lines sketch wave fields associated with hydrostatic nonrotating waves. The green dashed line marks CORAL's laser beam at Río Grande. This figure is reproduced from ([Reichert et al., 2021](#)).

To approach the verification of the hypothesis, three research questions are posed, each answered in one chapter of this thesis. Usually, GW signatures are determined via the subtraction of a temperature background which is redefined from measurement to measurement. One objective of this thesis is the definition of a reasonable temperature background taking advantage of high-cadence lidar measurements.

(R1) Does the high cadence of CORAL measurements allow for the determination of planetary waves and tides in addition to annual and semi-annual oscillations and thus lead to better constraints on the temperature background?

So far, GWs at the Southern Andes were primarily investigated using space-borne instruments which have a limited resolution in time and in the vertical. The goals of the evaluations of the CORAL measurements are to investigate the GW potential energies, GW intermittency, and vertical wavelengths, which is summarized in the second research question.

(R2) What is the signature of the world's strongest stratospheric gravity wave hotspot in high-cadence CORAL temperature data?

As lidar measurements provide no information on horizontal wave structures, raytracing simulations are carried out to complement the analysis. A quantitative comparison between measured and modeled GW energies based on raytracing simulations has not yet been made. Significant differences could give conclusions on how much wave energies in linear wave theory deviate from realistic wave energies.

(R3) What are the forcing and propagation conditions of observed quasi-stationary mountain waves over Río Grande? How do the modelled gravity wave potential energies compare with the CORAL observations?

Chapter 2 gives an overview of the lidar technique and the specifications of the CORAL system. It is described how temperatures are retrieved from lidar measurements and middle atmospheric temperatures at Río Grande are presented in a climatological manner.

Please note that there is no preceding separate chapter on theory and methods, but chapters 3, 4, and 5 have sections on theory and methodology where needed.

In **Chapter 3** modes of temperature variability acting at longer times than GW periods are determined. Seasonal oscillations are identified and, subsequently, the theory behind planetary waves and tides is recalled. A running two dimensional fit is presented to extract planetary waves and tides from irregularly sampled lidar and regularly gridded ERA5 data, and results are shown. **(R1)**

Chapter 4 presents the analysis of GW potential energies and vertical wavelengths. Initially, the part of the linear GW theory that is most relevant for this work is recalled, and most emphasis is put on the distinction between the hydrostatic rotating and nonrotating wave regimes. The continuous wavelet transform is explained and the novel diagnostique technique WAVELET-SCAN is presented. **(R2)**

In **Chapter 5** the raytracing study that focuses on forcing and propagation conditions of MWs is presented. **(R3)**

Chapter 6 comes back to the central hypothesis posed for this thesis and summarizes the main conclusions of this work. Finally, an outlook for future studies is given.

Chapter 2

Temperature Measurements in the Middle Atmosphere

At the end of the 19th century, [Teisserenc de Bort \(1898\)](#) conducted the first temperature measurements in the middle atmosphere using balloon-sondes. Since then a variety of techniques on different platforms were employed to infer atmospheric variables like temperature. Some examples include rocket grenades ([Stroud et al., 1960](#)), falling spheres ([Lübken et al., 1996](#)), ionization gauges on sounding rockets ([Lübken et al., 1996](#), [Rapp et al., 2001](#)), microwave spectrometers on satellites ([Waters et al., 1975](#)), infrared sounders on satellites ([Remsberg et al., 2002](#)), and ground-based airglow imagers ([Pautet et al., 2014](#), e.g.). In 1980 the first ground-based lidar instrument was developed to perform temperature soundings in the middle atmosphere ([Hauchecorne and Chanin, 1980](#)). While lidar systems of the past filled entire buildings, technological advances, mostly regarding the development of lasers, allowed for the miniaturization of these instruments that can now be deployed on balloons ([Kaifler et al., 2020a](#)) or planes ([Fritts et al., 2016](#)) or built into transportable containers ([von Zahn and Höffner, 1996](#)) instead of permanent observatories. The advantage is that such a container can be shipped relatively easily and inexpensively to scientifically interesting locations around the world ([Kaifler and Kaifler, 2020](#)). CORAL is such a mobile system, and was used to obtain the temperature data set on which this work is based. The data set is a novelty in two respects. On the one hand, it is the first time that high-resolution temperature data are available at the southern tip of South America, covering an altitude range from the lower stratosphere up to the mesosphere/lower thermosphere (MLT). On the other hand, the autonomous operation results in a measurement cadence which is higher than for any other middle atmospheric lidar system. Before [Section 2.2](#) gives an overview of this unique data set, it is first described the general function of a lidar, the specifications of CORAL, and how atmospheric temperatures up to mesospheric altitudes are retrieved.

2.1 Lidar Principle

The idea to use very intense beams of light to investigate optical properties of the atmosphere at high altitudes is over 90 years old. In the 1930s, [Synge \(1930\)](#) described a system that would be capable of measuring atmospheric densities up to 30 km with an

accuracy of 1%. Such a system would comprise no less than 100 searchlights illuminating the night sky and a few parabolic mirrors to collect the backscattered light. The idea of *light detection and ranging* (lidar) was born. Within the same decade, the first experiments based on the described principle were conducted (Tuve et al., 1935, Hulburt, 1937). Photographs of the light beam confirmed the theory of molecular scattering and a layer of haze particles between 5 km and 10 km was identified. The breakthrough of the lidar technique came with the invention of the laser in the 1960s (Collis, 1965). Since then, the basic principle did not change. The lidar emits a short pulse of intense laser light and measures the time difference between the emission of the pulse and reception of the backscattered light to find the altitude z where the light was scattered. Nowadays, lidar is a well established tool and represents an active remote sensing technique similar to radar or sonar. The basic building blocks of a lidar are a transmitter and a receiver. The transmitter is a laser that emits a short pulse with power P_0 and with a temporal length τ_L in the order of a few nanoseconds into the atmosphere. The most common laser medium is Nd:YAG (neodymium-doped yttrium aluminium garnet; $\text{Nd:Y}_3\text{Al}_5\text{O}_{12}$) which emits laser light at a wavelength of 1064 nm. Depending on the application, the frequency can be doubled (532 nm) or tripled (355 nm). A telescope collects backscattered photons and focuses them into an optical fiber which guides the signal to the receiver box. Therein, the optical signal is filtered and converted into an electrical signal that is then digitized and recorded by a computer. Figure 2.1 illustrates the lidar principle.

The subsequent derivation is made essentially following Weitkamp (2006). The laser beam does not exit the laser medium perfectly parallel but exhibits an aperture angle or divergence Υ . The illuminated atmospheric volume V of the laser pulse is

$$V = \pi c \tau_L z^2 \left(\frac{\Upsilon}{2} \right)^2, \quad (2.1)$$

where c is the speed of light. To evaluate V , a volume integral in spherical coordinates is computed, in which the small angle approximation can be used since Υ is of the order of μrad , and the *effective (spatial) pulse length* is constrained by $\frac{c\tau_L}{2} \ll z$. The pulse intensity I_p is given by P_0 divided by the surface of a spherical cap with radius z , hence

$$I_p = \frac{P_0}{2\pi z^2 \left(\frac{\Upsilon}{2} \right)^2} e^{-\int_0^z \alpha_e(\tilde{z}) d\tilde{z}}, \quad (2.2)$$

where the integral represents the attenuation of light on its way from the point of emission to z (Lambert-Beer Law). α_e is the extinction coefficient. The total power that is scattered by the atmosphere volume illuminated by the pulse is

$$P_V = \beta' V I_p = P_0 \frac{c\tau_L}{2} \beta'(z) e^{-\int_0^z \alpha_e(\tilde{z}) d\tilde{z}} \quad (2.3)$$

where β' is the backscatter coefficient. The received intensity at the telescope is

$$I_r = \frac{P_V}{4\pi z^2} e^{-\int_0^z \alpha_e(\tilde{z}) d\tilde{z}}, \quad (2.4)$$

where, again, the integral represents the attenuation of light from the point of scattering down to the receiver. Considering the area of the telescope A , the received signal power

is

$$P_r = I_r A = P_0 \frac{c\tau_L}{2} \frac{A}{z^2} \frac{\beta'(z)}{4\pi} e^{-2 \int_0^z \alpha_e(\bar{z}) d\bar{z}}. \quad (2.5)$$

If the scattering is isotropic, then $\beta(z) = \frac{\beta'(z)}{4\pi}$ and the lidar equation is obtained:

$$P_r = I_r A = P_0 \frac{c\tau_L}{2} A \Gamma \frac{O(z)}{z^2} \beta(z) e^{-2 \int_0^z \alpha_e(\bar{z}) d\bar{z}}. \quad (2.6)$$

Additionally, Γ is introduced to account for the system efficiency and $O(z)$ represents the overlap function of the laser beam and the telescope's field of view (FOV). The lidar technique can be used to measure the concentration of aerosols, trace gases like ozone and water vapor (e.g. [Wirth et al., 2009](#)), and wind speeds can be derived by measuring the Doppler shift induced in the lidar return signal (e.g. [Reitebuch et al., 2009](#), [Baumgarten, 2010](#)). A general overview over a number of lidar techniques can be found in [Weitkamp \(2006\)](#). In the next section CORAL is described in more detail, which is the lidar system that acquired the temperature data used in this thesis.

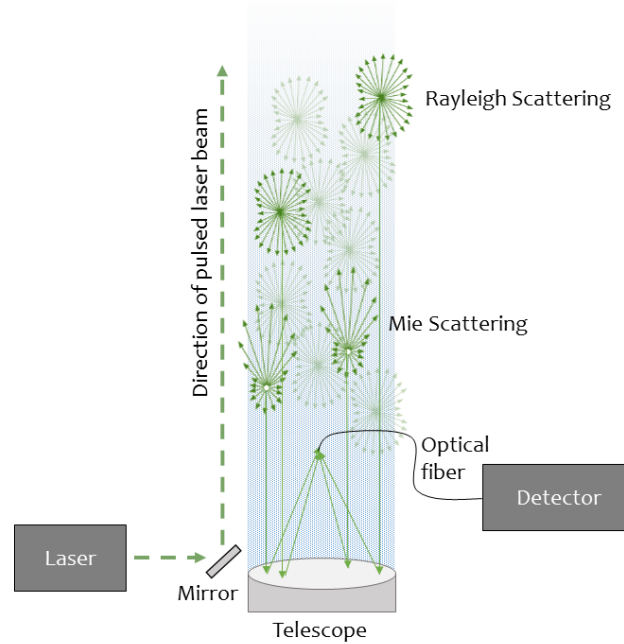


Figure 2.1: This Schematic illustrates the lidar principle. Pulses of intense laser light are shot in the atmosphere and there subject to Rayleigh scattering on air molecules. In the lower atmosphere, they are also susceptible to Mie scattering on aerosol particles. Backscattered photons are collected with a telescope and the signal is transferred to a detector.

2.1.1 The Compact Rayleigh Autonomous Lidar

The COmpact Rayleigh Autonomous Lidar (CORAL) is a ground-based Rayleigh/Raman backscatter lidar that was developed and built by the German Aerospace Center (DLR).

It conducted measurements in previous campaigns and has proven its reliability in terms of automatic operation and minimal maintenance (Kaifler et al., 2017, 2018, Reichert et al., 2019, Kaifler et al., 2020b). In November 2017 it was installed at the EARG (53.7° S, 67.7° W), Argentina. CORAL is the first fully automatic middle atmosphere lidar probing an altitude range from 15 km to approximately 90 km (Kaifler and Kaifler, 2020). Its autonomous operation results in a 3 – 8 times larger measurement cadence than any comparable human-operated lidar system. For cost reasons, CORAL does not have a daylight filter and is, therefore, only in operation in darkness and when weather conditions allow for it. The standard temperature data product has a resolution of 20 min and 900 m in time and altitude, respectively, but other resolutions can be produced in post-processing of the single-photon raw data.

Figure 2.2 shows the optical setup of CORAL. The lidar system uses a frequency doubled pulsed Nd:YAG laser as a light source with a pulse repetition rate of 100 Hz. Each laser pulse delivers an energy of 120 mJ at 532 nm wavelength. In order to decrease the aperture angle, the beam is expanded before its release into the atmosphere. The telescope with a diameter of 0.64 m and a FOV of $361 \mu\text{rad}$ focuses the collected light into an optical fiber which is positioned in the focal point of the parabolic mirror. Photons arriving in the receiver box at times corresponding to altitudes below 14 km are blocked by means of a chopper to protect the sensitive detectors. After the chopper, the collimated beam is spectrally divided using a dichroic mirror which separates the elastic scattering at 532 nm wavelength from the inelastic nitrogen vibrational Raman scattering at ~ 608 nm wavelength. The latter is filtered by a 3 nm wide interference filter and finally detected using a photomultiplier tube. The elastic Rayleigh scattering is split up by two subsequent beam splitters which have a transmission of 8% each. Therefore, the far channel receives 92.0%, the mid channel 7.4%, and the low channel 0.6% of the incident light. The mid and far channel detectors are avalanche photo diodes which are gated in order to limit count rates to about 5 MHz. Interference filters of 0.8 nm width are placed in front of both detectors. The low channel detector is again a photomultiplier with a 3 nm interference filter mounted in front.

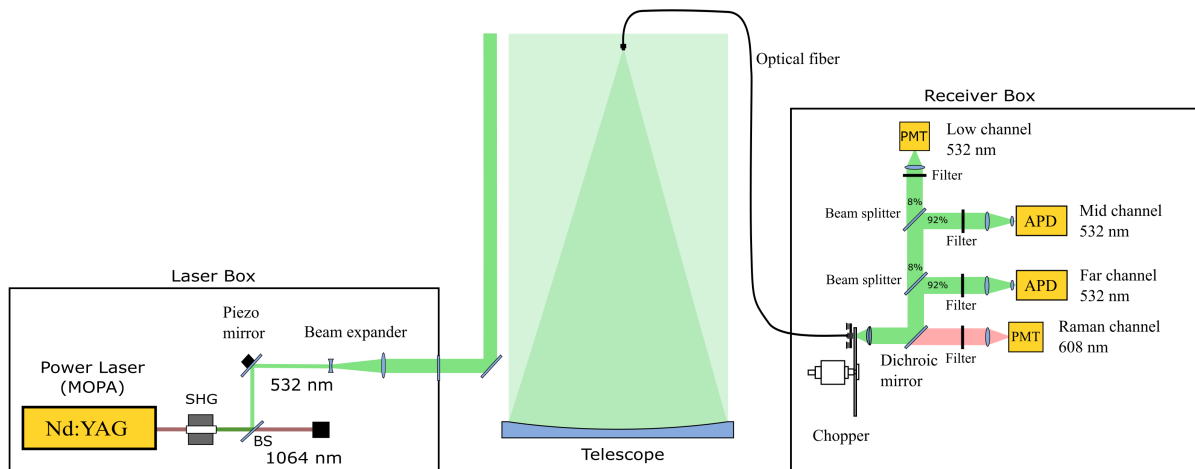


Figure 2.2: This is a schematic of the CORAL instrument and illustrates the optical paths. The figure is taken from Kaifler and Kaifler (2020). See text for details.

The CORAL system is mounted in an 8 ft steel container that provides all the infrastructure for operation and simplifies the transport of the lidar (Fig. 2.3a, b). The container has two access doors (I), one to enter the air-conditioned room that accommodates the transmitter, receiver, and data acquisition systems and one for the telescope room. Furthermore, two optical domes (II and III) are foreseen for installation of passive guest instruments like the Advanced Mesospheric Temperature Mapper (AMTM) (Pautet et al., 2014). One dome (III) accomodates an all-sky camera detecting stars and assessing sky conditions. Figure 2.3c shows the group of scientists that gathered in November 2017 at the EARG to install CORAL as well as the AMTM.

2.1.2 Temperature Retrieval

Following Behrendt (2005) (2.6) is reduced to

$$P_r(z) = C \frac{\theta(z)n_d(z)}{z^2}, \quad (2.7)$$

where C includes atmosphere and system parameters, $\theta(z)$ describes the atmospheric transmission and $n_d(z)$ is the number density of air molecules. From (2.7) it becomes evident that $P_r \sim n_d$. However, C is unknown and includes the extinction of the lidar signal due to aerosols and cloud droplets. The latter cause elastic Mie scattering as their size is of the same order or larger than the wavelength of the incident light. This is different from elastic Rayleigh scattering where the scattering particle is much smaller than the wavelength of the incident light. However, both scattering processes have in common that no energy is transferred such that the wavelengths of incident and backscattered light remain unaltered when Doppler-shifts are neglected. The difference between the two types of scattering is that Mie scattering takes place predominantly in the forward direction and additionally depends on the size and shape of the particle. Therefore, P_r is not directly proportional to n_d below ~ 30 km due to aerosols. However, the Raman channel detects only inelastic Raman scattering on nitrogen molecules which occurs three to four orders of magnitude less frequently than Rayleigh scattering due to the smaller scattering cross section. Due to the exponential decrease of atmospheric density, P_r decreases by one order of magnitude every ~ 16 km. Therefore, the return signal in the Raman channel from stratospheric altitudes is comparable with the return signal in the Rayleigh channel from mesospheric altitudes. The combination of Raman and Rayleigh channels is used to measure the profile of n_d , and thus reliable temperatures can be retrieved down to 15 km. Using the ideal gas law

$$p(z) = k_B n_d(z) T(z), \quad (2.8)$$

where p is pressure and k_B is the Boltzmann constant, and integrating the hydrostatic equation

$$\frac{dp}{dz} = -\varrho(z)g(z) \quad (2.9)$$

using $\varrho(z) = n_d(z)M$ and (2.7) leads to

$$T(z) = \frac{P_r(z_{\text{ref}})}{P_r(z)} \frac{z_{\text{ref}}^2}{z^2} T(z_{\text{ref}}) - \frac{M}{k_B} \int_{z_{\text{ref}}}^z \frac{\tilde{z}^2}{z^2} \frac{P_r(\tilde{z})}{P_r(z)} g(\tilde{z}) d\tilde{z}. \quad (2.10)$$

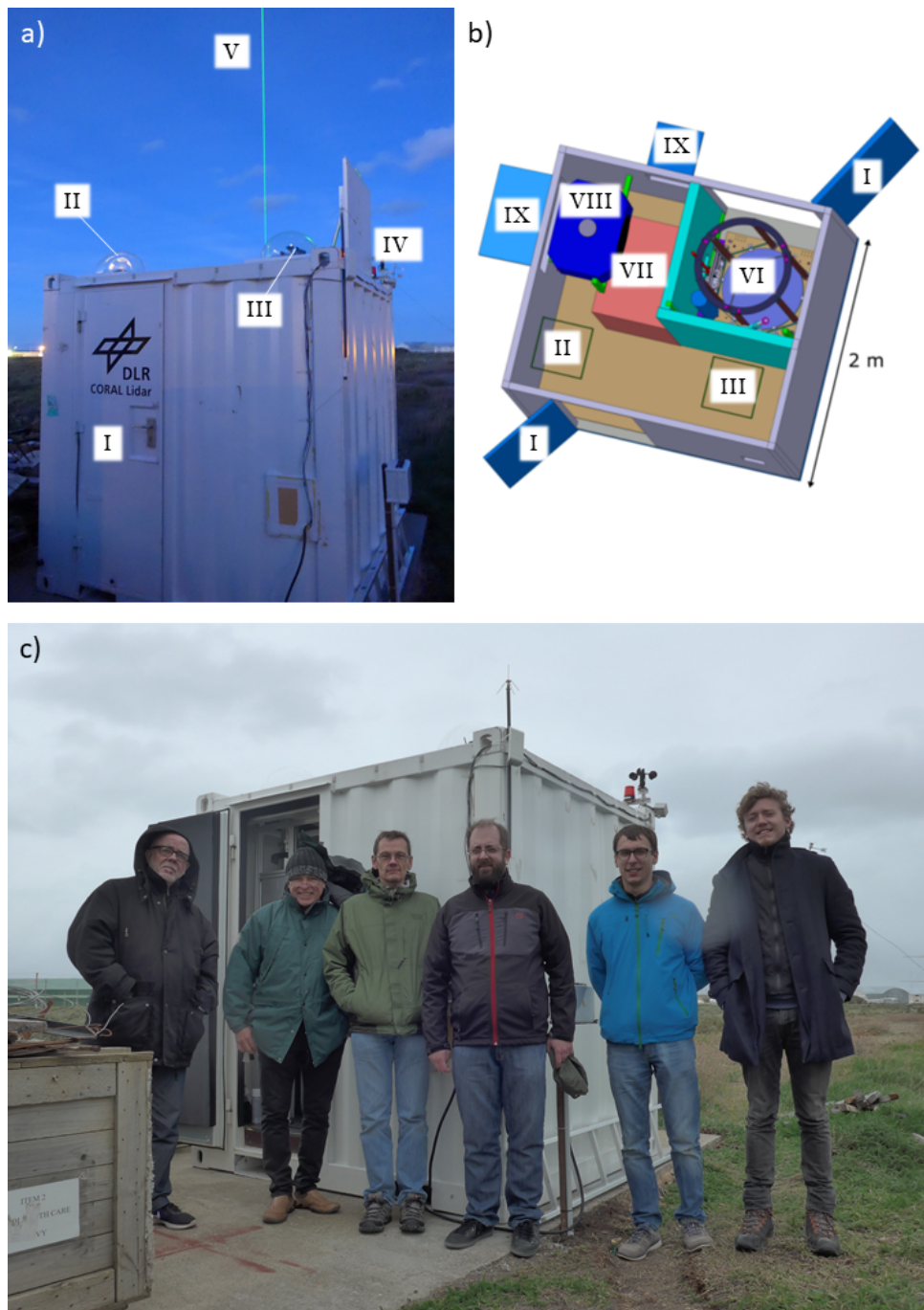


Figure 2.3: a) The front of the CORAL container is shown with access door to the operation room (I), optical dome for passive optical instrument (II), optical dome containing the all-sky camera (III), telescope hatch (IV) and laser beam (V). b) The drawing illustrates the interior of the CORAL container with access doors (I), slots for passive instruments (II and III), telescope (VI), lidar rack (VII), water chiller (VIII) and chiller hatches (IX). The figure is adapted from [Kaifler and Kaifler \(2020\)](#). c) From left to right: Alejandro de la Torre, Jose Luis Hormaechea, Pierre-Dominique Pautet, Jacobo Salvador, Bernd Kaifler and Robert Reichert after installation of CORAL and the AMTM in Río Grande in November 2017. Photographs by R. Reichert.

Here it is assumed that the atmospheric transmission is independent of altitude, which is a reasonable assumption in the middle atmosphere in the absence of strong absorption lines. It becomes clear that the temperature profile relies on the temperature at a reference altitude z_{ref} which is called seeding temperature. However, if the temperature profile is seeded at a high altitude and integrated from top to bottom, the first term in (2.10) loses significance for altitudes lower than 1 or 2 density scale heights below the seeding altitude, as the lidar signal increases exponentially with decreasing altitude. The same holds true for temperature uncertainties which decrease from top to bottom because of the increasing lidar signal. This procedure is first performed for the nightly average profile smoothed with a boxcar filter of ~ 2 km width and using co-located SABER¹ measurements as a seed value typically at 100 – 110 km altitude. Then, in an iterative manner, temperature profiles of subsequently higher resolutions of 120 min, 60 min, 30 min, 20 min, and 10 min are obtained by seeding at their top altitudes with the respective lower-resolution profiles.

2.2 CORAL Data Set

From 24 November 2017 to 20 October 2020, CORAL obtained 3042 hours of high-quality data. The duration of nightly measurements ranges from 1 h to a maximum of 15 h, the latter only being possible during long nights in winter. Runtime hours and number of measurement nights are listed for each month and year in Table 2.1. The maximum number of measurement hours per month was obtained in June 2018 with a total of 188 h and an average of 7.5 h per measurement night. The time between dusk and dawn (solar elevation angle $< -9^\circ$) is the potential run-time as CORAL lacks daylight filters and thus operates only in darkness. Measurements cover 42% of the potential run-time in June 2018. Between 16 June and 23 June 2018 a long lasting MW was nearly continuously observed (Kaifler et al., 2020b). The recording of such events demonstrates the advantage of autonomous lidar measurements as GW properties can be investigated over a larger period. In 2018 a maximum of 1124 h (31% of the potential run-time) was obtained within a total of 250 measurement nights, resulting in an average of 4.5 h per measurement night. The run-time in 2019 is with 24% lower compared to 2018 due to a 7-week-long downtime caused by technical issues. In 2020 CORAL collected even more data than in 2018 with on average 5.0 h per measurement night. In addition, it obtained record-high measurement durations from January to April as well as August and September.

Temperature profiles are provided with different temporal and vertical resolutions (see Reichert et al., 2019, Kaifler and Kaifler, 2020, for details). In the following analysis temperature data are used at 900 m vertical and 60 min time resolution computed on a grid of 100 m and 15 min. The annual average mean temperature precision in the altitude ranges 15 – 70 km and 70 – 100 km is 0.3 K and 4.2 K, respectively. The temperature errors include the effect of photon noise and are derived by performing Monte Carlo simulations (see (Kaifler and Kaifler, 2020, for details)).

¹Sounding of the Atmosphere using Broadband Emission Radiometry

Month/Year	2017	2018	2019	2020	total
Jan		18.0	36.8	43.8	98.6
		9	21	19	49
Feb		57.5	53.5	70.8	181.8
		17	20	24	61
Mar		91.0	83.8	108.8	283.6
		28	20	23	71
Apr		117.8	92.3	144.3	354.4
		22	20	28	70
May		151.8	174.5	142.3	468.6
		25	24	23	72
Jun		188.3	112.5	160.8	461.6
		25	19	25	69
Jul		154.0	82.0	153.5	389.5
		24	14	22	60
Aug		111.3	46.3	143.8	301.4
		23	8	27	58
Sep		86.5	-	101.0	168.5
		26	-	24	45
Oct		76.0	65.0	62.5	141.0
		19	19	15	38
Nov	5.8	37.0	64.8		107.6
	4	16	24		44
Dec	16.5	35.0	33.5		85.0
	9	16	17		42
total	22.3	1124.2	845.0	1050.1	3041.6
	13	250	206	210	679

Table 2.1: Runtime hours and number of nights with measurements for each month and year between 24 November 2017 and 20 October 2020. CORAL did not perform any measurements in September 2019 due to technical issues.

2.2.1 Nightly Mean Temperature Profiles

All nightly mean temperature profiles are displayed in [Figure 2.4](#). High concentrations of stratospheric aerosols caused by Australian bushfires prevented reliable temperature measurements in the lower stratosphere in austral fall 2020 ([Ohneiser et al., 2020](#)). Hence, a large portion of temperature data between 15 km and ~ 20 km in February and March 2020 had to be discarded. Only two further data gaps occurred due to technical issues with the instrument. The first appeared when a partial failure in the laser power supply caused a decrease in laser power, resulting in a reduced achievable maximum altitude from 18 August 2018 to 14 November 2018. The second period began on 14 August 2019 when a failed heating led to freezing coolant inside the laser and resulted in permanent damage. A replacement laser unit was shipped to R o Grande which took about six weeks. This data gap covers the period of the SOUTHTRAC-GW airborne campaign. The lidar

started operating again on 2 October 2019.

The summer temperature profiles (Nov – Feb) appear smooth and undisturbed in contrast to the winter profiles (Mar – Oct). The temperature maximum is considered to be the stratopause and the temperature minimum above 80 km to be the mesopause. In summer the stratopause is at approximately 50 km and the mesopause is at ~ 85 km. Sufficiently low temperatures in the summer mesopause have also led to the observation of a few noctilucent clouds which are not the subject of this work. The winter stratopause is cooler and elevated, migrating downwards at the end of winter. Winter profiles show larger night-to-night variability than summer profiles. The nightly mean profiles in [Figure 2.4](#) show annual oscillations at nearly all altitudes. These annual oscillations together with the less obvious semiannual oscillations are investigated and discussed in [Section 3.3.4](#).

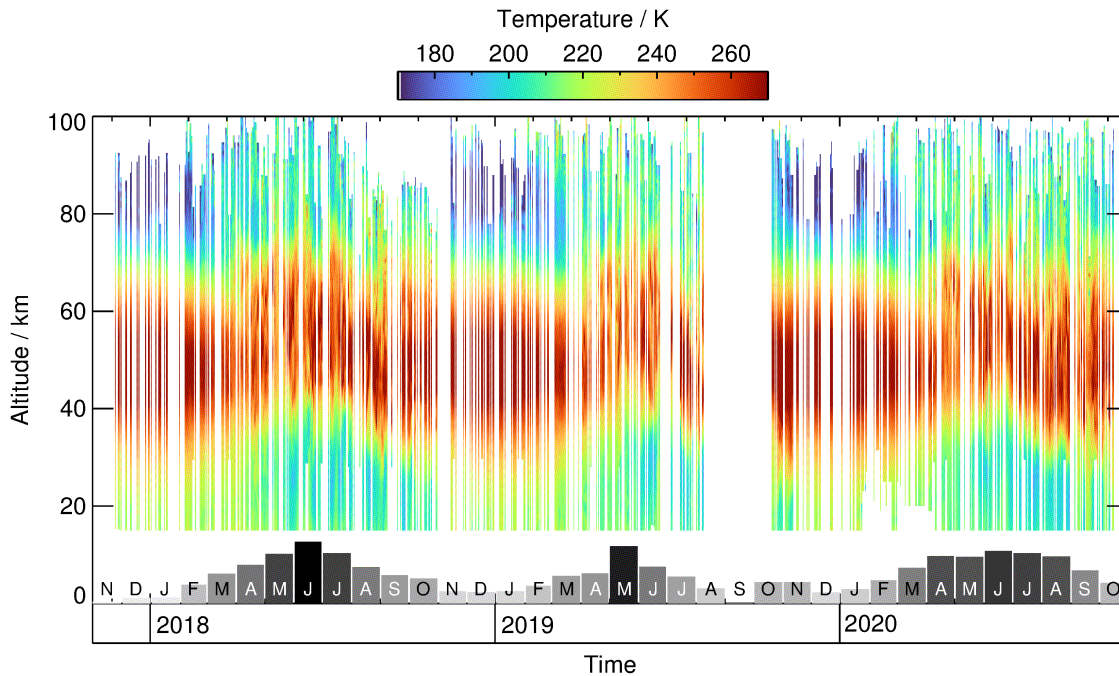


Figure 2.4: (t,z) -cross section of temperature T is illustrated. The cross section comprises all nightly mean temperature profiles obtained by CORAL from 24 November 2017 till 20 October 2020. White areas mark times and altitude regions where no temperatures were retrieved. Grey bars below indicate the monthly measurement duration in number of nights (see also [Tab. 2.1](#)).

2.2.2 Monthly Mean Temperature Profiles

The monthly mean temperature profiles provide a quantitative insight into the vertical temperature structure of the middle atmosphere above Río Grande. [Figure 2.5](#) shows monthly averages of nightly mean temperature profiles as well as corresponding standard deviations and temperature uncertainties. In addition, to highlight the extraordinary wave amplitudes, one measurement each winter month is shown exhibiting the largest

temperature deviation from the monthly mean. These profiles are called *extreme wave* profiles. Only measurements with at least 3 h duration are taken into account.

In the austral summer month of January, the stratopause is pronounced, with a maximum temperature of 275 K at 48 km altitude. The mesopause is located at ~ 85 km with a minimum mean temperature of 160 K. The standard deviation has a low value of 2.4 K between 15 km and 70 km, which indicates a dynamically quiet stratosphere and a lower mesosphere. A larger temporal variability is observed in the MLT, where the standard deviation between 70 km and 100 km increases to 10.3 K. Please note that temperature standard deviations are larger than temperature uncertainties at all altitudes. This illustrates that the temperature standard deviation is primarily influenced by atmospheric processes and not by uncertainties in the temperature retrieval.

From February to May, the stratopause cools from 275 K to 248 K and rises simultaneously from 48 km to 56 km. In the same period, the mesopause warms from 160 K to 200 K and rises from ~ 85 km to >100 km, i.e. to the top or even outside of the measurement range. While the mesopause in January and February is identified by a pronounced temperature minimum, a nearly isothermal region appears between 75 km and 100 km in March, April, and May. In the following months, a constant negative temperature gradient in the MLT suggests that the mesopause is located above 100 km as observed by e.g. [Gerding et al. \(2008\)](#) and [Yuan et al. \(2019\)](#) at mid-latitude northern hemisphere sites. Autumn temperature standard deviations increase to 6.7 K between 15 km and 70 km and remain constant at 10.6 K in the MLT.

In the following winter months, large average temperature standard deviations of 10.4 K are observed in the altitude range 15 – 70 km. From June to August a rapid increase can be seen in temperature standard deviation of ~ 10 K from the lower to the upper stratosphere ($\sim 30 - 40$ km). The upper stratosphere is most stably stratified, and the largest positive temperature gradients of up to 4.8 K km^{-1} are found in August. From August onwards, the observed developments reverse in time. Temperature standard deviations below 70 km decrease, and a pronounced mesopause establishes at ~ 85 km in November and gradually cools while the stratopause warms.

All extreme wave profiles in winter show a maximum deviation from the monthly mean on the order of 25 K to 55 K. The comparison with the adiabatic lapse rate ([Fig. 2.5](#)) suggests that the large negative temperature gradients occurring above the stratopause are limited by convective instability. By considering the position of maxima and minima, one can approximate the vertical wavelength of those extreme waves. It ranges from 10 km to 20 km.

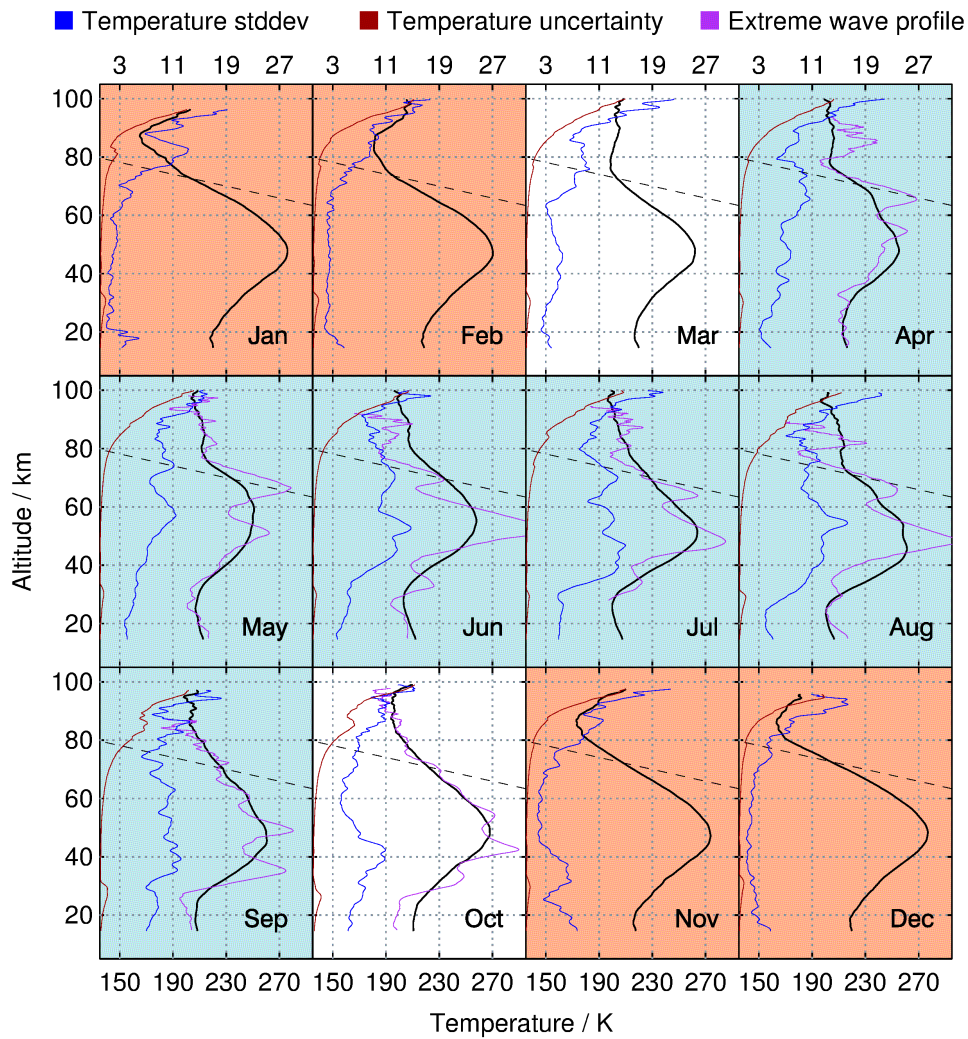


Figure 2.5: Monthly averages of nightly mean CORAL temperature profiles (black) and extreme wave profiles (purple) refer to the lower axis. Monthly averages of standard deviation of nightly mean temperature profiles (blue) and of nightly mean temperature uncertainty (red) refer to the upper axis. The profiles include data from November 2017 till October 2020. The adiabatic lapse rate is sketched as black dashed line. The blue background marks winter months, the red background summer months. See [Table 2.1](#) for the number of measurement hours.

Chapter 3

Atmospheric Temperature Background

The medium in which atmospheric internal GWs propagate is the atmosphere. Just as the propagation of light depends on the refractive index of e.g. glass, water, or air, the propagation of GWs depends on the refractive index of the atmosphere. The latter is essentially determined by the thermal stability and the background wind leading to reflection, ducting, refraction and focusing of GWs. Ultimately, wave breaking leads to the generation of turbulence via energy transport from large scales to small scales. Turbulence might interact in turn with a present wave field or serve as a source for new wave activity (Fritts and Alexander, 2003, and references therein).

Since CORAL's temperature data are obtained as function of time and height, these are the only dimensions that can be used to compute a temperature background and to distinguish GWs from it. GWs and background phenomena are assigned to their spatial and temporal scales in Figure 3.1. Please note that Figure 3.1 is just a schematic. Even though tides, PWs, and seasonal oscillations have predominantly mean vertical wavelengths longer than 30 km (Pancheva and Mukhtarov, 2011), their instantaneous (Huang et al., 2009) vertical wavelengths can also be shorter. Conversely, MWs exhibit mostly mean vertical wavelengths shorter than 20 km, but they may well have instantaneous vertical wavelengths longer than 30 km at the altitude of the PNJ core. With a conventional cutoff at 15 km, most of the high-pass signal can be safely considered as GWs. However, this might be different at latitudes below 45° (Rapp et al., 2018b). The low-pass background consists primarily of tides, PWs, and seasonal scillations. However, if the Butterworth cutoff is extended to 30 km, a non-negligible fraction of variance from tides, PWs, and seasonal oscillations leaks into the high-pass signal. This entire chapter is dedicated to the development of a method that accomplishes the extraction of the diurnal tide and PW signatures from the CORAL data set to reduce the leakage from background processes to GW signatures.

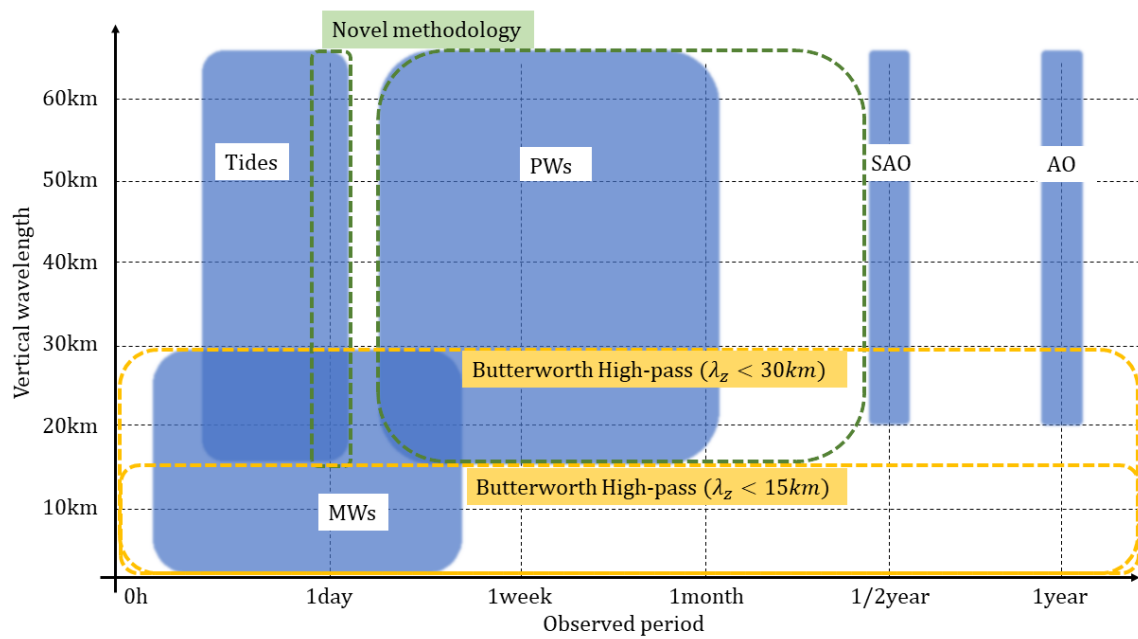


Figure 3.1: Depicted is a schematic of the wave scales that are accessible from lidar data. The blue areas show spectral coverages of different wave phenomena while the orange areas indicate the regions of the scales that are accessible via a Butterworth filter with cutoffs at 15 km and 30 km vertical wavelengths. The green areas mark the scales that are accessed using a novel methodology.

3.1 Theory and Methods

3.1.1 Seasonal Oscillations

While seasonal oscillations in the mesosphere arise due to the annual turn-over of the wave-driven meridional circulation, stratospheric seasonal oscillations result predominantly from the variability of solar radiation Q_s :

$$Q_s \propto D_h \sin(\phi) \sin(\delta) + \cos(\phi) \cos(\delta) \sin(D_h) \quad (3.1)$$

where $D_h = \arccos(-\tan(\phi) \tan(\delta))$ is the half-day length, ϕ is the latitude, and δ is the solar declination (Zdunkowski et al., 2007). The solar declination can be expressed as $\delta = -\epsilon \cos(\hat{\Omega}t + \xi)$ where $\epsilon = 23.44^\circ$ is the ecliptic, $\hat{\Omega}$ is the angular frequency of the Earth's rotation around the sun, and $\xi = 0.17$ is the phaseshift between winter solstice and the 1st of January. A Fourier analysis of (3.1) at the latitude of Río Grande reveals a dominant fundamental period of one year and additional higher harmonics with periods of integer fractions of one year that show less spectral power. Only the second harmonic with a period of half a year is of significant power. A terannual oscillation in middle atmospheric temperature was investigated by Gerding et al. (2008) at a northern hemisphere mid-latitude site and was claimed to be of negligible amplitude. Therefore seasonal oscillations in this work are modeled as a superposition of a constant background temperature \bar{T} , an annual oscillation (AO) with amplitude B_{AO} and phase τ_{AO} , and a semiannual oscillation (SAO) with amplitude B_{SAO} and phase τ_{SAO} . The fit function is defined as

$$T_{SO}(t) = \bar{T} + B_{AO} \cos(\hat{\Omega}(t - \tau_{AO})) + B_{SAO} \cos(2\hat{\Omega}(t - \tau_{SAO})). \quad (3.2)$$

The fit parameters \bar{T} , B_{AO} , B_{SAO} , τ_{AO} and τ_{SAO} are determined independently for each height in steps of 100 m.

Prior to the application of the least-square harmonic fit, a composite of the CORAL temperature data is computed by averaging nightly mean profiles with the same day of year. In addition, only those measurements are taken into account which are longer than 3 h in order to ensure that measurements are representative means. That way the influence of uncorrelated temperature variability, e.g. caused by PWs and GWs, is reduced. The results of this method are presented in Section 3.2.3.

3.1.2 Planetary Waves and Tides

After the subtraction of seasonal oscillations T_{SO} from CORAL's temperature data T , residuals with periods less than 180 days remain (see Figure 3.2). Sub-seasonal temperature perturbations are defined as

$$\tilde{T} = T - T_{SO}. \quad (3.3)$$

Signatures within \tilde{T} comprise PWs, tides, GWs, and other phenomena like sudden stratospheric warmings (SSW) or mesospheric inversion layers (MIL). In addition, zonal winds averaged between 30 km and 40 km are shown. The zonal winds are ERA5 reanalysis data

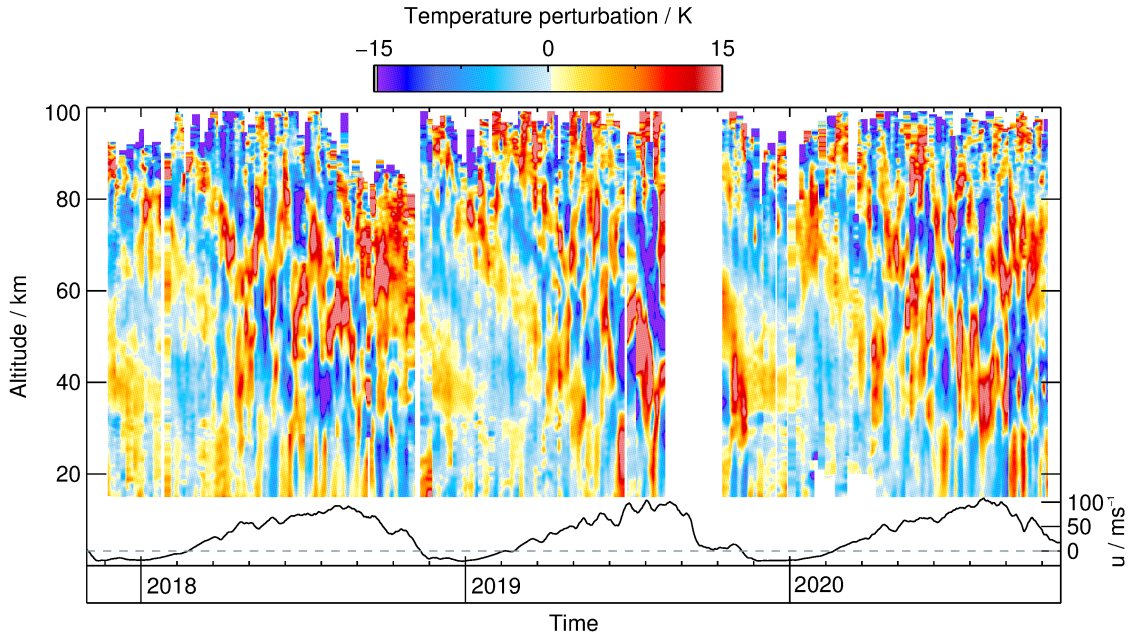


Figure 3.2: Illustrated is a (t, z) -cross section of sub-seasonal temperature perturbations \tilde{T} . To emphasize PW structures, \tilde{T} is Hann smoothed with a window length of 9 days. Bottom line depicts the average zonal wind from ERA5 truncated at wavenumber 21 between 30 km and 40 km.

taken from the ECMWF and are spectrally truncated at wavenumber T21 to remove the influence of small-scale disturbances like GWs. Large temperature disturbances are visible in the winter months and coincide with enhanced wind speeds. Also, a particularly large perturbation is found in mid August 2019 just before the occurrence of the extraordinary southern hemisphere SSW of 2019 (e.g. Dörnbrack et al., 2020, Rapp et al., 2021, and references therein).

What dynamical processes affect the thermal structure of the middle atmosphere on time scales < 180 days? The answer will certainly comprise GWs, but for now waves of larger scales shall be in the focus. The next pages give an outline of the theory behind global scale resonances of the atmosphere. We will see that the atmosphere exhibits a number of dominant eigenmodes which can be separated in tides, i.e. oscillations with periods of an integer fraction of a solar day and PWs with periods of multiple days. Information about diurnal tides will be extracted with a novel running two dimensional fit. Results of the novel method are discussed in the last part of this section.

Following Forbes et al. (1995), the linearized equations for perturbations on a spherical

isothermal atmosphere can be written as

$$\frac{\partial u}{\partial t} - fv + \frac{1}{a \cos(\phi)} \frac{\partial \Phi}{\partial \lambda} = 0 \quad (3.4)$$

$$\frac{\partial v}{\partial t} + fu + \frac{1}{a} \frac{\partial \Phi}{\partial \phi} = 0 \quad (3.5)$$

$$\frac{\partial}{\partial t} \Phi_z + N^2 w = \frac{\kappa J}{H_s} \quad (3.6)$$

$$\frac{1}{a \cos(\phi)} \left(\frac{\partial u}{\partial \lambda} + \frac{\partial}{\partial \phi} (v \cos(\phi)) \right) + \frac{1}{\varrho_0} \frac{\partial}{\partial z} (\varrho_0 w) = 0 \quad (3.7)$$

where the vector $\vec{u} = (u, v, w)^T$ defines wind speed in Cartesian coordinates $\vec{x} = (x, y, z)^T$, Φ is the perturbation geopotential, ϱ_0 is the background density that only depends on altitude, λ is the longitude, $\kappa = R/c_p \approx 2/7$, where R is the universal gas constant and J is the heating per unit mass, a is the radius of the Earth, and H_s is the scale height. Perturbations are assumed to consist of longitudinally propagating waves, i.e.

$$\{u, v, w, \Phi\} = \{\hat{u}, \hat{v}, \hat{w}, \hat{\Phi}\} e^{i(s\lambda - \sigma t)} \quad (3.8)$$

where the amplitudes $\{\hat{u}, \hat{v}, \hat{w}, \hat{\Phi}\}$ are functions of longitude and altitude. The zonal wavenumber s is a positive integer and refers to the number of oscillations along a constant latitude. Negative values of the angular frequency σ refer to westward propagating waves while positive values represent eastward propagating waves. If (3.8) is substituted in (3.4) – (3.7), one single second-order partial differential equation for Φ in z and ϕ is obtained. The ansatz then is to separate $\hat{\Phi}$ and write it as a sum of two functions, one that depends only on ϕ and one that depends only on z . Both functions represent a complete orthogonal set and can be solved via the horizontal and vertical structure equations. The former is better known as *Laplace's tidal equation*. The exact formalism is not recalled here as it is not in the focus of this work. The equations governing atmospheric perturbations are finally formulated as an eigenfunction-eigenvalue problem with h_n being the eigenvalue which is called *equivalent depth*. Another way to express the eigenvalue is $\varepsilon_n \approx 88 \text{ km}/h_n$. Generally, the vertical structure equation can be solved with a wave ansatz. There are two conceptually different solutions in case of a present forcing. First, if $h_n < 0$ or $h_n > 4\kappa H$ the wave degenerates to an evanescent mode where the oscillation is trapped in the altitude region of the forcing. Second, if $0 < h_n < 4\kappa H$ then the wave refers to a propagating mode i.e. energy transport away from the source region.

The eigenfunctions of Laplace's tidal equation are called Hough functions and, together with their eigenvalues, refer to a mode. Each mode is expressed as (s, n) where n is the meridional index which refers to the number of nodes of the eigenfunction in the meridional direction. The modes are classified into gravity modes (Class I) and PW or Rossby modes (Class II). Gravity modes always propagate with a finite vertical wavelength either westward or eastward. Their eigenvalues ε_n^s are always positive (for $s = 1$ see Fig. 3.3). A modal decomposition of IFS¹ wind and temperature data into GWs and PWs was carried out in Dörnbrack et al. (e.g. 2018). Whether PW modes propagate or not depends on

¹Integrated Forecast System

their propagation direction. Eastward propagating modes are all trapped, while westward propagating modes have a finite vertical wavelength if their eigenvalue is large enough. In case of a diurnal forcing through solar absorption, the most dominant modes are (1, 1), (1, 2), (1, 3), (1, -1), (1, -2), (1, -4), i.e. diurnal tides, where the first three are propagating and the last three are trapped modes. These modes are sketched in Figure 3.3. The same forcing also excites the semi-diurnal tides (SDT), i.e. (2, 2), (2, 3), (2, 4), (2, 5), (2, 6) which happen to be all propagating modes (not shown). If there is no forcing, the so called normal modes are present of which the most dominant ones are (1, -2), (1, -3), (1, -4), (2, -3), (3, -3) (see Fig. 3.3) which have periods of 5 days, 8 days, 12 days, 4 days and 2 days. Another important forcing mechanism is due to orography and results in quasi-stationary PWs with a nominal $\sigma = 0$. Due to transient atmospheric background conditions, though, this type of PW does have a σ that is non-zero. Hence the prefix “quasi”.

Not only tides but also PWs can be derived from Laplace’s tidal equation. However, they differ significantly in their generation. While tides are primarily driven by the absorption of solar radiation in the ozone layer or in the water vapor rich troposphere, PWs are excited by meridional gradients in potential vorticity (Brasseur and Solomon, 2006). The interested reader is referred to the works by e.g. Chapman and Lindzen (1970), Kasahara (1976), Volland (1988) and Forbes et al. (1995).

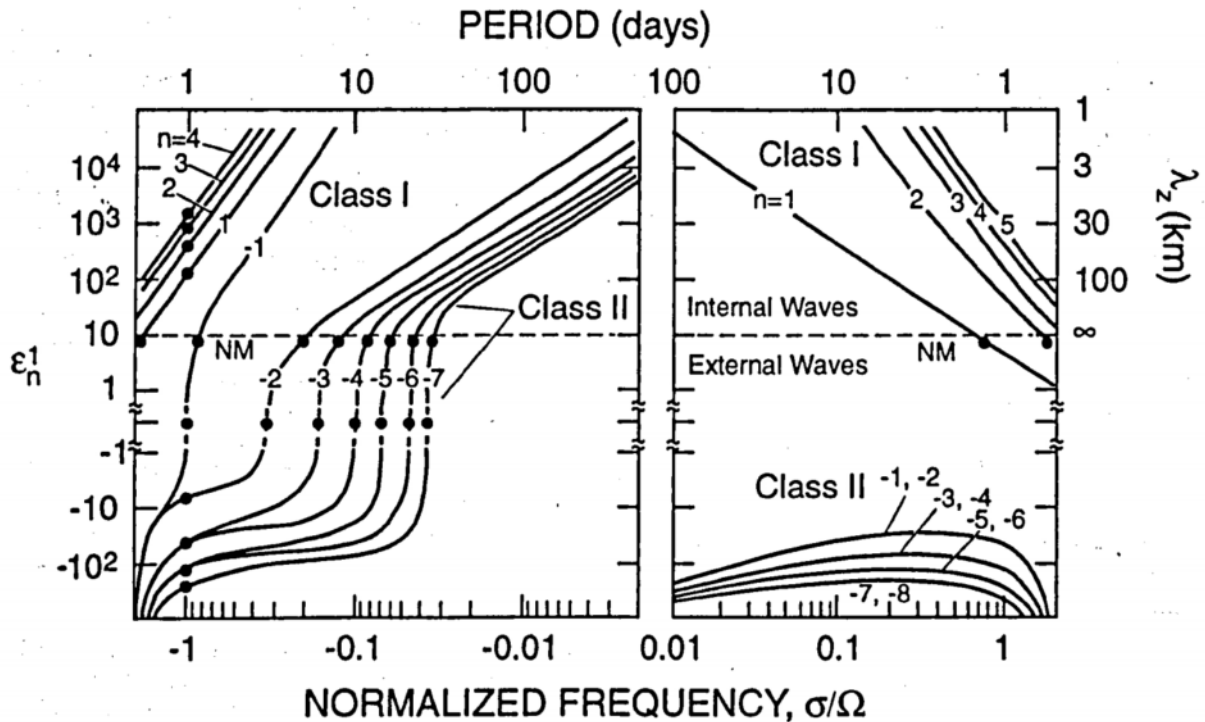


Figure 3.3: The figure is taken from Forbes et al. (1995) and shows the eigenvalues ϵ_n^1 of wave modes as function of normalized frequency with zonal wavenumber $s = 1$ for a selection of meridional indices n ranging from -8 to 5. The dots at $\epsilon_n^1 \approx 8.4$ mark normal modes (NM) and at $\sigma/\Omega = -1$ mark diurnal tides.

Butterworth Highpass Filter

In the introduction it was shown that a huge variety of dynamical modes manifest themselves in the thermal structure of the middle atmosphere. Ideally, one would like to separate GWs accurately from other phenomena. Multiple studies based on lidar data established a number of separation methods. One common possibility to reveal GW signatures is to remove the nightly mean temperature profile from measured profiles (Rauthe et al., 2008, Gardner and Taylor, 1998). The result of this method depends on the duration of the measurement and will eliminate any structures that are constant over time, e.g. MW signatures. On the other hand Yamashita et al. (2009) subtract a temporal running mean. The structures revealed by this method depend on the width of the running mean because oscillations larger than the window widths are suppressed. Whiteway and Carswell (1995), Duck et al. (2001) and Alexander et al. (2011) fit polynomial functions to temperature profiles in order to estimate the temperature background. In a comparative study, Ehard et al. (2015) suggested the application of a Butterworth high-pass filter in the vertical. This method is now frequently used (e.g. Baumgarten et al., 2017, Bramberger et al., 2017, Kaifler et al., 2017, Rapp et al., 2018a, Strelnikova et al., 2021). The transfer function of the Butterworth filter is defined as

$$H(\lambda_z) = \left(1 + \left(\frac{\lambda_z}{\lambda_{cut}} \right)^{2o} \right)^{-1/2}, \quad (3.9)$$

where o is the order of the filter, λ_{cut} the cutoff wavelength and λ_z the vertical wavelength. Butterworth et al. (1930) designed this filter such that its response is flat, meaning that the spectrum of the signal is altered as little as possible within the passband. Figure 3.4d shows the Butterworth transfer function with $o = 5$ and $\lambda_{cut} = 15$ km. In practice, the vertical temperature profile as it is displayed in Figure 3.4a is extended by a reversed version of itself in order to create an artificial periodicity. After that, the Butterworth transfer function is multiplied with the FFT-spectrum of the periodic temperature profile. To obtain the temperature perturbations, the inverse FFT of the modulated spectrum is computed. The high-pass and low-pass signals illustrate the separation of GW signals from the background. IFS data show an extended wave field over the southern tip of South America trailing downstream over the southern ocean at this particular date (not shown). From linear theory a vertical wavelength on the order of 25 km to 30 km is expected at the time of the measurement. This exemplary temperature profile was chosen to show that at a cutoff of 15 km a large part of the GW spectrum can be misinterpreted as background. In addition, if the cutoff is not sharp then amplitudes in the passband are strongly suppressed for $\lambda_z > \lambda_{cut}$. When lidar measurements are conducted sporadically and with low cadence, Ehard et al. (2015) recommend to use a Butterworth filter to separate GWs from the background. However, if the measurement cadence is sufficient to identify PWs and tides, these can be assigned to the temperature background. Ultimately, this background is subtracted from original temperature measurements and more realistic GW amplitudes can be retrieved.

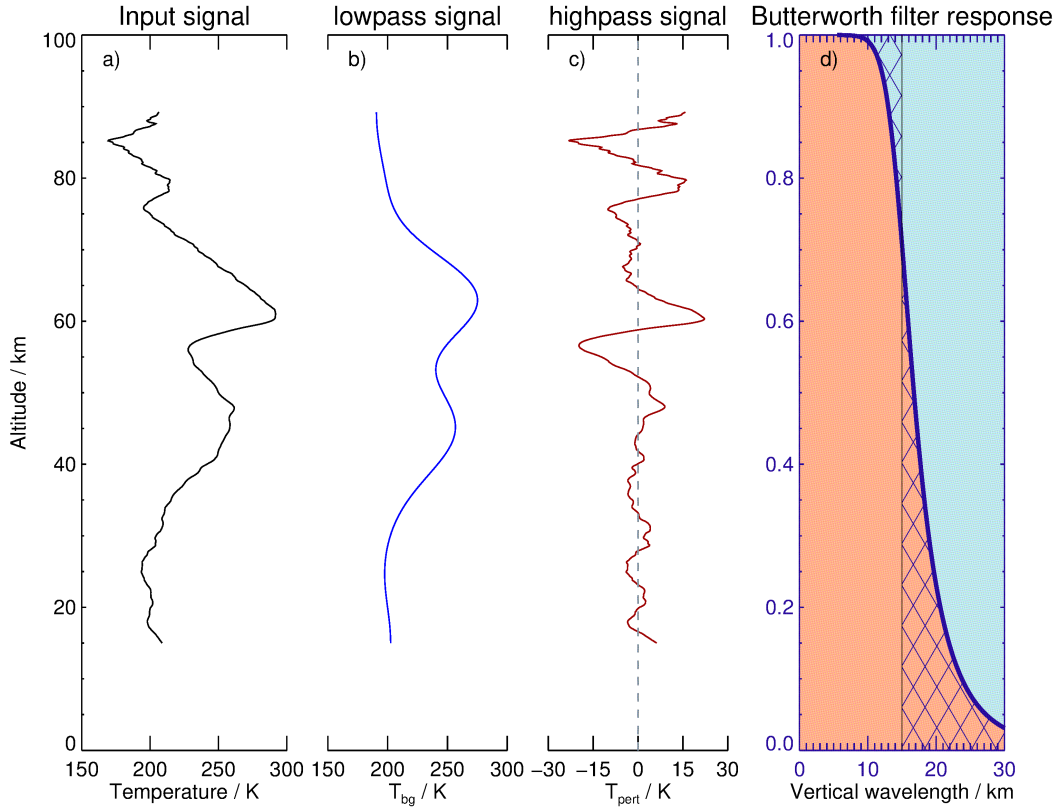


Figure 3.4: An input temperature profile (a) is juxtaposed to its low-pass profile (b) and high-pass profile (c). The filtering is done via a Butterworth filter with transfer function shown in (d) with a cutoff at 15 km. Colored areas mark parts of the spectrum that are represented in the high-pass (red) and low-pass (blue) signals. Hatched areas indicate high-frequency (low-frequency) parts of the spectrum that contribute to the low-pass (high-pass) signal.

Diurnal Tides Running 2D Fit

The extraction of diurnal tides (DT) from nighttime lidar measurements is a challenging task. The Nyquist-Shannon sampling theorem states that in order to resolve a desired frequency of a signal, the sampling frequency must be at least twice as large. In case of DT a sampling period of ≤ 12 h would be needed. CORAL's possible sampling periods are two fold: Within a nightly measurement, the sampling period is equal to the temporal resolution which can be as high as 5 min. On the other hand, in a period of clear sky conditions over multiple days, CORAL conducts measurements every night and thus at a sampling period of ~ 24 h. A composite analysis with a subsequent harmonic fit as it is done by [Kopp et al. \(2015\)](#) is not possible because individual measurements are too short in duration and not always obtained at the same local solar time (LST). Yet, a harmonic fit can be used to extract the amplitude and phase of DT from an irregularly sampled timeseries. [Figure 3.5](#) illustrates the recovery of DT from simulated lidar temperature data. The artificial temperature data comprise white noise with a standard deviation of 0.1 K and DT with an amplitude of 1 K ([Fig. 3.5a, b](#)). The timeseries are cropped

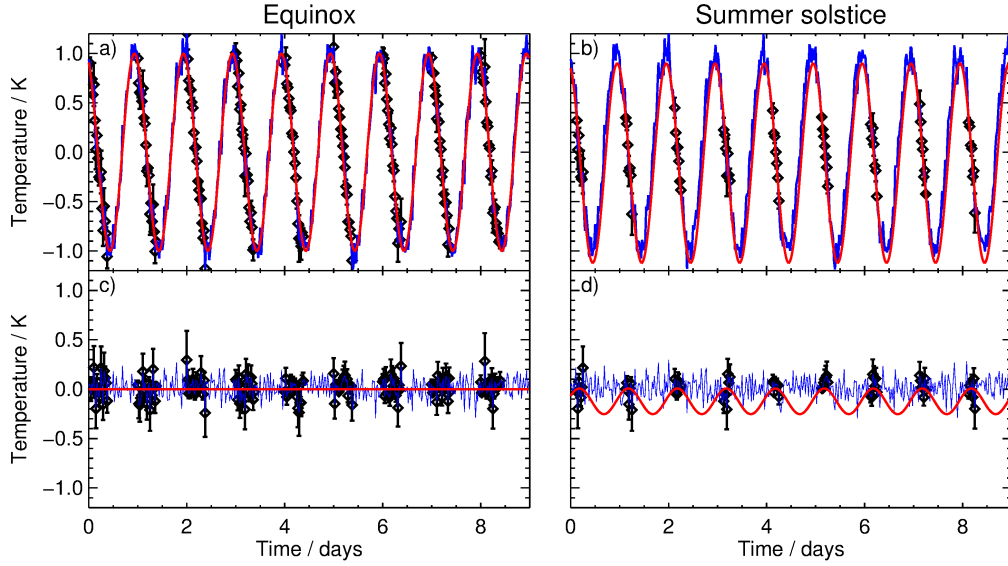


Figure 3.5: A cosine with an amplitude of 1 K and a period of 1 day superimposed with white noise ($\sigma = 0.1$ K) simulates the DT over the course of 9 days (blue line in a,b). Only white noise is shown for reference (blue line in c,d). Lidar sampling is imitated for equinox (a,c) and summer solstice (b,d) conditions (black diamonds and error bars). The red lines show harmonic fits of diurnal period applied to the cropped data.

in accordance to equinox (Fig. 3.5a, c) and summer solstice (Fig. 3.5b, d) conditions to simulate CORAL's irregular i.e. nighttime sampling. After that, a least-square harmonic fit is applied to the irregularly sampled data. The fit function is given as

$$T_{fit}(t) = D + T_{DT} \quad (3.10)$$

$$= D + B_{DT} \cos(\Omega(t + \tau_{DT})) \quad (3.11)$$

where D is a constant offset, B_{DT} is the amplitude, Ω is the angular frequency of DT, and τ_{DT} is the phase of DT. Even during summer solstice conditions when measurements are shortest, the harmonic fit over 9 days captures the original timeseries quite well. A problem appears though when no DT are present in the data. This case is illustrated in Figure 3.5c, d when the amplitude of the simulated tide was set to zero. In this case the timeseries only consists of white noise. During equinox conditions the harmonic fit applied to white noise delivers reasonably small values for the amplitude of DT. However, during summer solstice conditions the data coverage is not large enough, and the fit retrieves amplitudes and phases indicating DT which are not present in the original timeseries. This example demonstrates that generally information about DT can be extracted from irregularly sampled data although the sampling period, according to the Nyquist-Shannon sampling theorem, is not sufficient. However, it also becomes clear that the fit delivers erroneous results in seasons of short nights and at altitudes where no DT signal is present.

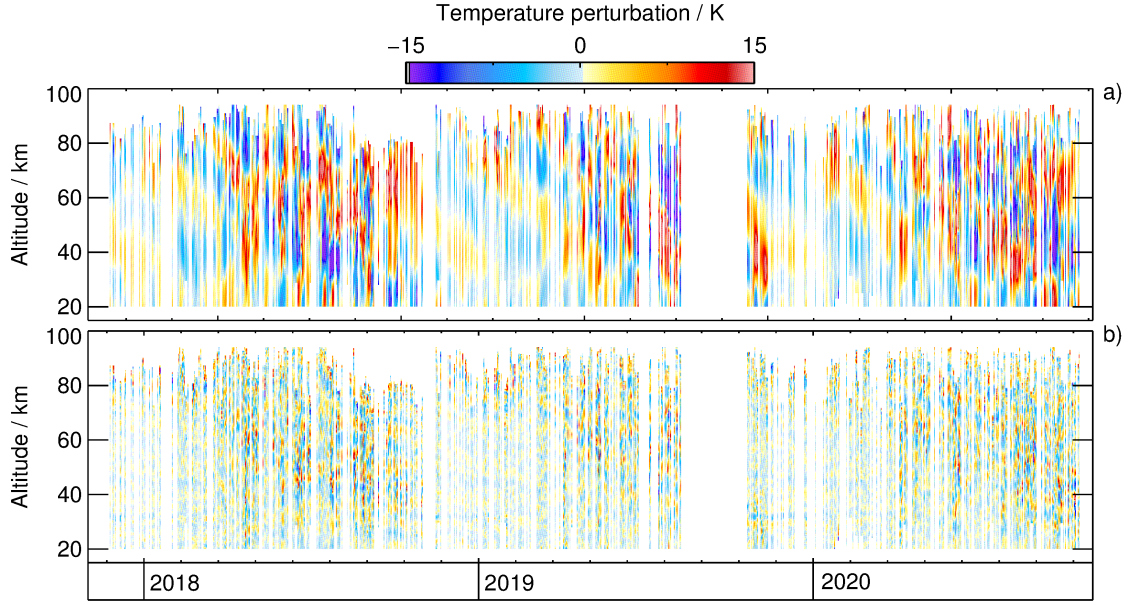


Figure 3.6: Illustrated are (t, z) -cross sections of temperature perturbations with vertical wavelengths >15 km T'' (a) and temperature perturbations with vertical wavelengths <15 km T' (b). This figure is adapted from [Reichert et al. \(2021\)](#).

[Figure 3.5](#) illustrates a rather perfect example with no background signal superimposed and using nighttime observations to full capacity. In reality, especially in winter, there are longer nights, but PW activity causes a variable thermal background and GWs generate more short term “noise”. To include a variable background, the harmonic fit function is extended with two linear elements. The fit function is defined as

$$T_{fit}(t, z) = T_{PW} + T_{DT} \quad (3.12)$$

$$= D + Ft + Gz + B_{DT} \cos(\Omega(t + \tau_{DT})) \quad (3.13)$$

where F and G are linear temperature changes in time and height, respectively. Before the fit is applied to the sub-seasonal temperature perturbations, another filtering step is needed. From theory and previous studies it is known that DT are either trapped or have a very large vertical wavelength. Therefore, a 5th order Butterworth high-pass filter is applied to vertical temperature profiles to get rid of GW contamination. A critical parameter is the cutoff wavelength λ_{cut} . If chosen too small, a larger part of the GW spectrum will be assigned to the background. If chosen too large, background features like tides and PWs are taken for GWs. For the following analysis the cutoff wavelength is defined as $\lambda_{cut} = 15$ km, a value used in multiple studies ([Baumgarten et al., 2017](#), [Bramberger et al., 2017](#), [Kaifler et al., 2017](#), [Rapp et al., 2018a](#)).

The application of the Butterworth filter yields

$$\tilde{T} = T'' + T' \quad (3.14)$$

where T'' indicates perturbations with vertical wavelengths >15 km and T' perturbations with vertical wavelength <15 km. [Figure 3.6](#) illustrates T'' and T' . Please note that under the right atmospheric background conditions GWs can have vertical wavelengths that

exceed 15 km. These GWs may contaminate T'' and the results of the fit. In order to keep a clear overview of the temperature decomposition, [table 3.1](#) summarizes all temperature contributions.

To capture the temporal and spatial variability of tides, the fit function is applied to CORAL's data in a running window. A similar method is used by [Stober et al. \(2017\)](#) and [Conte et al. \(2017\)](#) in order to extract tidal information from meteor radar data. As the fit function is two dimensional and applied in a running manner, the method is called DT running 2D fit (DT-R2D fit). By shifting the fit window in steps of 30 min in time and 2 km in altitude, not only $T_{DT}(t, z)$ but also $T_{PW}(t, z)$

T	$=$	\bar{T}	$+$	T_{SO}	$+$	\tilde{T}
T_{SO}	$=$	T_{AO}	$+$	T_{SAO}		
\tilde{T}	$=$	T''	$+$	T'		
T''	$=$	T_{PW}	$+$	T_{DT}	$+$	T_{Rest}
T_{GW}	$=$	T'	$+$	T_{Rest}		

Table 3.1: Temperature decomposition.

are retrieved. [Figure 3.7](#) shows four timeseries of T'' at altitudes of 30 km, 50 km, 70 km and 90 km and the result of the DT-R2D fit. The result of the DT-R2D fit for all altitudes is illustrated in [Figure 3.8](#) for a time period with good data coverage in March 2019. In the period of time that is chosen to demonstrate the result of the DT-R2D fit in [Figure 3.7](#), CORAL obtained measurements every single night. In addition, PW and also GW activity is very low during that time of the year. Therefore, the DT-R2D fit could retrieve reliable information about DT. Amplitudes of DT peak near 50 km and 80 km ([Figure 3.8](#)). In both regions the phase lines appear very steep, while above 80 km, phase lines show a significant phase progression. Please note that temperature uncertainties above 80 km are generally large with respect to the tidal amplitudes such that reliable statements about tidal signatures cannot be made.

To bridge most of the measurement gaps within CORAL data, the fit window is set to be 9 days long. However, to be sensitive to PWs with periods shorter than 9 days in the case of a high measurement cadence, the measurements are weighted with a 2D Gaussian function during the fit. The Gaussian has a standard deviation of 3 days in the time domain and 2 km in the vertical. Although the fit window spans 9 days, the running manner in combination with the Gaussian weighting also makes the DT-R2D fit sensitive to PWs with periods of 3 to 9 days.

[Figure 3.9](#) and [Figure 3.10](#) illustrate the same quantities as [Figure 3.7](#) and [Figure 3.8](#) but for another period of nine days in July 2020. [Figure 3.9](#) shows that within 9 days CORAL obtained seven measurements, i.e. the data coverage is sufficiently good. Yet, it becomes clear that temperature deviations on shorter temporal scales are probably leftovers from GWs with large vertical wavelengths, tides, or other unconsidered phenomena. In addition, [Figure 3.10](#) reveals a PW with an approximate vertical wavelength of 50 km. To keep the DT-R2D fit on track such that retrieved parameters do not exhibit unphysical sudden jumps in time or altitude, a number of constraints are implemented. [Table 3.2](#) lists all constraints that are used.

Fit-parameter	global limits	dynamic limits in time	dynamic limits in altitude
D	$\pm 50 \text{ K}$	$\pm 5.0 \text{ K d}^{-1}$	$\pm 4.0 \text{ K km}^{-1}$
F	$\pm 5.0 \text{ K d}^{-1}$	$\pm 2.2 \text{ K d}^{-2}$	$\pm 0.7 \text{ K d}^{-1} \text{ km}^{-1}$
G	$\pm 4.0 \text{ K km}^{-1}$	$\pm 0.7 \text{ K d}^{-1} \text{ km}^{-1}$	$\pm 0.8 \text{ K km}^{-2}$
B_{DT}	None	$\pm 2.2 \text{ K d}^{-2}$	$\pm 0.7 \text{ K d}^{-1} \text{ km}^{-1}$
τ_{DT}	None	$\pm 0.8 \text{ h d}^{-1}$	$\pm 1.6 \text{ h km}^{-1}$

Table 3.2: Global and dynamic constraints for the fit parameters of the DT-R2D fit.

The constraints are divided into global and dynamic. Global constraints are always valid, i.e. the fit parameters are not allowed to take on values that are below the lower constraint or above the upper constraint. Dynamic constraints make sure that retrieved fit parameters do not deviate drastically from parameters that are retrieved in prior time or altitude steps. Hence, dynamic constraints can be regarded as a maximum and minimum allowed rate of change of the parameters with time or altitude. Most constraints were found by trial and error. However, some constraints do have a reasonable physical meaning. The phase of DT is confined in time such that, at maximum, it can only shift by one oscillation within one month. As the data were previously low-pass filtered with a cutoff wavelength of 15 km, the phase is also restricted in the vertical such that it changes no more than 24 h within 15 km.

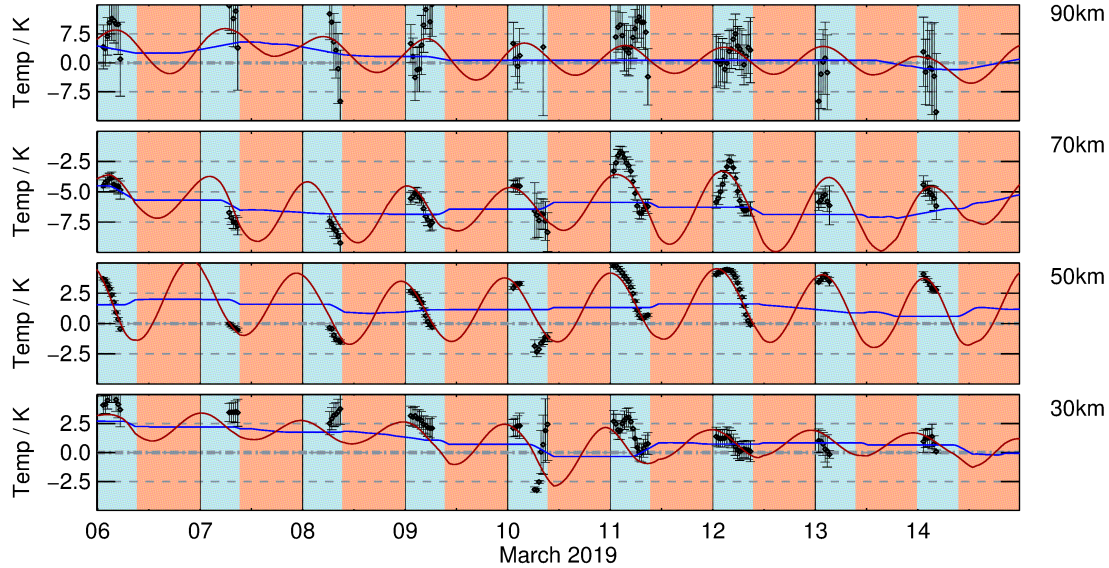


Figure 3.7: T'' is depicted at equinox conditions at altitudes of 30 km, 50 km, 70 km and 90 km (black diamonds and error bars). The temperature background T_{PW} is illustrated by blue lines and the DT signal T_{DT} by red lines. Blue and red background colors mark night and day.

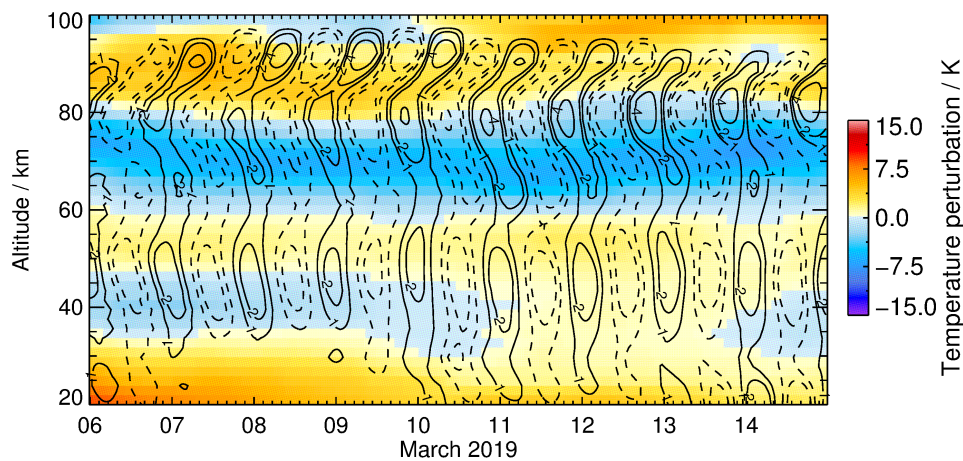


Figure 3.8: Illustrated are temperature perturbation reconstructions based on the DT-R2D fit results. The blue-red colorscale refers to T_{PW} while contourlines illustrate perturbations due to DT. Contourlines mark 1 K, 2 K and 4 K (solid) as well as -1 K, -2 K and -4 K contours (dashed).

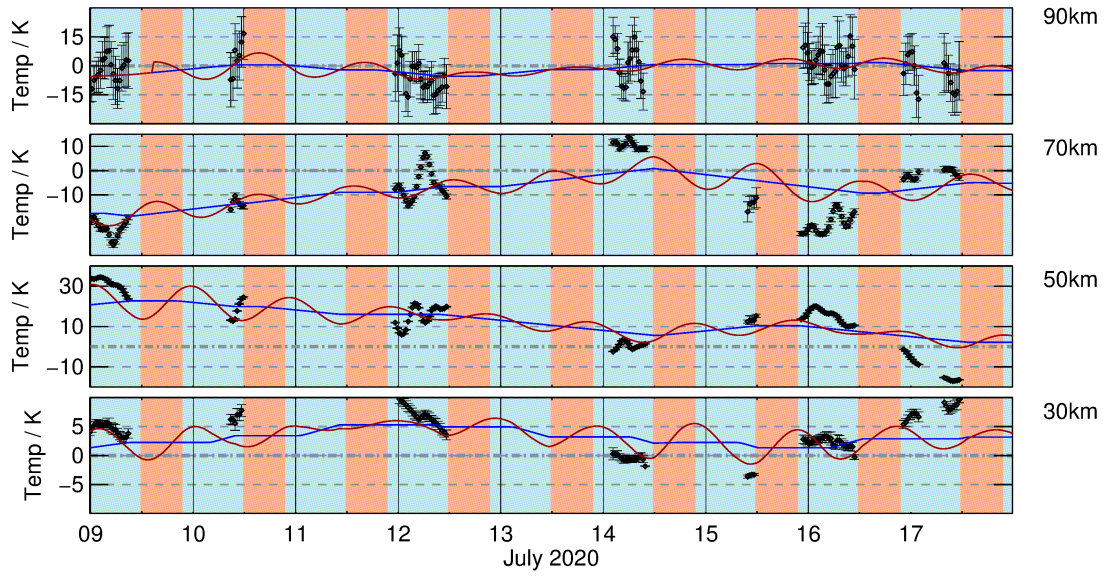


Figure 3.9: Same as [Figure 3.7](#) but for a period of nine days during July 2020.

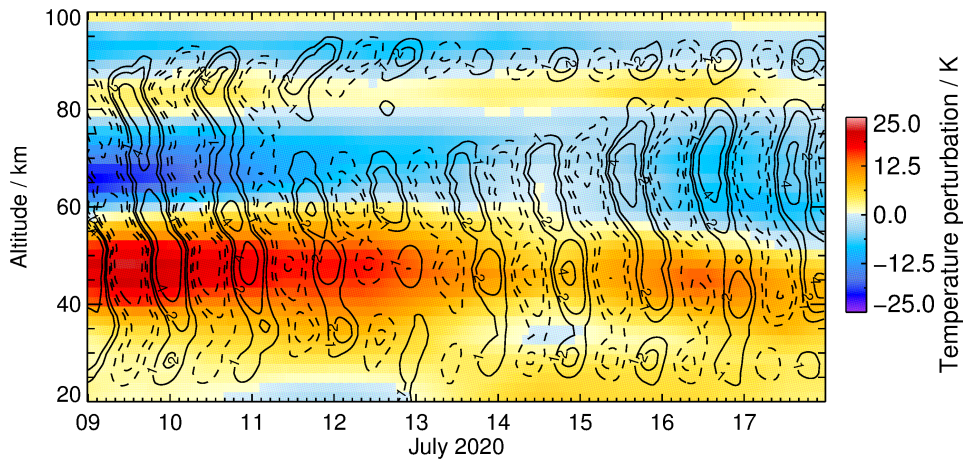


Figure 3.10: Same as [Figure 3.8](#) but for a period of nine days during July 2020.

3.2 Results

3.2.1 Amplitudes and Phases of Diurnal Tides

Figure 3.11 shows monthly mean DT amplitudes as retrieved from the DT-R2D fit applied to CORAL T'' data and to ERA5 reanalysis data. DT amplitudes as retrieved from ERA5 data show about the same vertical distribution throughout the year. In the lower stratosphere, they are rather weak but increase to a broad maximum of about 2 K near 50 km. In the mesosphere, ERA5 amplitudes decrease to a minimum near 70 km. Enhanced standard deviations between May and August are particularly striking. In December and January no DT amplitudes are retrieved from CORAL data due to short measurement durations. Please note that also in November and February statistics are not robust. However, mean CORAL amplitudes during that time of the year are in good agreement with ERA5 amplitudes. The same holds true in the winter season, although CORAL amplitudes are always larger. Enhanced deviations are found in the mesosphere where CORAL amplitudes are significantly larger than ERA5 amplitudes and mostly increase up to 90 km to 4 – 6 K.

Monthly mean phases of the DT as retrieved from CORAL and ERA5 data are presented in Figure 3.12. Again, profiles of DT phases retrieved from CORAL and ERA5 data agree nicely within their standard deviations. In summer ERA5 phases are constant at 18 h LST between 20 km and 60 km and exhibit very small standard deviations. In winter the phase profile appears more variable with phaseshifts of $\sim \pm 6$ h, and standard deviations also increase. CORAL phases are also centered at 18 h LST below 60 km but show larger variability than ERA5 phases. Above 60 km CORAL phases deviate even stronger from 18 h LST. In March, not only the amplitudes from CORAL and ERA5 of DT agree well, but also the phases. In this month DT can be explored best in CORAL data as nights, i.e. measurements, get longer while at the same time contamination from PWs and GWs is still very low.

3.2.2 Planetary Wave Disturbances

Now T_{PW} is investigated as retrieved by the DT-R2D fit described in Section 3.1.2. Figure 3.13 illustrates T_{PW} of which a running mean over 45 days is subtracted to emphasize PWs as it is done by e.g. Hauchecorne and Chanin (1983). In addition, temperature perturbations from ERA5 are overplotted as contour lines. From ERA5 data a 45 day running mean is subtracted and afterwards, for better comparison, a 9 day running mean is applied in order to mimic the averaging effect of the DT-R2D fit. Enhanced PW activity is evident in austral winter at all altitudes. PW activity in winter is expected from theory as vertical propagation is only permitted if zonal winds are westerly (Brasseur and Solomon, 2006). For the most part, structures in both temperature perturbation fields are in good agreement. Only minor deviations are present, for example in the winter of 2018 above 65 km where PW amplitudes decrease in the ERA5 data. The dominant period is in the order of ~ 30 days, suggesting the presence of a quasi-stationary wave.

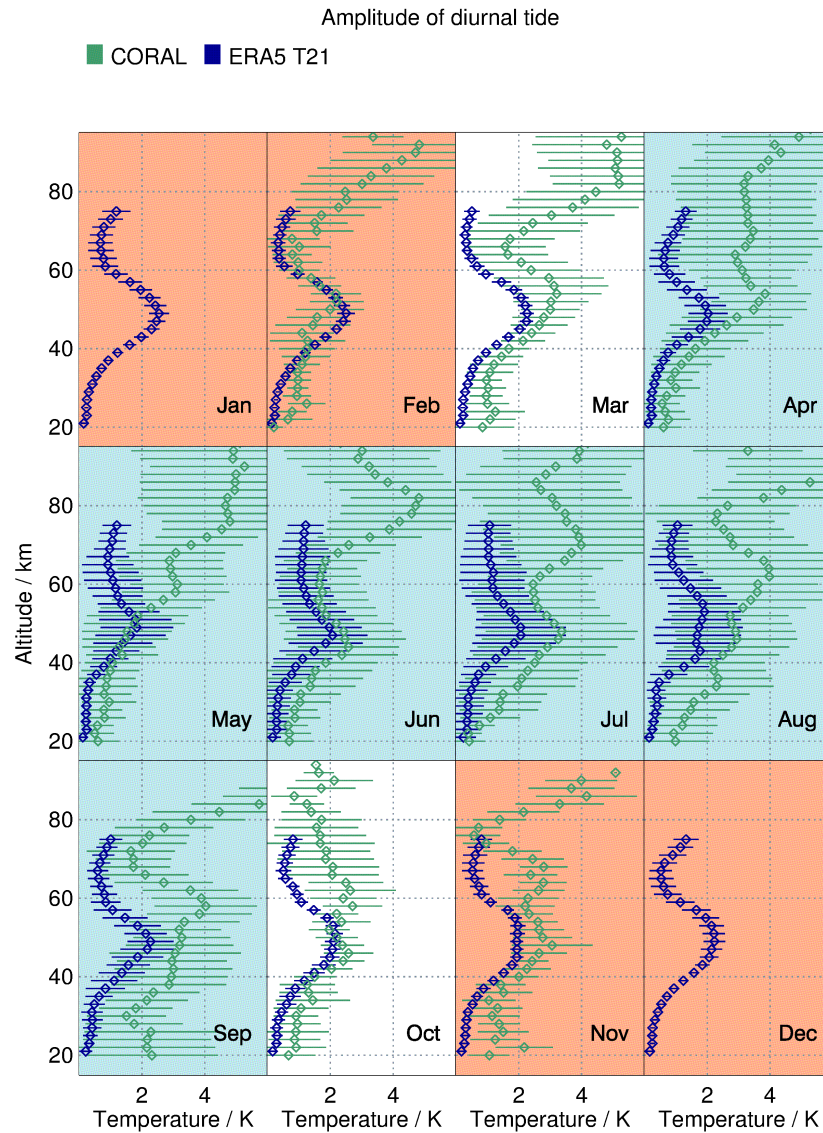


Figure 3.11: Monthly mean profiles depict amplitudes (diamonds) of the DT as retrieved by the DT-R2D fit applied to CORAL (green) and ERA5 (blue) data. Monthly standard deviations are indicated by horizontal lines. Due to poor data coverage no amplitudes are retrieved from CORAL data in December and January.

3.2.3 Amplitudes and Phases of Seasonal Oscillations

Results of amplitude and phase plotted as times of maximum amplitude of the AO and the SAO are shown in [Figure 3.14](#). Only values are included that are retrieved from fits based on a minimum number of 100 days with measurements. [Figure 3.14](#) reveals a stratospheric AO with its maximum in austral summer and a mesospheric AO with its maximum in austral winter. Both oscillations are separated by a pronounced minimum at 62 km. The peak mesospheric AO amplitude of 22.5 K is observed at 88 km while the peak stratospheric AO amplitude of 18 K is found at 32 km. The phase lines shown in

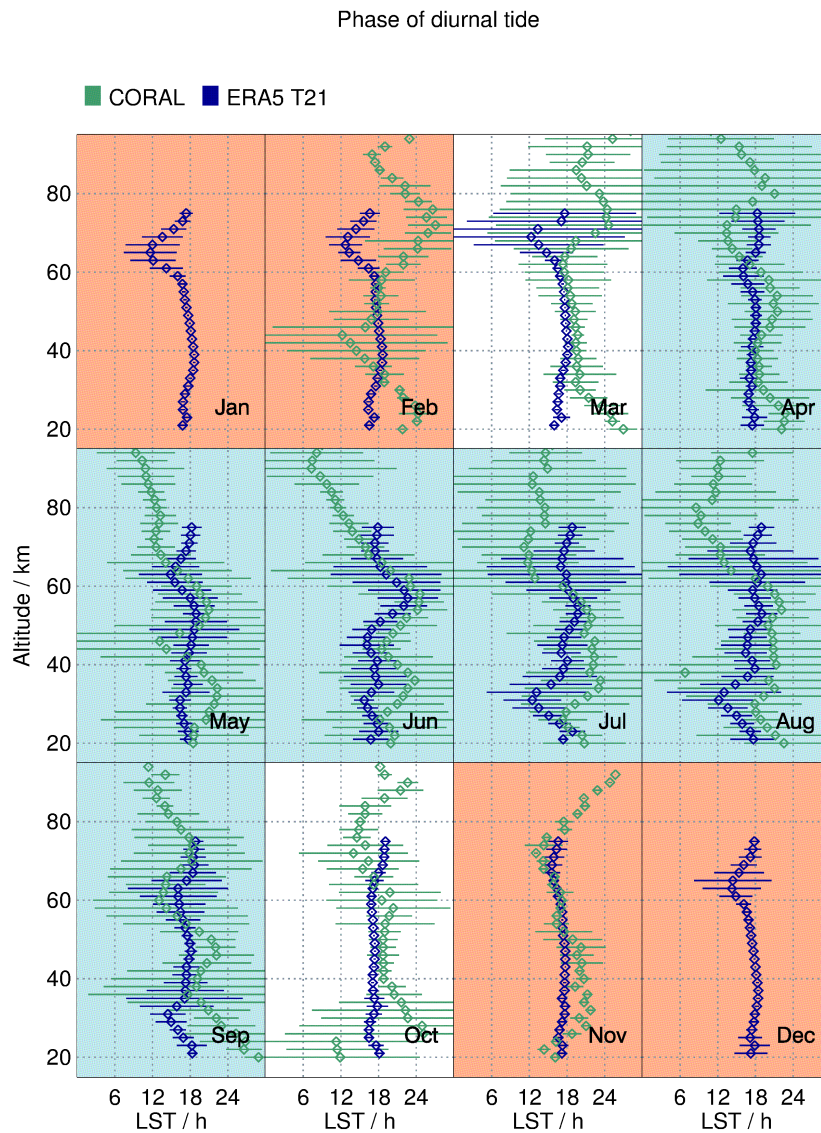


Figure 3.12: This figure shows the same as [Figure 3.11](#) but for the phases of the DT.

[Figure 3.14c](#) indicate the location of the maximum of each oscillation. The stratospheric AO exhibits a downward phase progression of $-42 \text{ km month}^{-1}$ while the mesospheric AO shows a positive phase speed of 40 km month^{-1} from 65 to 78 km and a negative phase speed of $-21 \text{ km month}^{-1}$ from 78 to 95 km.

The SAO exhibits three maxima in amplitude: At 41 km (6.5 K), referred to as stratospheric SAO (SSAO); at 65 km (8 K), referred to as lower mesospheric SAO (LMSAO), and at 88 km (10.5 K), referred to as mesospheric SAO (MSAO). The SSAO and the MSAO exhibit a phase shift of about 4 to 5 months. There is an almost infinite vertical phase speed in the case of the MSAO, a downward progression of -9 km month^{-1} for the LMSAO, and a downward progression of $-12 \text{ km month}^{-1}$ for the SSAO. In contrast to the amplitudes, the phase changes continuously from the SSAO to the LMSAO. There is

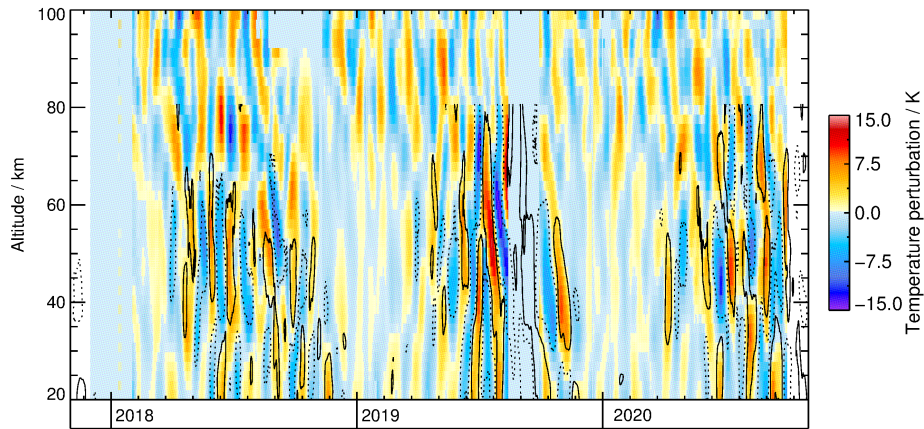
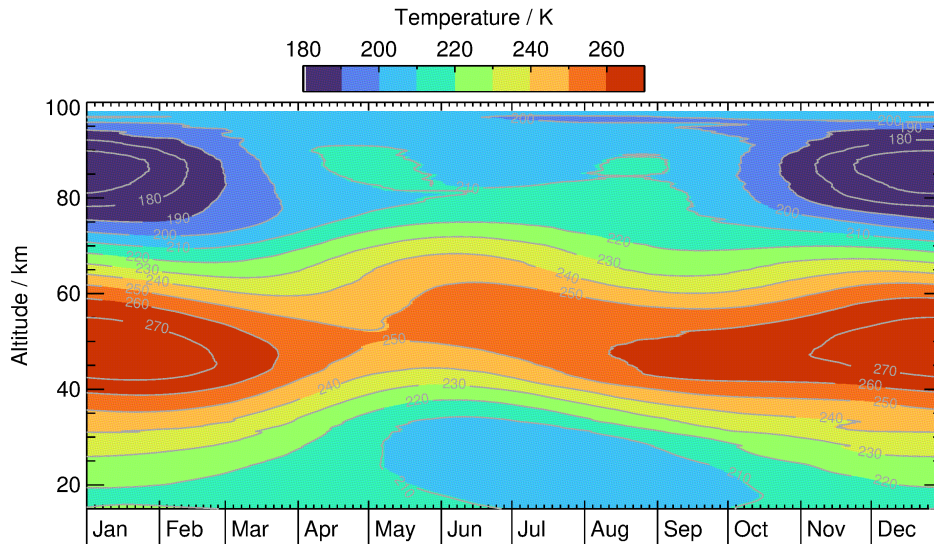
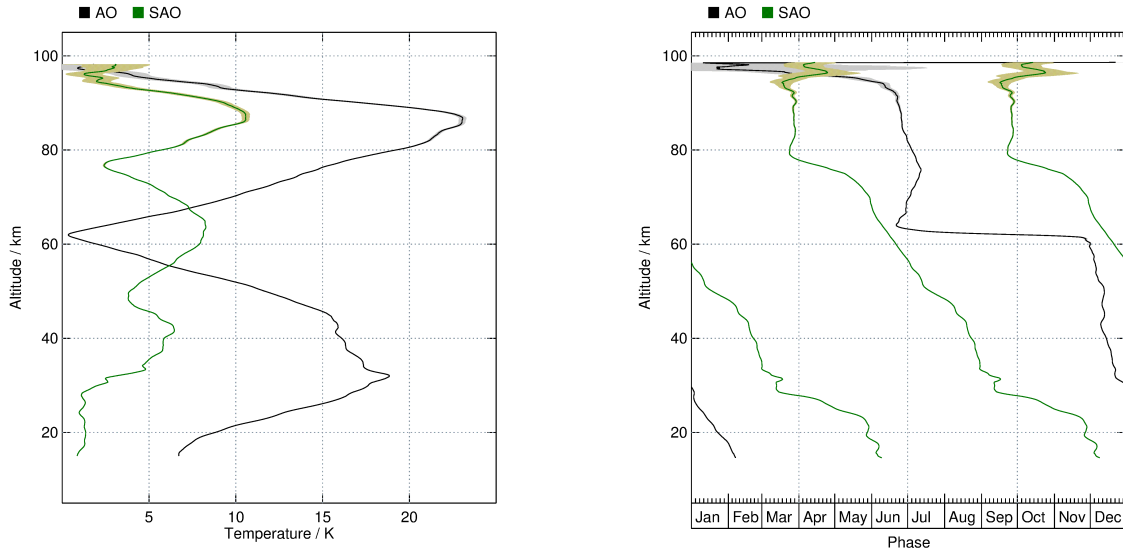


Figure 3.13: Illustrated are temperature perturbations due to PWs, T_{PW} , as retrieved by the DT-R2D fit with a running mean over 45 days subtracted. Contour lines show temperature perturbations from ERA5 data of which also a 45 days running mean is subtracted. Contour levels are 3 K (solid) and -3 K (dotted).

a more or less constant phase shift of 3 months between both the SSAO and the stratospheric AO as well as the MSAO and the mesospheric AO. The superposition of the two oscillations in the stratosphere causes the addition of the amplitudes in winter, resulting in a relatively sharp pronounced temperature minimum, while in summer the amplitude of the SAO is subtracted from that of the AO, resulting in a relatively broad and weak temperature maximum. The situation is similar in the mesosphere. There a strongly pronounced temperature minimum is observed in summer and a weakly pronounced temperature maximum is observed in winter (Fig. 3.14a).



(a) Illustrated is the (t, z) -cross section of temperature comprising seasonal oscillations T_{SO} . This figure is adapted from Reichert et al. (2021).



(b) Profiles of the amplitude of the AO (black) and SAO (green) are shown. Background shading marks the 1σ standard deviation.

(c) Profiles of the phase, i.e. time of the maximum of the AO (black) and SAO (green) are shown. Background shading marks the 1σ standard deviation.

Figure 3.14: Depicted are the results of the harmonic fit applied to a composite of CORAL's nightly mean temperature profiles.

3.3 Discussion

3.3.1 Diurnal Tides

At the outset, it should be emphasized that a ground-based observer cannot make a statement about the wave number of the DT, nor can he make a statement about the direction in which the DT is migrating. A reasonable agreement was found between amplitudes and phases of DTs as retrieved from CORAL and ERA5 data up to about 60 km. Major differences above 60 km are caused by the sponge layer in the ERA5 which dampens tidal amplitudes in the model and could also arise due to a leakage of variance from SDTs and large-scale ($\lambda_z > 15$ km) GWs in CORAL data. On the other hand, amplitudes of diurnal migrating tides in reanalysis data are underestimated by 20% to 50% compared to SABER data (Sakazaki et al., 2018, Gerber et al., 2021). In addition, the standard deviation of DT amplitudes as retrieved from CORAL are significantly larger than retrieved from ERA5. This may be due to the fact that CORAL data is filtered vertically with a Butterworth filter and ERA5 data is spectrally truncated at wavenumber 21.

Kopp et al. (2015) derived amplitudes and phases of DTs utilizing data acquired by a daylight-capable lidar at a site in northern Germany (54° N, 12° E). In the summer months they found a maximum monthly mean DT amplitude near 50 km altitude on the order of 2 K which is comparable to derived DT amplitudes from ERA5 at Río Grande. In March the maximum amplitude increased to 4 K near 45 km. Larger amplitudes of up to 10 K were found in the MLT region in April and August. DT amplitudes as derived from CORAL are on the same order of magnitude but have large standard deviations. This is underscored by findings from Baumgarten and Stober (2019), where they confirm the monthly mean DT amplitudes in the stratosphere as reported by Kopp et al. (2015) but highlight the variability of DTs on time scales of a few days. Pancheva and Mukhtarov (2011) investigated the diurnal westward migrating tide in SABER data and have shown that it reaches a first maximum at 50 km with amplitudes in the range of 1.5 – 3.5 K during the course of the year at 50° S. Findings in Sec. 3.2.1 agree with results presented in Pancheva and Mukhtarov (2011). Larger amplitudes of up to 4.5 K with greater variability throughout the year are also found in SABER data above 80 km. In this altitude range similar DT amplitudes are found but they may be artificially enhanced due to spectral leakage and contamination by SDTs. The phase of DTs in the stratosphere is in the range of 15 h – 18 h LST. The same was found in studies by Kopp et al. (2015) and Pancheva and Mukhtarov (2011).

3.3.2 Semi-diurnal Tides

SDTs become dominant in the mesosphere, where they can exhibit temperature amplitudes in the range of 3 K to 8 K (Pancheva and Mukhtarov, 2011, Kopp et al., 2015). CORAL data often show significant temperature perturbations with a period of 12 h if measurements are long enough (see 11/12 March 2019 at 70 km in Figure 3.7). An attempt was made to extend the DT-R2D fit to include a harmonic fit with a 12 h period. However, the fit did not provide reliable results. It is likely that some of the SDT variance is reflected in the amplitudes of DTs. This may be to some degree responsible for the

relatively large DT amplitudes in the mesosphere and the increased DT variability at these altitudes.

3.3.3 Stationary Wave-1

The most reasonable explanation for the occurrence of temperature perturbations with a period of ~ 30 days (Fig. 3.13) is quasi-stationary PWs with wavenumber 1. According to Charney and Drazin (1961) there is a window of zonal mean winds that permits the vertical propagation of Rossby waves into the middle atmosphere. The condition is $0 < \bar{u} - c < u_c$ where \bar{u} denotes the zonal mean zonal wind and c the phase velocity of the PW. The upper limit called ‘‘Rossby critical velocity’’ is given by

$$u_c = \frac{\bar{q}_\phi}{k^2 + l^2 + \left(\frac{f}{2NH}\right)^2} \quad (3.15)$$

where \bar{q}_ϕ is the meridional gradient of potential vorticity. A typical value for u_c for a wave-1 is 57 ms^{-1} (Plumb, 2010). The zonal mean zonal wind at 60° S at 10 hPa averaged between 1979 and 2020 is $> 57 \text{ ms}^{-1}$ between May and September.² How then is it possible that strong PW activity is observed in austral winter if, according to the Rossby critical velocity, waves are prohibited from propagating vertically? The Charney-Drazin Criterion is only valid in the absence of wind shear, i.e. $\frac{\partial u}{\partial y} = \frac{\partial u}{\partial z} = 0$. This is generally not the case. To investigate whether a wave-1 is able to propagate vertically, the refractive index for PWs can be used. It is given by e.g. Li et al. (2007) as

$$n_k^2(y, z) = \frac{\bar{q}_\phi}{\bar{u}} - \left(\frac{k}{a \cos(\phi)}\right)^2 - \left(\frac{f}{2NH}\right)^2. \quad (3.16)$$

If the condition $n_k^2 > 0$ is met, the Rossby wave can propagate vertically. Figure 3.15 shows the (t, z) -cross section of the refractive index for a wave-1 at the latitude of R rio Grande. The areas with positive refractive index suggests that PWs can propagate up to 40 km at all times of the year. Only between November 2019 and March 2020, between 20 km and 35 km altitudes, negative refractive indices suggest confinement of PWs to altitudes below ~ 20 km. Also, generally during the summer months from November to February, no vertical propagation of PWs is possible above 40 km.

Randel (1988) investigated the seasonal evolution of PWs in the southern hemisphere stratosphere. They also found that a stationary wave-1 is able to propagate vertically up to 50 km in austral winter. Enhanced amplitudes of the SAO in CORAL data might be affected by two wave-1 variance maxima, one at the beginning and one at the end of the southern hemispheric winter season (Randel, 1988, Hirota et al., 1983).

3.3.4 Seasonal Oscillations

As evident from Figure 3.14b, the mesospheric AO is larger than the stratospheric AO. This is consistent with previous studies (Fleming et al., 1990, Remsberg et al., 2002,

²1979 – 2020 average zonal mean zonal wind taken from https://acd-ext.gsfc.nasa.gov/Data_services/met/ann_data.html

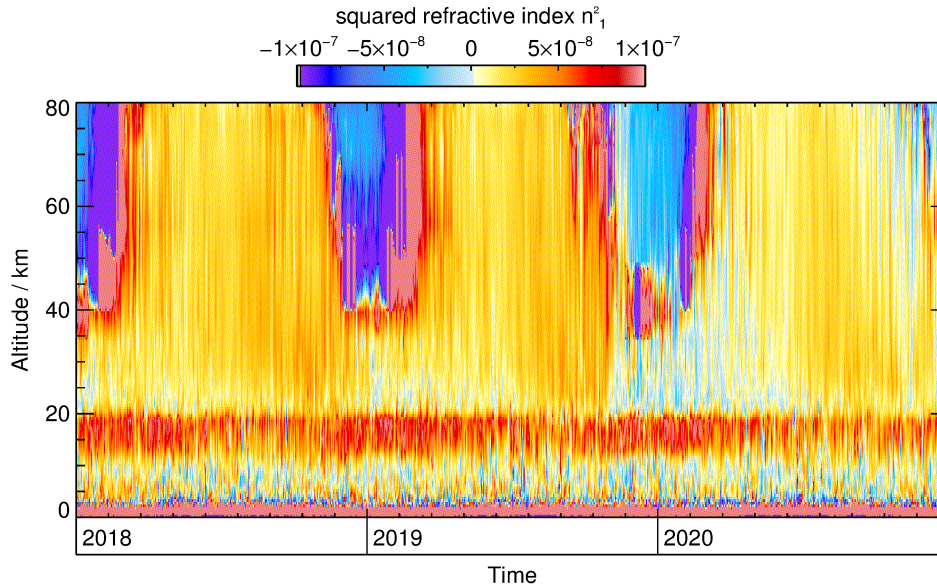


Figure 3.15: Illustrated is a (t, z) -cross section of the squared refractive index n_1^2 for wavenumber 1 based on ERA5 data at the location of Río Grande. Positive values (red) indicate that vertical propagation of PWs is possible, while negative values (blue) suggest that vertical propagation cannot occur.

	latitude	stratospheric AO	mesospheric AO	SSAO	LMSAO	MSAO
Fleming et al. (1990)	54° S	20 – 30 K	25 – 35 K	4 – 6 K	4 – 6 K	6 – 8 K
this study	54° S	18.0 K	22.5 K	6.5 K	8.0 K	10.5 K
Zhang et al. (2017)	50° S	–	–	>3.5 K	>4.5 K	>5.0 K
Zhang et al. (2017)	50° N	–	–	>1.5 K	3.0 – 3.5 K	>3.5 K
Gerding et al. (2008)	54° N	13.1 K	27.1 K	5.0 K	3.0 K	9.0 K
Fleming et al. (1990)	54° N	10 – 20 K	25 – 35 K	4 – 6 K	1 – 2 K	5 – 7 K

Table 3.3: AO and SAO amplitudes are listed from CIRA-86 (Fleming et al., 1990), SABER (Zhang et al., 2017) and two lidar studies (this study and Gerding et al., 2008).

Zhang et al., 2017). The same applies for the observed phaseshift of ~ 6 months. Amplitudes of seasonal oscillations derived in this work and from three other studies are listed in Table 3.3. Gerding et al. (2008) investigated seasonal oscillations utilizing a lidar system at a site in northern Germany which is conjugate in latitude to southern Argentina. In addition, findings are juxtaposed to CIRA-86 (Fleming et al., 1990) evaluated at 54° S and 54° N as well as SABER data (Zhang et al., 2017) evaluated at 50° S and 50° N. Please note that derived seasonal oscillations from CIRA-86 and from SABER data are based on zonal averages. Hence, differences between results from lidar studies and CIRA-86 or SABER are possibly an indication of local anomalies. For example, a local anomaly is the strong localized amplitude of the SSAO in the southern hemisphere eastern hemisphere (Gao et al., 1987). Another explanation for differences between the lidar studies and

CIRA-86 and SABER is tidal aliasing which is known to occur in analyses based on only nighttime measurements. In the worst case, the retrieved amplitude of seasonal oscillations is amplified by a factor equal to the peak-to-peak amplitude of present tides. However, the persistent phase relation between tides and measurements in darkness as well as measurements that are distributed over a couple of hours usually result in smaller aliased amplitudes. A maximum aliased MSAO amplitude of 2 K to 3 K was found when modelling DTs of intraannual variation of 1 K to 7 K at 87 km altitude at low latitudes (Zhao et al., 2007). Such an intraannual variation is comparable to results in Sec. 3.2.1, and thus it is possible that aliased amplitudes contribute 2 K to 3 K to the MSAO derived from CORAL data as well. This can explain the differences between the results in this work and the amplitudes from CIRA-86 and SABER to some degree. Similarly, the MSAO amplitude is also larger in the lidar study by Gerding et al. (2008) in comparison to CIRA-86 and SABER.

There is a significant difference in LMSAO amplitudes between the northern and southern hemisphere which is known to be caused by wave-1 variance maxima at the beginning and end of the austral winter season (Gao et al., 1987, Randel, 1988). LMSAO amplitudes are found that are at least 2 K larger in comparison to CIRA-86 and SABER results which may also be affected by tidal aliasing as derived amplitudes of DTs are on the order of 2 K to 4 K at these altitudes. It is also worth mentioning that Gao et al. (1987) report on a non-negligible year-to-year variability of the LMSAO amplitude.

The amplitudes derived for the SSAO above Río Grande are 0.5 K to 2.5 K larger than the values found in CIRA-86 and also 1.5 K larger than in the lidar study by Gerding et al. (2008). This small deviation might also be the result of tidal aliasing as tidal amplitudes are in the range 1 – 3 K in this altitude region.

The amplitudes of the AO estimated from lidar data above northern Germany are in good agreement with CIRA-86. In contrast, the AO amplitudes observed above Río Grande are smaller than the values reported by Fleming et al. (1990). The reason for the smaller amplitudes may be geophysical or it could also be caused by tidal aliasing which can both increase and decrease the amplitude of seasonal oscillations.

3.4 Summary and Answer to Research Question (R1)

In this chapter, attention was focused on the temperature background, in particular studying seasonal oscillations, PWs, and DTs. Defining this temperature background accurately is important for the derivation of realistic GW amplitudes and potential energies. Here again is the research question posed at the beginning:

(R1) Does the high cadence of CORAL measurements allow for the determination of planetary waves and tides in addition to annual and semi-annual oscillations and thus lead to better constraints on the temperature background?

Diurnal Tides

For the first time, amplitudes and phases of DTs were derived from irregularly sampled lidar temperature data in the middle atmosphere above Río Grande. To achieve this a novel technique has been developed which is inspired by the adaptive spectral filtering technique from [Stober et al. \(2017\)](#). The DT-R2D fit extracts the amplitude and phase of DTs in a running window over 9 days and 6 km in steps of 30 min and 500 m (see e.g. [Figure 3.7](#)). Reasonable agreement has been found between the DT derived from CORAL measurements and ERA5 data up to 60 km with monthly mean amplitudes of 2 K – 4 K in that altitude region (see [Figure 3.11](#)). This is consistent with previous findings at mid- to high-latitudes (see e.g. [Lübken et al., 2011](#), [Pancheva and Mukhtarov, 2011](#), [Kopp et al., 2015](#), [Baumgarten and Stober, 2019](#)) which suggests that the DT-R2D fit does a reasonable job in the stratosphere. Above 60 km, DT amplitudes derived from CORAL data have a minimum between 60 km to 80 km and continue to increase with altitude, exceeding amplitudes derived from SABER data ([Pancheva and Mukhtarov, 2011](#)). Enhanced amplitudes in CORAL data in the upper mesosphere might be due to a local anomaly or a leakage of variance from SDTs which are known to become dominant in this altitude region. The large standard deviation of the DT in CORAL data confirms the enhanced variability of DTs which was found in another lidar study ([Baumgarten and Stober, 2019](#)). However, it remains unclear to what degree large-scale ($\lambda_z > 15$ km) GWs and SDTs affect the retrieval of DTs and thus contribute to enhanced variability. Even though the DT-R2D fit does not require continuous measurements over 24 h, a certain level of data coverage must exist in order to extract DTs. This requirement leads to the fact that no DTs can be defined in the summer months and, more generally, whenever the measurement cadence is too low.

Identifying tides in lidar data is key to investigating the interaction of tides and GWs (e.g. [Baumgarten and Stober, 2019](#)) as tides do not only alter the buoyancy frequency ([Preusse et al., 2001](#)) but also the background wind field ([Baumgarten and Stober, 2019](#)). Most recently [Pautet et al. \(2021\)](#) observed the interaction of tides and GWs in the MLT region above Río Grande using OH-airglow.

To put it in a nutshell, CORAL’s measurement cadence is high enough to study DTs in winter, but not sufficient to analyze them in summer.

Planetary Waves

The temperature perturbations due to PWs, T_{PW} , as found in CORAL data are in close agreement to corresponding temperature perturbations in ERA5 data. A dominant period on the order of ~ 30 days is most likely due to a quasi-stationary wave-1. Strong zonal winds and wavenumbers larger than 1 lead to rather small refractive indices for PWs, which indicates that Rossby waves with larger wave numbers cannot propagate vertically. To bridge the majority of measurement gaps in CORAL data the DT-R2D fit window is 9 days long, which results in a suppression of temperature signals that have periods smaller than 9 days. CORAL's measurement cadence is high enough to resolve PWs with periods larger than 9 days but mostly insufficient to resolve waves with smaller periods.

Seasonal Oscillations

Within the considered period of time CORAL performed an average of 21 measurements each month which allowed for the robust determination of amplitudes and phases of the AO and SAO. It has been found that the AO exhibits a weaker peak at 32 km and a stronger peak at 88 km with the phases shifted by 6 months. This is consistent with previous observations. However, both oscillations are weaker than observed in CIRA-86, and the stratospheric (mesospheric) AO is stronger (weaker) than above Kühlungsborn which is conjugate in latitude to Río Grande. The SAO shows three maxima at heights of 41 km, 65 km and 88 km. The amplitudes of the SAO at these altitudes are significantly larger than reported in other studies (see e.g. [Fleming et al., 1990](#), [Gerding et al., 2008](#), [Zhang et al., 2017](#)). The amplitudes of DTs found are of such magnitude that they could explain the observed deviations of the seasonal oscillations by tidal aliasing. Also enhanced wave-1 activity at the beginning and end of the winter season is reported to cause leakage of variance to the SAO ([Gao et al., 1987](#), [Randel, 1988](#)).

Chapter 4

Internal Gravity Waves

Under quiet conditions the atmosphere is in hydrostatic equilibrium thanks to the balance between the pressure gradient force acting upwards and Earth's gravity acting downwards. If an air parcel is displaced vertically by an external force, a force imbalance occurs wherein the gravitational force counteracts the buoyancy. The air parcel starts to oscillate and wave motions are initiated. Such vertical displacements are for instance caused by deep convection, frontal zones and orography. The excited oscillation can be described as a wave packet with a finite extension in space and time that propagates away from its source. This work focuses on internal gravity waves with periods $f < \hat{\omega} < N$. In general, a wave packet consists of a spectrum of waves which disperses as it propagates through the atmosphere. Some spectral components of the wave packet may get trapped between levels of reflection, while other components may propagate unhindered deep into the middle atmosphere or beyond. The key aspect of wave propagation is the transport of energy and momentum over large distances in the vertical and horizontal.

4.1 Linear Gravity Wave Theory and Methods

In this section the equations to describe linear GWs are derived. The focus will be on the equations that are relevant to this work. The interested reader is also referred to Gill (1982), Nappo (2002), Fritts and Alexander (2003) and Holton (2004).

4.1.1 Dispersion Relation

Linear wave theory is based on three fundamental conservation laws of fluid dynamics:

1. Conservation of momentum is manifested in the Navier-Stokes equation which is given by

$$\frac{\partial \vec{u}}{\partial t} + \vec{u} \cdot \nabla \vec{u} + f(\hat{e}_z \times \vec{u}) = -\frac{1}{\rho} \nabla p - g \hat{e}_z + \vec{D}. \quad (4.1)$$

2. Conservation of mass is given by the continuity equation which states

$$\frac{\partial \rho}{\partial t} + \nabla(\rho \vec{u}) = 0. \quad (4.2)$$

3. Conservation of internal energy is given by

$$\frac{d\Theta}{dt} = Q. \quad (4.3)$$

The above equations together with the ideal gas law define a complete set and describe the dynamics of inviscid fluids. In above equations, \hat{e}_z refers to the unit vector in z -direction, \vec{D} and Q are forcing terms, and Θ is the potential temperature that an air parcel would have if brought adiabatically down to the Earth's surface. The **Navier-Stokes Equation (4.1)** states that air masses in the atmosphere are accelerated by the Coriolis force, the pressure gradient force, gravity, and an additional force which might be, for instance, a body force due to dissipating waves. The **continuity equation (4.2)** relates an increasing (decreasing) density in a fixed volume to mass convergence (divergence). **Equation (4.3)** states that the potential temperature of an air parcel changes only if energy is exchanged with its surroundings.

In order to solve the system of equations, as a first step (4.1) – (4.3) are linearized by carrying out a Reynolds decomposition such that any atmospheric variable can be written as $\Phi = \bar{\Phi}(z) + \Phi'(x, y, z, t)$, i.e. a background or mean state parameter $\bar{\Phi}$ that depends solely on altitude and a perturbation Φ' . A special condition is only imposed on w , in which $\bar{w} = 0$. Any derivatives of the background components with respect to x, y, t are zero, and only the derivatives of the perturbation components remain. Also, it is assumed that the background atmosphere is in hydrostatic equilibrium, i.e.

$$\frac{d\bar{p}}{dz} = -\bar{\rho}g. \quad (4.4)$$

Furthermore, it is assumed that atmospheric variables u', v', w', θ' change slowly in comparison to the spatial and temporal extent of a wave such that the temporal derivative

of $\bar{\Phi}$ is zero. This is referred to as the WKB¹ approximation. After linearizing (4.1) – (4.3) and under the given assumptions, they can be solved using a wave ansatz of the form

$$\Phi' = \tilde{\Phi} \exp(i(kx + ly + mz - \omega t) + \alpha_h z) \quad \text{with} \quad \alpha_h = \frac{1}{2H_s} \quad (4.5)$$

where $\vec{k} = (k, l, m)^T$ is the wave vector, $\omega = \hat{\omega} + \vec{k}\vec{u}$ is the observed (Eulerian) wave frequency, and $\tilde{\Phi}$ is the amplitude of the wave which is also a function of x, y, z, t . Plugging (4.5) into the linearized (4.1) – (4.3) the *polarization relations* are obtained and given as

$$\tilde{u} = \begin{pmatrix} i\hat{\omega}k - fl \\ i\hat{\omega}l + fk \end{pmatrix} \tilde{v} \quad (4.6)$$

$$\tilde{p} = \begin{pmatrix} \hat{\omega}^2 - f^2 \\ \hat{\omega}k + ifl \end{pmatrix} \tilde{u} = \begin{pmatrix} \hat{\omega}^2 - f^2 \\ \hat{\omega}l - ifk \end{pmatrix} \tilde{v} \quad (4.7)$$

$$\tilde{w} = \frac{-\hat{\omega}}{N^2 - \hat{\omega}^2} \left(m + i \left(\alpha_h - \frac{g}{c_s^2} \right) \right) \tilde{p} = \frac{-\hat{\omega}(m + i\alpha_h)}{N^2 - \hat{\omega}^2} \tilde{p} \quad (4.8)$$

$$\tilde{w} = i \frac{g\hat{\omega}}{N^2} \tilde{\Theta}, \quad (4.9)$$

where c_s is the speed of sound which is let go to infinity on the right side of (4.8). This set of equations relates the wave perturbation amplitudes of the different variables to one another. The GW dispersion relation that connects the wave's intrinsic frequency with its wavelength results from the combination of the polarization relations and is given by

$$\hat{\omega}^2 = \frac{N^2(k^2 + l^2) + f^2(m^2 + \alpha_h^2)}{k^2 + l^2 + m^2 + \alpha_h^2}. \quad (4.10)$$

Equation (4.10) can be simplified by defining a horizontal wavenumber in the direction of the wave vector $k_h = \sqrt{k^2 + l^2}$ and assuming hydrostatic waves via setting $m \gg \alpha_h$:

$$\hat{\omega}^2 = \frac{N^2 k_h^2 + f^2 m^2}{k_h^2 + m^2} \quad (4.11)$$

$$= \frac{N^2 k_h^2}{m^2} + f^2 \quad \text{using} \quad m > k_h. \quad (4.12)$$

In the mid-frequency ($N \gg \hat{\omega} \gg f$) regime, the dispersion relation simplifies to

$$\hat{\omega}^2 = \frac{N^2 k_h^2}{m^2}. \quad (4.13)$$

The intrinsic frequency is the Brunt-Väisälä frequency scaled with the aspect ratio which is the relation between the vertical and horizontal wavelengths. One realizes that as the aspect ratio becomes smaller, i.e. waves propagate more in the horizontal domain, effects due to the Earth's rotation have to be taken into account.

¹Named after Wentzel, Kramers and Brillouin

4.1.2 Phase and Group Velocity

The observed phase velocity in the mid-frequency regime is

$$\begin{pmatrix} c_{\text{ph}} \\ c_{\text{pz}} \end{pmatrix} = \begin{pmatrix} u_{\parallel} \\ 0 \end{pmatrix} + \hat{\omega} \begin{pmatrix} k_{\text{h}}^{-1} \\ m^{-1} \end{pmatrix}, \quad (4.14)$$

where u_{\parallel} is the horizontal wind parallel to the wave vector. Please note that the level where $c_{\text{ph}} = u_{\parallel}$ is a critical level at which $m \rightarrow \infty$. However, since instabilities and dissipation start before the critical level is reached, this limit is actually never reached in the real atmosphere (Dörnbrack and Nappo, 1997, Fritts and Alexander, 2003). The observed group velocity is defined as

$$\begin{pmatrix} c_{\text{gh}} \\ c_{\text{gz}} \end{pmatrix} = \begin{pmatrix} u_{\parallel} \\ 0 \end{pmatrix} + \begin{pmatrix} \partial\hat{\omega}/\partial k_{\text{h}} \\ \partial\hat{\omega}/\partial m \end{pmatrix} \quad (4.15)$$

$$= \begin{pmatrix} u_{\parallel} \\ 0 \end{pmatrix} + \hat{\omega} \begin{pmatrix} k_{\text{h}}^{-1} \\ -m^{-1} \end{pmatrix} \stackrel{MW}{=} \begin{pmatrix} u_{\parallel} \\ 0 \end{pmatrix} - u_{\parallel} \begin{pmatrix} 1 \\ -k_{\text{h}}/m \end{pmatrix}, \quad (4.16)$$

where $c_{\text{ph}} = 0$ is used in the last step in order to derive group velocities for stationary MWs. It becomes evident that as $c_{\text{gh}} = 0$, waves in the mid-frequency regime are non-dispersive. Besides, with energy being transported in the direction of group velocity, the fact that $c_{\text{pz}} = -c_{\text{gz}}$ shows that with upward phase progression, energy is transported downward and vice versa. MWs in this regime have rather small horizontal wavelengths (< 100 km) and propagate merely vertically as $c_{\text{gh}}/c_{\text{gz}} = 0$.

The observed phase velocity in the low-frequency regime ($\hat{\omega} \sim f$) is identical to (4.14), but the observed group velocity is given as

$$\begin{pmatrix} c_{\text{gh}} \\ c_{\text{gz}} \end{pmatrix} = \begin{pmatrix} u_{\parallel} \\ 0 \end{pmatrix} + \frac{N^2 k_{\text{h}}}{m^2 \hat{\omega}} \begin{pmatrix} 1 \\ -k_{\text{h}}/m \end{pmatrix} \stackrel{MW}{=} \begin{pmatrix} u_{\parallel} \\ 0 \end{pmatrix} - \frac{N^2}{m^2 u_{\parallel}} \begin{pmatrix} 1 \\ -k_{\text{h}}/m \end{pmatrix}, \quad (4.17)$$

where again $c_{\text{ph}} = 0$ is used in the last step to derive group velocities for MWs. In the low-frequency regime $c_{\text{gh}} \neq 0$ which means that waves in this regime are dispersive. MWs in this regime have rather large horizontal wavelengths (> 100 km) and propagate both in the vertical but also in the horizontal since $c_{\text{gh}}/c_{\text{gz}} > 0$. As an illustration, Figure 1.4 depicts the topography of the Southern Andes and the two wave regimes above. Queney (1948) and Gill (1982) also refer to the low-frequency regime as the rotating wave regime as therein the rotation of the Earth is not negligible, and the mid-frequency regime is referred to as the nonrotating wave regime. The hydrostatic nonrotating waves appear right above the mountain peaks, for example above Mt. Darwin and Mt. Fitz Roy. These waves exhibit horizontal wavelengths that are of the same order as their vertical wavelengths as long as \vec{u} and N remain constant. The further away the wave source is, the less likely it is to observe hydrostatic nonrotating waves above Río Grande. Waves in the hydrostatic rotating wave regime exhibit horizontal wavelengths that are significantly longer than their vertical wavelengths and originate from the envelope of the Southern Andes topography rather than from individual mountain peaks. These waves extend leeward of the mountains including over Río Grande where CORAL can observe them. The spreading of MWs leeward of the mountains was observed by Dörnbrack et al. (1999) in Scandinavia but is also reported for the Southern Andes region in publications by e.g. Jiang et al. (2013), Wright et al. (2017) and Kaifler et al. (2020b).

4.1.3 Gravity Wave Potential Energy

The total energy per unit mass of an internal GW is defined as

$$E = \frac{1}{2} \overline{(u^2 + v^2 + w^2)} + \frac{1}{2} \frac{g^2}{N^2} \overline{\left(\frac{\rho'}{\rho_0}\right)^2} \quad (4.18)$$

in which the first term represents the perturbation kinetic energy and the second term the perturbation potential energy (Gill, 1982, Nappo, 2002). Density and temperature are connected via the ideal gas law. Thus, the potential energy can also be written as

$$E_p = \frac{1}{2} \frac{g^2}{N^2} \overline{\left(\frac{T'}{T_0}\right)^2}, \quad (4.19)$$

where g is a function of altitude. The analysis of wave energy is limited to the GW potential energy E_p as no observations of winds are provided. E_p is often used as proxy for GW activity in lidar observations (e.g. Wilson et al., 1991, Whiteway and Carswell, 1995, Whiteway et al., 1997, Alexander et al., 2011, Mz  et al., 2014, Kaifler et al., 2015b, Baumgarten et al., 2017). The GW potential energy is proportional to the squared GW-induced relative temperature perturbations T'/T_0 which is the perturbation amplitude T' divided by the background temperature T_0 . In order to derive E_p , measured temperatures are first separated into contributions from background and GW-induced perturbations. The temperature background is accurately defined in the previous chapter. However, in order to ensure that results are comparable with other studies and to be independent of the measurement coverage, the temperature background is defined as $T_0 = \bar{T} + T_{SO} + T''$. In addition, only those temperature perturbations are considered with vertical scales smaller than 15 km. Wave energies based on this rather conventional cutoff are compared to “realistic” wave energies which are based on the predefined temperature background in Section 4.3.4. The term “realistic” in connection with wave energies is used only to distinguish from conventional wave energies, which tend to be underestimated on average. No claim is made that these are indeed correct wave energies.

The overbar in (4.19) denotes that E_p is averaged over at least one cycle of a GW, i.e. in case of lidar measurements one period or one vertical wavelength. Following Whiteway and Carswell (1995), the mean-square relative temperature perturbations are defined as

$$\overline{\left(\frac{T'}{T_0}\right)^2}_{kl} = \frac{1}{n_t n_z} \sum_{i=k-\frac{n_t}{2}}^{k+\frac{n_t}{2}} \sum_{j=l-\frac{n_z}{2}}^{l+\frac{n_z}{2}} \left(\frac{T'}{T_0}\right)^2_{ij} \quad (4.20)$$

where k and l denote the discrete location in time and altitude at which the evaluation is done. The indices i and j run over the averaging window containing n_t and n_z lidar temperature observations where $\Delta t = n_t \cdot \delta t = 3$ h and $\Delta z = n_z \cdot \delta z = 15$ km with $\delta z = 100$ m in the vertical and $\delta t = 15$ min in time. The value of $\Delta z = 15$ km is chosen in accordance with λ_{cut} and $\Delta t = 3$ h is chosen according to the required minimum measurement duration.

The root-mean square (RMS) is commonly used in electrical engineering to describe the average power of an alternating current that is dissipated by an electrical resistance (Daintith, 2009). If the amplitude of a pure sine-wave is 1 then the RMS amplitude is $1/\sqrt{2}$.

This fact is used in the comparison of wave amplitudes in [Section 5.2.3](#). In analogy, here the RMS is used to describe the mean GW potential energy of the wave field. In addition, it is required that at least 90% of the averaging window is filled with data. The arithmetic mean E_p (represented in the following by \diamond) is computed as

$$\langle E_p \rangle_{kl}^{\diamond} = \frac{1}{n_t n_z} \sum_{i=k-\frac{n_t}{2}}^{k+\frac{n_t}{2}} \sum_{j=l-\frac{n_z}{2}}^{l+\frac{n_z}{2}} E_{p,ij}. \quad (4.21)$$

For instance, [Baumgaertner and McDonald \(2007\)](#) have shown that the E_p distribution follows a lognormal distribution based on six months of data such that the arithmetic mean is not an optimal measure of the GW activity. In this case a geometric mean is better suited. Hence, to describe the average E_p over long time scales, i.e. months or years, the geometric mean E_p (represented in the following by \odot) is computed as

$$\langle E_p \rangle_{kl}^{\odot} = \exp \left(\frac{1}{n_t n_z} \sum_{i=k-\frac{n_t}{2}}^{k+\frac{n_t}{2}} \sum_{j=l-\frac{n_z}{2}}^{l+\frac{n_z}{2}} \ln(E_{p,ij}) \right). \quad (4.22)$$

In addition, the standard deviation and the skewness of the lognormal distribution is determined according to

$$\sigma_{kl}^{\odot} = \sqrt{\frac{1}{n_t n_z} \sum_{i=k-\frac{n_t}{2}}^{k+\frac{n_t}{2}} \sum_{j=l-\frac{n_z}{2}}^{l+\frac{n_z}{2}} \left(\ln(E_{p,ij}) - \ln(\overline{E_{p,kl}}^{\odot}) \right)^2} \quad (4.23)$$

and

$$\gamma_{kl}^{\odot} = \frac{1}{n_t n_z} \sum_{i=k-\frac{n_t}{2}}^{k+\frac{n_t}{2}} \sum_{j=l-\frac{n_z}{2}}^{l+\frac{n_z}{2}} \left(\ln(E_{p,ij}) - \ln(\overline{E_{p,kl}}^{\odot}) \right)^3. \quad (4.24)$$

Skewness provides information on whether the distribution is inclined towards large or low energy densities. Therefore, it also offers details about the GW intermittency. According to [Plougonven et al. \(2013\)](#) a reliable measure for the GW intermittency is the Gini coefficient. It is defined as

$$I_g = \frac{\sum_{i=1}^{n-1} \left(i \overline{E_p}^{\diamond} - \mathbb{E}_{p,i} \right)}{\sum_{i=1}^{n-1} i \overline{E_p}^{\diamond}} \quad (4.25)$$

where \mathbb{E}_p is the cumulative sum over E_p values sorted in ascending order and $n = n_t n_z$ is the number of those E_p values that are included in the cumulative sum. Calculations of the respective uncertainties are given in [Appendix C](#).

4.1.4 Conservation of GW Momentum

If there is no wave dissipation, in the presence of a vertically varying background atmosphere the gravity wave pseudomomentum flux (GWMF) can be considered a constant

(Fritts and Alexander, 2003). The vertical flux of horizontal pseudomomentum is given as

$$\begin{pmatrix} F_{\text{px}} \\ F_{\text{py}} \end{pmatrix} = \varrho \left(1 - \frac{f^2}{\hat{\omega}^2} \right) \begin{pmatrix} \overline{u'w'} \\ \overline{v'w'} \end{pmatrix}. \quad (4.26)$$

In order to express the GWMF in terms of wavenumbers and E_p the polarization relations (4.6) – (4.9) are used (see (Ern et al., 2004)). The total GWMF is then given as

$$F_{\text{ph}} = \sqrt{F_{\text{px}}^2 + F_{\text{py}}^2} = \left(1 - \frac{\hat{\omega}^2}{N^2} \right) \frac{k_h}{m} \varrho E_p. \quad (4.27)$$

If the intrinsic frequency (4.12) for low-frequency GWs is plugged in one gets

$$F_{\text{ph}} = \left(1 - \frac{k_h^2}{m^2} - \frac{f^2}{N^2} \right) \frac{k_h}{m} \varrho E_p. \quad (4.28)$$

It follows that $E_p \sim \frac{1}{\varrho} \frac{m}{k_h}$, meaning that as ϱ decreases with height E_p increases to keep the pseudomomentum flux constant. This is only valid if the aspect ratio i.e. m/k_h remains constant as well. Generally this is not the case as varying atmospheric background conditions lead to changes in m and k_h (Marks and Eckermann, 1995).

Ideally, one would like to make a statement whether GWs dissipate or not based on the E_p profile. Previous studies compared their E_p profiles to the conservative growth rate (e.g. Rauthe et al., 2006, Alexander et al., 2011, Mz e et al., 2014, Kaifler et al., 2015b, Wright et al., 2016, Chu et al., 2018). It was used to approximate the growth of potential energy due to the decrease of air density and is given as

$$E_p(z) = E_0 \exp\left(\frac{z}{H_s}\right), \quad (4.29)$$

where E_0 is an initial energy. The scale height H_s was either determined from an average temperature (Alexander et al., 2011, Mz e et al., 2014, Kaifler et al., 2015b, Wright et al., 2016) or was fitted to the E_p profiles (Chu et al., 2018), but it was always considered to be constant with height. This implies the assumption of an isothermal atmosphere as well as a uniform horizontal wind speed in order to keep m/k_h constant. These assumptions are not very realistic. Hence, conservative growth curves as function of temperature are calculated. The scale height $H_s(z) = \frac{RT(z)}{Mg}$ is calculated using the monthly mean temperature profiles shown in Figure 2.5. The symbol R is the universal gas constant and $M = 29.0 \text{ g mol}^{-1}$ is the mean mass of one mol of the atmosphere. Nevertheless it has to be assumed that there are no shears in the horizontal wind field and that u changes with the same rate as N in order to ensure a constant aspect ratio. These assumptions are still unrealistic but closer to reality than in previous studies. After all, conservative growth curves as a function of temperature give a more realistic but still only rough estimation of the expected growth of wave amplitudes in the absence of dissipation. It is obvious that E_p cannot become indefinitely large where the air density approaches zero at large altitudes. At some point there will be wave dissipation, for instance when there arises a self-induced shear instability or an unstable lapse rate (Dunkerton, 1982). Most of the CORAL data show growth rates which are smaller than conservative growth rates,

suggesting possible wave dissipation. Another explanation for smaller growth rates is oblique wave propagation (Kalisch et al., 2014). Here, GWs exit the observational volume at some altitude, causing lower measured E_p values above. Based on the measurement data, the two processes cannot be distinguished. If waves exit the observational volume at some altitude due to oblique propagation, there is also a certain possibility that waves can enter the volume. This convergence can lead to locally increased E_p values and might even result in growth rates larger than conservative growth rates.

4.1.5 1D Wavelet transformation

Fourier showed that any periodic signal can be written as a sum of sine and cosine functions. The Fourier transform is given as

$$\hat{f}(\omega) = \frac{1}{\sqrt{2\pi}} \int_{-\infty}^{\infty} f(t)e^{-i\omega t} dt \quad (4.30)$$

and reveals spectral information about the input signal $f(t)$. The downside is that the frequency is not available as function of time. Hence, the windowed or short-time Fourier transform was developed to retain the temporal information of the spectral signature. However, due to the fixed width of the window the retrieved frequencies are limited, for example periods can not be larger than the window width. To overcome this problem, the continuous wavelet transform (CWT) was developed (Farge, 1992). The CWT uses a mother wavelet that is scaled and translated and thus a larger domain of the signal is analyzed when large periods are retrieved. A common mother wavelet is the Morlet wavelet which is a plane wave modulated by a Gaussian. It is given as

$$\psi_0(\eta) = \pi^{-1/4} e^{i\omega_0 \eta} e^{-\eta^2/2} \quad \text{and} \quad (4.31)$$

$$\psi \left[\frac{(\nu' - \nu)\delta t}{\mu} \right] = \sqrt{\frac{\delta t}{\mu}} \psi_0 \left[\frac{(\nu' - \nu)\delta t}{\mu} \right], \quad (4.32)$$

where ω_0 is the nondimensional frequency and η the nondimensional time parameter (Torrence and Compo, 1998). Equation (4.32) shows how the wavelet is scaled via the parameter μ and translated via ν . The sampling of the input signal is given by δt . The factor in front derives from normalization. The CWT of a discrete series of measurements f_k is obtained by calculating the convolution with a translated and scaled version of the mother wavelet. The wavelet transform is given by

$$W_\nu(\mu) = \sum_{\nu'=0}^{N-1} f_{\nu'} \psi^* \left[\frac{(\nu' - \nu)\delta t}{\mu} \right] \quad (4.33)$$

where the symbol $*$ indicates the complex conjugate. The scales are defined as $\mu_j = \mu_0 2^{j\delta j}$ with $\mu_0 = 2\delta t$ and $\delta j = 1/8$. Instead of computing the convolution in the time domain, it is faster to do a point-wise multiplication of the two signals in the frequency domain. Thus, the CWT can also be defined as

$$W_\nu(\mu) = \sum_{k=0}^{N-1} \hat{f}_k \hat{\psi}^*(\mu\omega_k) e^{i\omega_k \nu \delta t}. \quad (4.34)$$

Figure 4.1 shows the real parts of two Morlet wavelets with different scales and their representation in the frequency domain. It is important to understand that the choice of ω_0 determines how many oscillations the wavelet has and thus determines the degree of uncertainty in the time and frequency domain. The choice of $\omega_0 = 4$ results in a rather poor frequency resolution, but it is known that the vertical wavelength of GWs changes rapidly in a region of large vertical wind shear. Therefore, more emphasis is put on the spatial resolution.

It is also possible to filter spectral amplitudes in the frequency domain and reconstruct the filtered signal afterwards. The reconstructed signal is then

$$f_\nu = \frac{\delta j \sqrt{\delta t}}{C_\delta \psi_0(0)} \sum_{j=0}^J \frac{\Re(W_\nu(\mu_j))}{\sqrt{\mu_j}} \quad (4.35)$$

where $\Re(W_\nu(\mu_j))$ is the real part of the wavelet transform and C_δ is a constant factor that originates from the reconstruction of a δ -function. The interested reader may be referred to [Torrence and Compo \(1998\)](#).

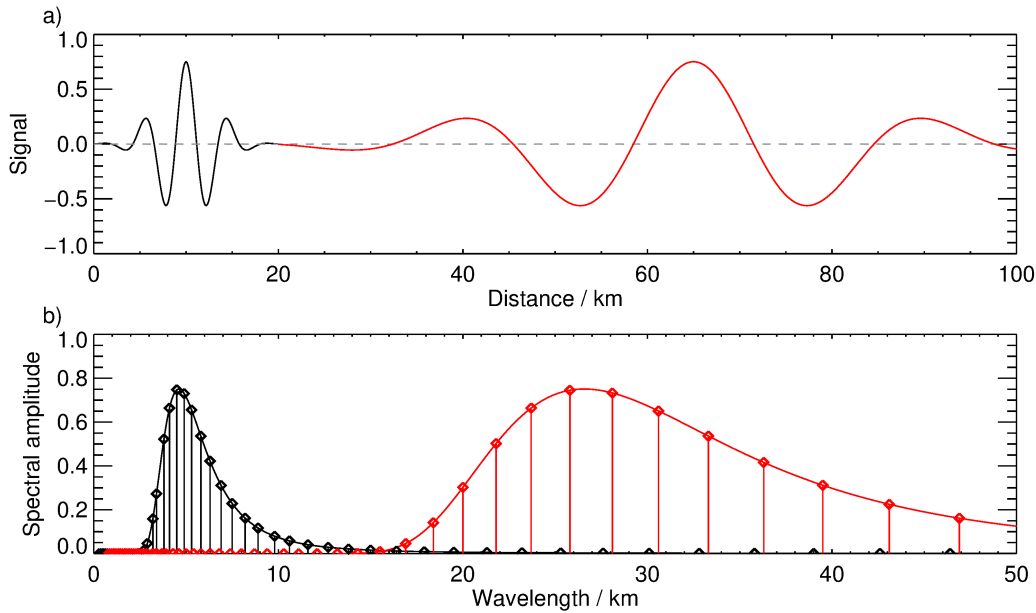


Figure 4.1: a) Real part of two Morlet wavelets with $\omega_0 = 4$ and $\mu = 5$ km (black) and $\mu = 25$ km (red) and their Fourier transform (b). Vertical lines and dots in (b) represent the discrete scales μ_j used in the CWT.

4.1.6 2D Wavelet transformation

The CWT can also be extended in two dimensions (e.g. [Chen and Chu, 2017](#)) such that

$$W_{\vec{n}}(s, \vartheta) = \sum_{n'=0}^{N-1} \sum_{m'=0}^{M-1} f_{n'm'} \psi^* \left(\mathcal{R}_\vartheta^{-1} \frac{(\vec{n}' - \vec{n}) \vec{\delta} t}{s} \right) \quad (4.36)$$

where $\mathcal{R}_\vartheta = \begin{pmatrix} \cos \vartheta & -\sin \vartheta \\ \sin \vartheta & \cos \vartheta \end{pmatrix}$ is an additional rotation of the 2D wavelet and $\vec{n} = (n, m)^T$ and $\vec{\delta t} = (\delta t, \delta z)^T$ are translation and sampling vectors in two dimensions e.g. time and altitude. [Figure 4.2](#) shows examples of 2D wavelets with different orientations. The direction of the wave vector in (t, z) -space is defined by the angle ϑ and the scale μ corresponds to the period along this direction. The angle ϑ is defined anti-clockwise where $\vartheta = 90^\circ$ represents a wavelet with stationary phaselines. Other orientations can be converted into vertical phase speeds c_{pz} according to $c_{pz} = \frac{\delta z}{\delta t} \tan \vartheta$. A 2D CWT is not only performed for different translations and scales but also for rotations.

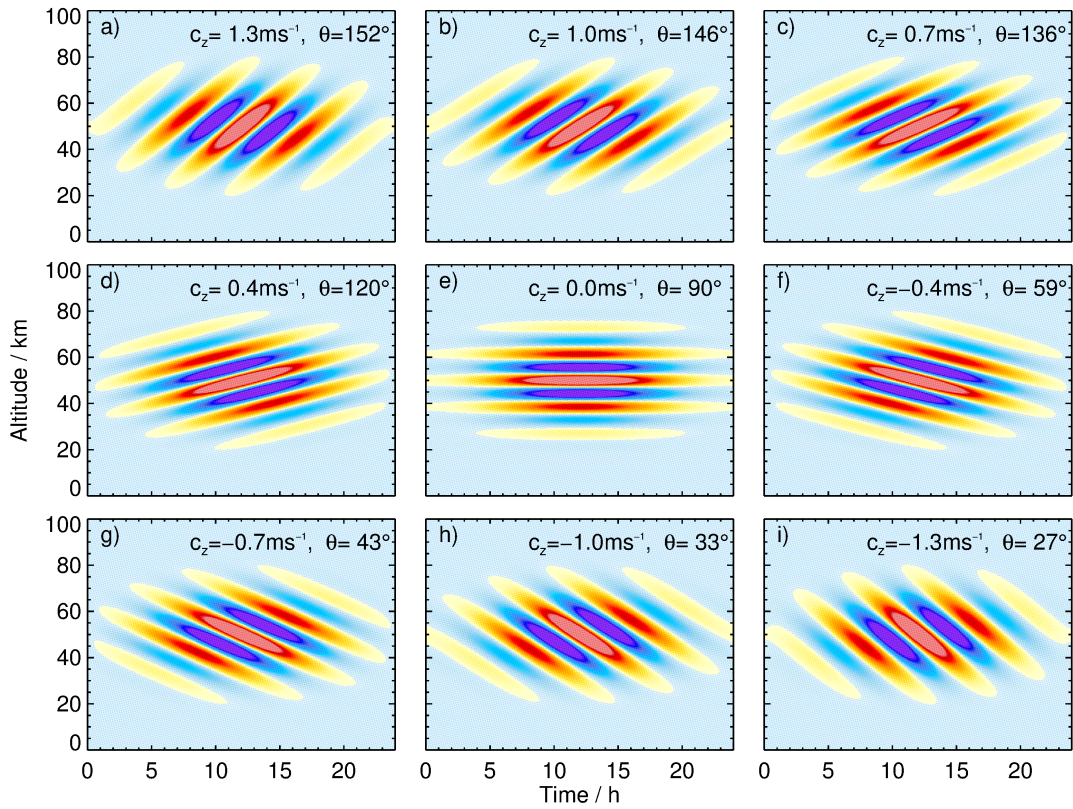


Figure 4.2: Examples of 2D Morlet wavelets in (t, z) -space. The chosen scale refers to a vertical wavelength of 10 km in case of $\vartheta = 90^\circ$. Illustrated are four wavelets with positive vertical phase speeds (a – d) referring to apparently downward propagating waves, one stationary wavelet (e) referring to mountain waves and four wavelets with negative vertical phase speeds (f – i) referring to apparently upward propagating waves.

4.1.7 WAVELET-SCAN

Vertical wavelengths of GWs generally vary in time as well as in altitude while interacting with the background wind field (e.g. [Marks and Eckermann, 1995](#), [Bühler, 2014](#)). Besides, multiple waves can superimpose or even interact non-linearly, leading to complex

wave patterns in lidar temperature data. Although the 1D wavelet analysis preserves the altitude information of spectral modes, so far lidar studies have focused mostly only on dominant modes and neglected weaker ones (e.g. Baumgarten et al., 2017, Kaifler et al., 2017). Here, a new method is described that is based on 1D wavelet analysis but also keeps track of the temporal and vertical changes of more than one coherent spectral mode by utilizing a clustering algorithm. This novel method is called WAVELET-SCAN.

In a first step, a temperature profile is analyzed in the vertical using CWT. As mother wavelet the Morlet wavelet is used. To fulfill the admissibility condition, i.e. the integral over the wavelet is zero, ω_0 is set to 4. Input scales are defined as in Section 4.1.5 with $\delta z = 1.0$ km and output scales, i.e. vertical wavelengths, are interpolated onto a linear grid. The results of the CWT are spectral amplitudes as function of altitude and vertical wavelength $W_z(\lambda_z)$. The underlying structure or “skeleton” (Torrésani, 1995) is determined by identifying local maxima in spectral amplitude in the direction of vertical wavelength, i.e. a zero-crossing from positive to negative values in $\frac{\partial W_z}{\partial \lambda_z}$. This step is repeated for all consecutive temperature profiles obtained in one measurement night and yields first $W_{t,z}(\lambda_z)$ and second a “skeleton” in the (t, z, λ_z) -space. In addition, it is required that $W_{t,z}(\lambda_z) > 3.0$ K and $W_{t,z}(\lambda_z) > \frac{\Delta T}{2}$ in order to minimize the contribution by tides and measurement uncertainties. The derivation of the “skeleton” is illustrated in Figure 4.3. Figure 4.3e shows an example of sub-seasonal temperature perturbations \tilde{T} on the night of 18 to 19 June 2018. Clearly, large-amplitude waves were observed on this date. As described above, CWTs are applied to all vertical profiles and subsequently $W_{t,z}(\lambda_z)$ is averaged to illustrate the three dimensional structure. In Figures 4.3a, c $W_{t,z}(\lambda_z)$ is averaged between 55 km and 95 km and between 15 km and 55 km, respectively. In Figures 4.3b, d $W_{t,z}(\lambda_z)$ is averaged over the first half of the night (22 UTC – 05 UTC) and the second half of the night (05 UTC – 12 UTC), respectively. With this arrangement the walls of the box representing $W_{t,z}(\lambda_z)$ are illustrated and one gets a good insight into its structure.

Multiple maxima exist in $W_{t,z}(\lambda_z)$ and ultimately form hypersurfaces in (z, t, λ_z) . The challenge is to identify those hypersurfaces which represent in physical space wave packets that may exhibit varying vertical wavelengths in time and altitude. This problem is solved by implementing a clustering algorithm as the second step of WAVELET-SCAN.

The Density-Based Spatial Clustering of Applications with Noise (DBSCAN) is able to separate densely packed data points with many nearby neighbors from isolated outliers (Ester et al., 1996). The critical value that has to be defined is the data point density. It is defined as the minimum number of points, *minPts*, that must be within a neighborhood of radius ν of any point. Normalizing by δt , δz , and $\delta \lambda_z$, the (t, z, λ_z) -space is represented as a Cartesian grid with unit distance $\nu = 1$. As the data points represent maxima in the λ_z -direction, the minimum distance between two adjacent maxima in that direction is $\nu = 2$. To ensure that only one λ_z for each time and altitude is identified, $\nu = \sqrt{2}$ and *minPts* = 7 is chosen. These settings turn out best for the problem at hand and result in a sufficient identification of coherent wave packets. For further details on the functionality of the DBSCAN the reader is referred to Ester et al. (1996).

After a wave packet is identified, it is required that its temporal and vertical extent is larger than 3 h and larger than the average vertical wavelength, respectively. This is to ensure that the packet performs at least one full oscillation in the vertical direction.

To demonstrate its capabilities WAVELET-SCAN is applied to artificial temperature data (see App. B) as well as to consecutive \tilde{T} -profiles that were obtained on the night from 18 to 19 June 2018. The output is information on a number of wave packets that represent multiple coherent spectral modes. For each wave packet, vertical wavelengths, spectral amplitudes and the cone of influence (COI) are retrieved. The COI describes the part of the wavelet spectrum where the determined spectral amplitudes are generally underestimated due to edge effects and are thus less reliable.

The sub-seasonal temperature perturbations (Fig. 4.3e) belong to a series of measurements that were conducted between 16 June and 23 June, 2018. In that period of time the mean vertical wavelength is 16 km (Kaifler et al., 2020b). The spectral analysis of \tilde{T} on 18 – 19 June 2018 performed by WAVELET-SCAN reveals more details. Superimposed coherent wave packets are revealed by the distributions of vertical wavelengths and by the reconstructions (Fig. 4.4a-d). The first packet extends over the whole altitude range and measurement duration. WAVELET-SCAN actually identifies three packets (I – III) separated by two measurement gaps, but as the reconstructed wave patterns demonstrate, the three identified packets belong to one single wave packet. This wave packet is responsible for the largest spectral amplitudes in the wavelet spectra (see red ellipses in Figure 4.3a, c, and d). Its average vertical wavelength is 12 km at the beginning of the measurement and the spectral amplitude starts with about 17 K. With progressing time the vertical wavelength shrinks to 9 – 10 km and the amplitude decreases to about 10 K until ~0700 UTC. At 0900 UTC the wave packet is confined to altitudes above 50 km and exhibits significantly shorter vertical wavelengths on the order of 6 km. That first wave packet dominates \tilde{T} and is linked to a strong mountain wave event (Kaifler et al., 2020b). Please note that spectral amplitudes in Figures 4.3a-d and Figures 4.4a, c are systematically underestimated. This is due to the fact that the variance of the signal is distributed over several scales because, in contrast to a pure sine function, the wavelet is spectrally broad (see also Fig. 4.1b). But as only one scale is reconstructed, the variance of the reconstructed signal is smaller than the variance of the input signal. It is unclear whether the last two packets (IV, V) are actually parts of one single wave packet that is divided by the measurement gap. But both packets show similar vertical wavelengths and hence they are shown next to each other. Wave packet IV (see green ellipse in Fig. 4.3a) appears between 0100 UTC and 0430 UTC in the altitude range 55 – 90 km. It has a vertical wavelength of 16 – 18 km and spectral amplitudes below 4 K. After the second measurement gap wave packet V (see orange ellipses in Fig. 4.3a-c) spans the whole altitude range with vertical wavelengths of 17 km decreasing to 11 km within three hours. Its largest spectral amplitude is 17 K.

The vertical wavelength of linear hydrostatic MWs can be considerably longer than λ_{cut} as evident from the approximation $\lambda_z = 2\pi \frac{u}{N}$ (Nappo, 2002): For example, assuming a realistic westerly wind of 70 m s^{-1} and a stratospheric $N = 0.02 \text{ s}^{-1}$ results in $\lambda_z = 22 \text{ km}$ in case of a westward propagating wave. Also, the extreme wave profiles in Figure 2.5 indicate vertical wavelengths on the order of 20 km. Therefore, WAVELET-SCAN is not applied to T' but to \tilde{T} in order to be sensitive to GWs with vertical wavelengths longer than λ_{cut} .

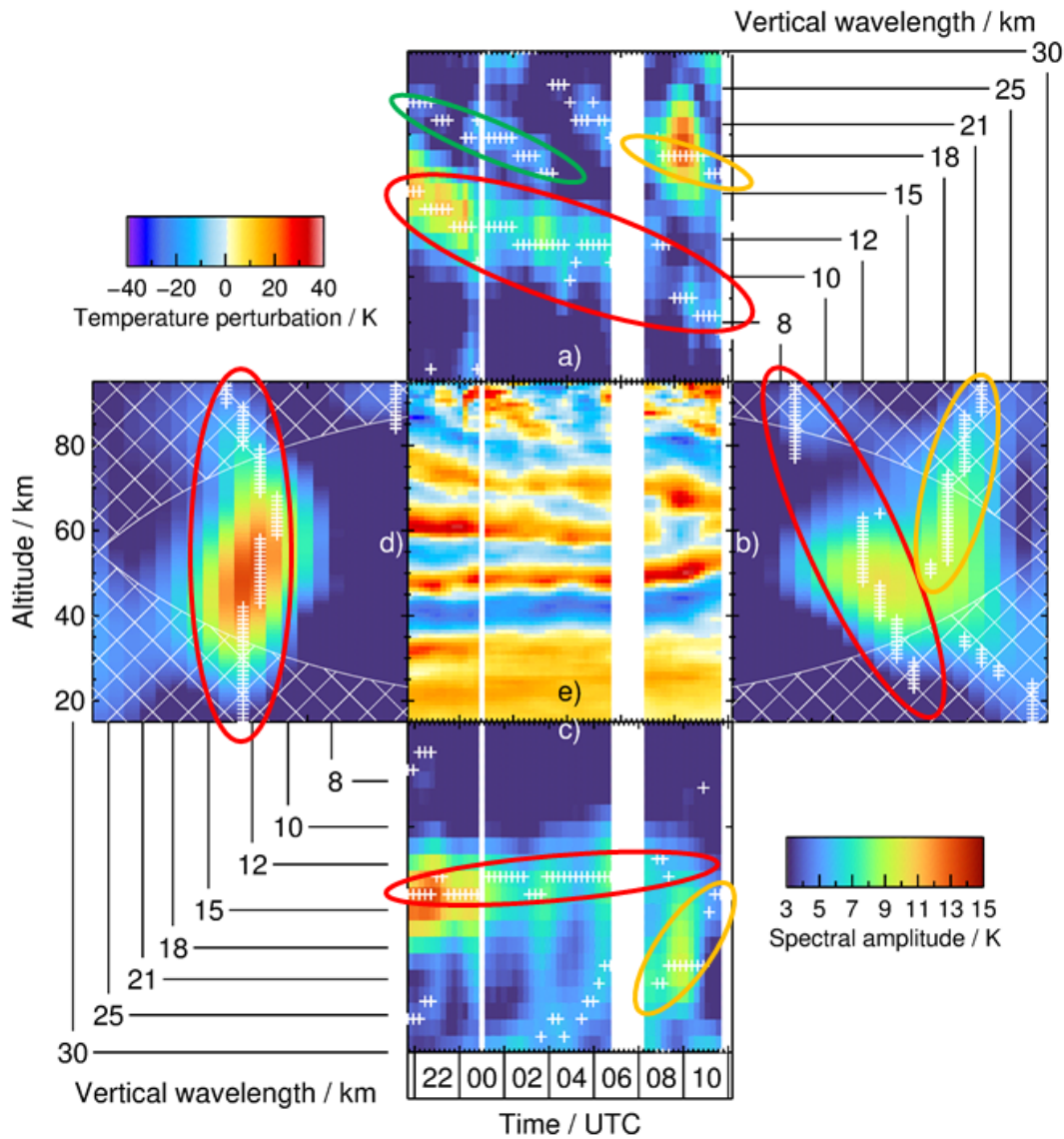


Figure 4.3: Wavelet spectrum averaged over altitudes 55 – 95 km (a) and altitudes 15 – 55 km (c), and averaged from 22 UTC to 05 UTC (d) and from 05 UTC to 12 UTC (b). Sub-seasonal temperature perturbations \hat{T} on 18 – 19 June 2018 are shown in (e). The hatched areas mark the cone of influence. White crosses mark local maxima in spectral amplitude. The red, green and orange ellipses highlight wave packets I – III, IV and V.

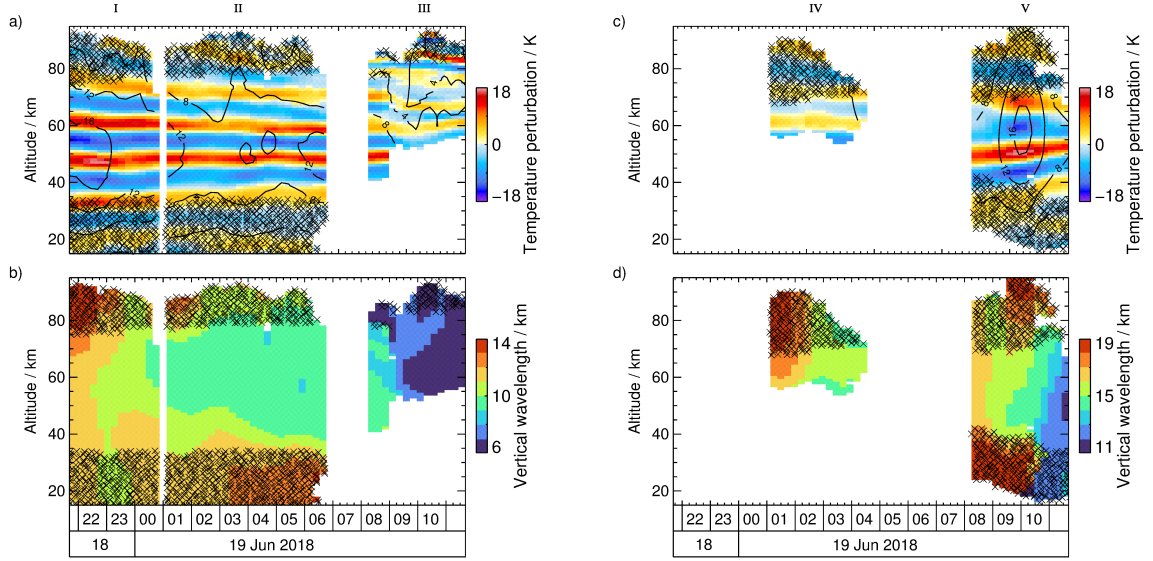


Figure 4.4: Analysis of the measurements on 18 – 19 June 2018 shown in [Figure 4.3e](#) based on WAVELET-SCAN: a) reconstructed wave packets with contour lines indicating spectral amplitudes, b) derived vertical wavelength of wave packets I – III. Panels c), d) display the same as a), b) but for wave packets IV and V. Hatched areas mark the COI. Please note different λ_z -ranges for b) and d).

4.1.8 2D Kernel Density Estimation

To estimate the probability density function (PDF) of a random variable, one can use a kernel density estimator (KDE). [Rosenblatt \(1956\)](#) and [Parzen \(1962\)](#) define the KDE as

$$\hat{f}(z; h) = \frac{1}{n} \sum_{i=1}^n K_h(z - z_i) \quad (4.37)$$

$$\hat{f}(z, \lambda; h) = \frac{1}{n} \sum_{i=1}^n K_h(z - z_i, \lambda - \lambda_i), \quad (4.38)$$

where their approach is extended to two dimensions. As Kernel K_h a two dimensional Gaussian distribution is used which is given as

$$K_{h_z h_\lambda}(z, \lambda) = \frac{1}{2\pi h_z h_\lambda} \exp\left(-\frac{1}{2} \left(\left(\frac{z}{h_z}\right)^2 + \left(\frac{\lambda}{h_\lambda}\right)^2 \right)\right), \quad (4.39)$$

where h_z and h_λ represent the standard deviations of the Gaussian distribution and are called bandwidths in this context. In this work, the bandwidths $h_z = h_\lambda = 1.0$ km are used which is about equal to the vertical resolution of CORAL's temperature measurements. The number of $(z, \lambda)_i$ -pairs is given by n .

In [Section 4.2.2](#) the 2D KDE is used to estimate the PDF of vertical wavelengths λ_i and altitudes z_i retrieved via WAVELET-SCAN.

4.2 Results

4.2.1 Identification of Stationary and Apparently Upward and Downward Propagating Waves in Austral Winter

The wave patterns in temperature data are analyzed by means of 2D wavelet analysis (Kaifler et al., 2015a, Chen and Chu, 2017, Kaifler et al., 2017) and GW-induced temperature perturbations are sorted into three wave classes depending on the angle of the phase lines in (t, z) -cross sections. The three wave classes comprise apparently upward propagating waves, stationary waves and apparently downward propagating waves. Dörnbrack et al. (2017) have shown that the relation of the background wind to the wave's group velocity plays a major role in how GWs appear in lidar data. For simplicity and lack of measured wind data, it is only distinguished between apparently upward and downward propagating waves and it is not accounted for potential Doppler shifts which can reverse the sign of the slope of phase lines in (t, z) -cross sections. Following the work by Zhao et al. (2017), a set of vertical phase speeds $c_{pz} = \pm[0.0, 0.4, 0.7, 1.0, 1.3] \text{ m s}^{-1}$ is defined to detect steady ($c_{pz} = 0$), apparently upward ($c_{pz} > 0$) and downward propagating ($c_{pz} < 0$) waves. Kaifler et al. (2017) used the criterion $c_{pz} < -0.35 \text{ m s}^{-1}$ for downward and $c_{pz} > 0.35 \text{ m s}^{-1}$ for upward propagating waves. The scales are chosen as suggested by Torrence and Compo (1998) such that, in case of MWs ($c_{pz} = 0$), vertical wavelengths from 2 km to 15 km are covered. Naturally λ_z increases for a phase line pattern with constant spacing when the orientation deviates from 90° , i.e. for upward and downward propagating waves. Hence, μ is truncated as function of ϑ in order to guarantee a maximum vertical wavelength of 15 km. One wavelet transformation is performed for each combination (μ, ϑ) . After that, temperature perturbations are reconstructed separately and averaged over orientations of associated wave classes. Finally, the RMS value of the temperature reconstructions of each wave class is computed over four altitude regions and the duration of the measurement. The altitude regions represent the lower (20 – 35 km) and upper (35 – 50 km) stratosphere as well as the lower (50 – 65 km) and upper (65 – 80 km) mesosphere.

As an example, results of this analysis applied to the measurement on 6 June 2018 are illustrated in Figure 4.5. In that particular case, sub-seasonal temperature perturbations show large vertical structures in the stratosphere which might be associated with PWs. A very pronounced oscillation that is stationary over the course of the measurement is found at about 60 km with a peak-to-peak amplitude exceeding 60 K. In the mesosphere, smaller scale perturbations become visible. The altitude range from 40 km to 70 km is dominated (>50%) by stationary phase lines while apparently upward and downward propagating waves contribute equally to the total RMS. Only above 70 km, apparently upward propagating waves dominate over downward propagating waves which could be a hint on the presence of secondary GWs (SGW).

The analysis is applied to each measurement lasting at least 6 h, i.e. the focus of this analysis is set on the winter season as measurements in summer are generally shorter. The total winter RMS is derived by integrating the RMS values over all measurements, the four altitude regions, and the three wave classes. The contribution of each wave class to the total winter RMS value is derived by integrating the individual RMS values over

all measurements as well as one altitude range and one wave class of interest, dividing the result by the total winter RMS. Table 4.1 lists the contributions to the total winter RMS of temperature reconstructions for each wave class in the four altitude regions. Stationary MWs account for slightly more than 50 % of sub-seasonal temperature perturbations at all altitudes. Their contribution increases up to the lower mesosphere. Apparently upward and downward propagating waves appear to have their maximum contributions in the upper and lower mesosphere, respectively. The findings of this analysis are comparable to the results in Kaifler et al. (2017).

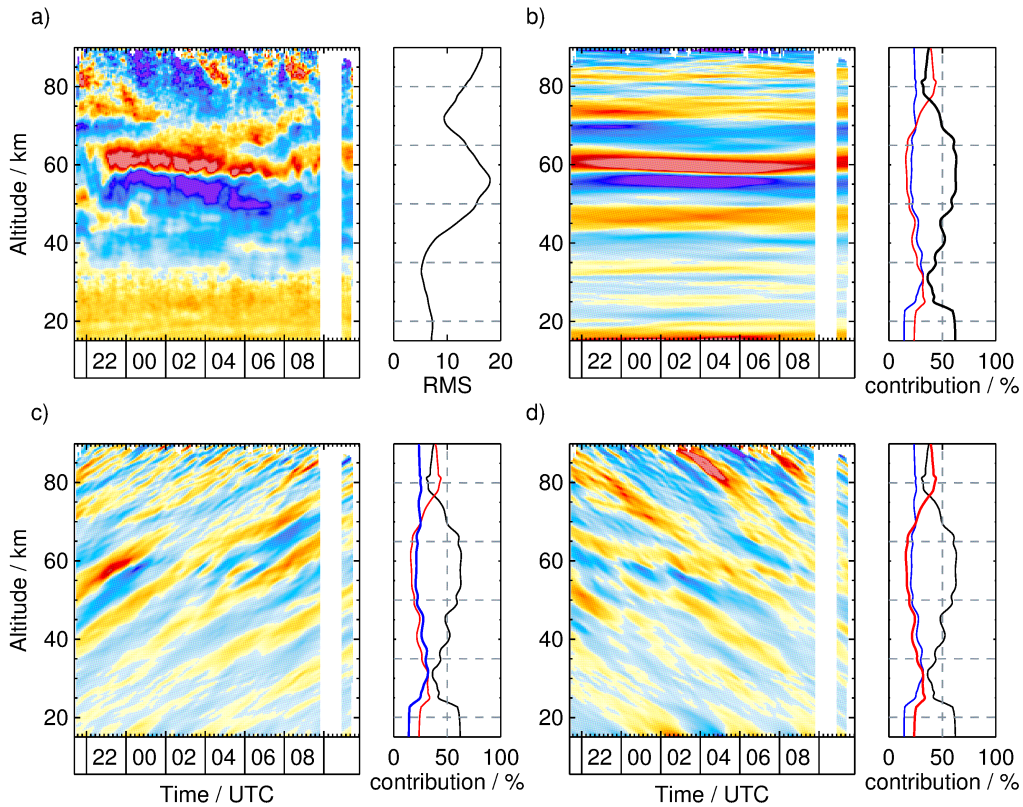


Figure 4.5: Depicted is an example for the analysis of wave class contributions. The sub-seasonal temperature perturbation \tilde{T} on 6 June 2018 is shown (a) together with the nightly RMS profile. In addition, steady (b) as well as apparently downward (c) and upward (d) propagating waves are shown. The nightly mean RMS contributions are associated with steady (black), apparently downward (blue), and upward (red) propagating waves.

4.2.2 Distribution of Vertical Wavelengths

The sub-seasonal temperature perturbations \tilde{T} contain signatures of PWs, tides and GWs. Usually, PWs exhibit significantly longer vertical wavelengths than GWs and, if detected, will primarily appear in the COI. Later, the discussion will be focused on the results outside the COI. To be less sensitive to tides a minimum spectral amplitude of 3K is

Altitude range	steady	upward propagating	downward propagating	total
65 – 80 km	16.0 %	9.7 %	6.0 %	31.7 %
50 – 65 km	17.2 %	8.4 %	6.7 %	32.3 %
35 – 50 km	12.9 %	5.4 %	5.0 %	23.3 %
20 – 35 km	7.3 %	2.7 %	2.7 %	12.7 %
total	53.4 %	26.2 %	20.4 %	100.0 %

Table 4.1: Listed are contributions of steady as well as apparently upward and downward propagating waves to the total winter RMS value of temperature reconstructions.

required, a value which describes typical amplitudes of diurnal tides in the stratosphere and lower mesosphere (see Fig. 3.11). WAVELET-SCAN is applied to winter measurements spanning more than 3 h and 60 km in time and altitude. The 2D KDE based on all detected wave packets is illustrated in Figure 4.6 with the hatched area indicating the COI.

Wave packets exist at all altitudes and with vertical wavelengths between 5 km and 30 km. The 2D KDE is probably underestimated at wavelengths smaller than 5 km due to the fact that waves in this spectral region exhibit smaller amplitudes. On the other hand, vertical wavelengths longer than 30 km might also occur very locally due to extremely strong horizontal wind speeds. The maximum of the 2D KDE is between 10 km and 16 km vertical wavelengths and in the altitude range 45 km – 80 km. By integrating the 2D KDE over altitudes and vertical wavelengths of interest, the probability to find waves within the chosen region can be obtained. 42 % of all detected wave packets have vertical wavelengths shorter or equal to 15 km. The probability increases to 50 % when the 2D KDE is integrated up to 16.5 km vertical wavelength. Wave packets exhibiting vertical wavelengths >20 km make up 35 % of the cases.

Winter time wind profiles in Figure 4.7 suggest that, according to $m = N/u$, maximum vertical wavelengths of hydrostatic MWs quickly increase towards the altitude of the wind maximum and shrink above. However, in the stratosphere this behaviour is not observed in the 2D KDE as the spatial resolution of the CWT is too low to resolve the rapid changes of m . A consequence of variable vertical wavelengths of GW packets is the potential for waves shifting in and out of the spectral window of the Butterworth filter, resulting in variable potential energies despite potentially constant amplitudes. An example is the extreme energy profile in May in Figure 4.9. On this night vertical wavelengths on the order of 20 km are found (not shown) in the mid-stratosphere, resulting in a substantial dip in retrieved potential energy at 40 km.

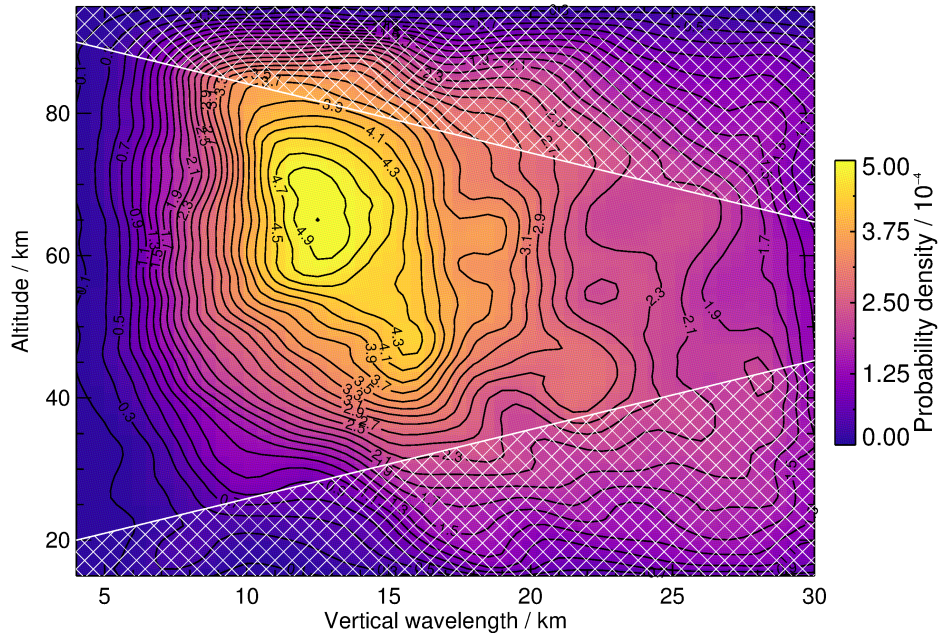


Figure 4.6: Depicted is the 2D KDE as function of vertical wavelength and altitude. The white hatched area marks the COI. Only data obtained between April and September of 2018, 2019 and 2020 are included.

4.2.3 Seasonal Variation of Gravity Wave Potential Energy

In the following the results of the analysis of GW potential energies is presented. Please note that the \diamond symbol represents a short-term arithmetic average, typically over the duration of a measurement night, while the \odot symbol represents a long-term geometric average over months or years. [Figure 4.8](#) shows $\langle E_p \rangle^\diamond$ averaged over a measurement night of at least 3 h duration for the following four altitude regions: 20 – 35 km (lower stratosphere), 35 – 50 km (upper stratosphere), 50 – 65 km (lower mesosphere), and 65 – 80 km (upper mesosphere). Averages, standard deviations, and skewnesses of lognormal E_p distributions for the four altitude regions are compiled in [Table 4.2](#). In addition, sample sizes and Gini coefficients are listed.

The $\langle E_p \rangle^\diamond$ time series presented in [Figure 4.8](#) show a pronounced annual variation at all altitudes with a minimum in austral summer and a maximum in winter. The largest difference between the summer and winter $\langle E_p \rangle^\odot$ is found in the lower mesosphere. Here, potential energies per mass are about ten times larger in winter than in summer ([Tab. 4.2](#)). In the upper mesosphere, a semiannual variation with a narrow peak in summer and a broad peak in winter can be identified. The minima of this semiannual variation coincide with the transition months March and October. A semiannual variation in zonal wind variances was also observed at Andenes and Juliusruh ([Hoffmann et al., 2010](#)). Striking are several high-energy events already exceeding 100 J kg^{-1} in the upper stratosphere. While this was only the case twice in 2019 and four times in 2020, in 2018 these events are found more frequently (e.g. [Kaifler et al., 2020b](#)). It is worth mentioning that November,

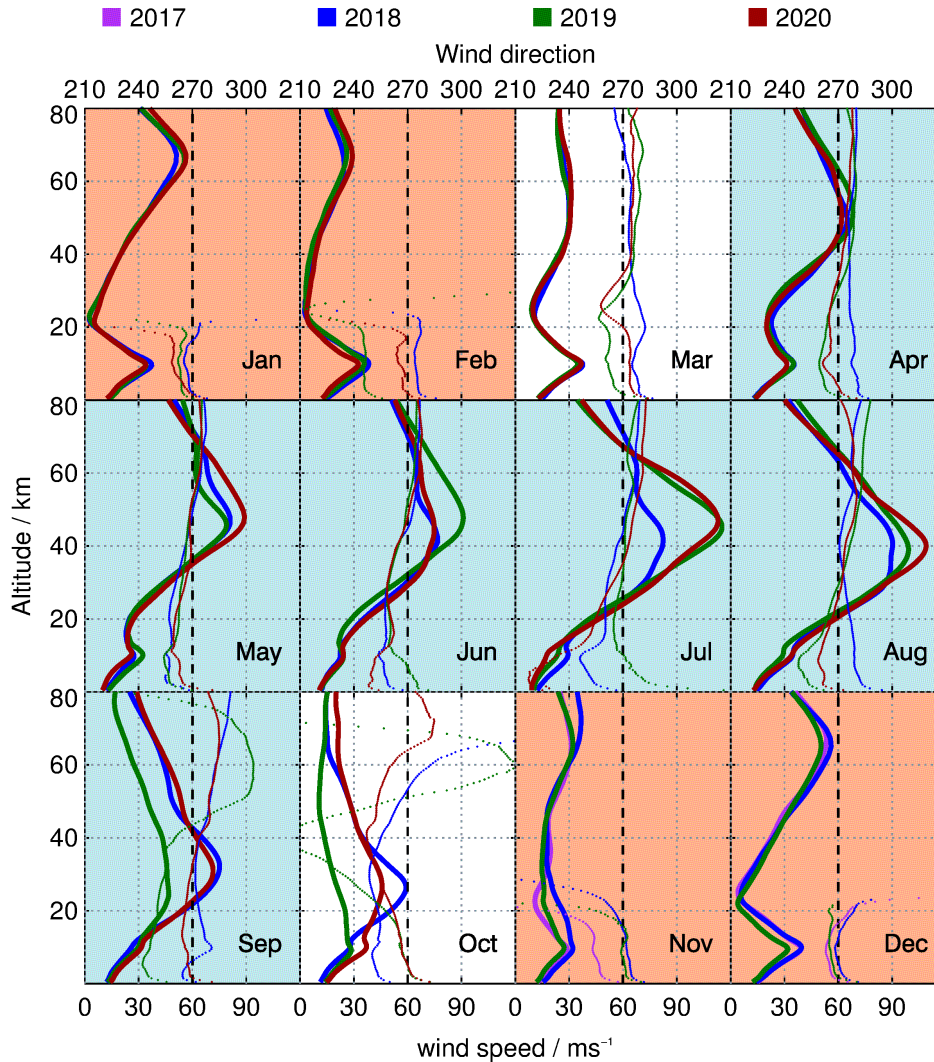


Figure 4.7: Illustrated are ERA5 monthly mean absolute wind profiles (thick lines, lower axis) and wind directions above Río Grande (thin lines, upper axis; the dashed lines mark westerlies). The wind field was truncated at T21 in order to filter out contributions from model-resolved GWs.

although classified as summer month, exhibits winter-like energies in the lower stratosphere. This results in relatively large values for σ^\oplus , γ^\oplus , and the Gini coefficient for the summer lower stratosphere (Tab. 4.2). In addition, histograms for summer and winter are shown to the right of each time series with thin horizontal lines indicating geometric averages. Drawn on a logarithmic axis, the histograms appear roughly as a normal distribution. This was already observed for GW potential energies (Baumgaertner and McDonald, 2007, Mzé et al., 2014, Kaifler et al., 2015b, Chu et al., 2018) and for GW momentum fluxes (Hertzog et al., 2012). In the lower and upper stratosphere, histograms

altitude	20 – 35 km	35 – 50 km	50 – 65 km	65 – 80 km
$\langle E_p \rangle^\circ$	2.8 J kg ⁻¹	2.8 J kg ⁻¹	5.8 J kg ⁻¹	31.4 J kg ⁻¹
	8.2 J kg ⁻¹	21.1 J kg ⁻¹	58.6 J kg ⁻¹	82.4 J kg ⁻¹
σ°	0.66	0.52	0.61	0.81
	0.88	0.96	0.75	0.58
γ°	0.19	0.01	0.06	0.00
	0.28	0.27	-0.02	0.02
I_g	0.33	0.23	0.22	0.25
	0.43	0.44	0.37	0.22
sample size	148 h	234 h	323 h	272 h
	1993 h	2247 h	2335 h	1941 h

Table 4.2: List of geometric mean summer (Nov – Feb) and winter (Apr – Sep; shaded) potential energies per mass $\langle E_p \rangle^\circ$ for four altitude levels. σ° represents the geometric standard deviation, γ° the skewness of the lognormal E_p distribution, and I_g the Gini coefficient.

exhibit tails towards larger E_p values in winter, reflecting enhanced GW intermittency.

4.2.4 Potential Energy as Function of Altitude

Next, monthly mean $\langle E_p \rangle^\circ$ profiles are investigated in which E_p values are under consideration that fall into the respective month (Fig. 4.9). Profiles are truncated in altitude if the number of data points at a given altitude is below 50% of the maximum number of data points.

Conservative growth curves are initialized with $E_0 = (1, 2, 5) \times (10^{-3}, 10^{-2}, 10^{-1}, 10^0)$ J kg⁻¹ (see Equ. 4.29) at 15 km altitude and shown together with derived $\langle E_p \rangle^\circ$ profiles in Figure 4.9. In analogy to Figure 2.5 one extreme energy profile is depicted for each month to highlight the extraordinary wave amplitudes and the resulting variability in $\langle E_p \rangle^\circ$ profiles. Please note that the selected extreme profiles in Figure 2.5 and Figure 4.9 do not necessarily refer to the same measurement nights because extreme temperature amplitudes may be damped in the E_p analysis if the λ_z associated with the temperature perturbations is larger than λ_{cut} .

In summer, $\langle E_p \rangle^\circ$ profiles do not differ substantially from month to month. Low energies as well as small standard deviations are observed from 20 km up to 60 km. Increased energies accompanied by larger standard deviations are only found in the lower stratosphere in November. Above 60 km, $\langle E_p \rangle^\circ$ increases rapidly and eventually reaches a maximum at ~ 80 km. In contrast to the stratosphere where observed energies are growing at a slower rate than the conservative growth rate, summer $\langle E_p \rangle^\circ$ profiles become closer aligned to the sketched conservative growth curves in the mesosphere. In summer, it can be noticed that generally conservative growth rates are smaller in the stratosphere than in the mesosphere. In March, initial energies in the lower stratosphere are comparable to summer months but exhibit larger standard deviations. In winter, all $\langle E_p \rangle^\circ$ profiles show significant growth up to ~ 60 km and level off above. Winter profiles are also characterized by large standard deviations that are comparable in the stratosphere and lower meso-

sphere, whereas standard deviations in the upper mesosphere are comparable to those in the summer months. Energies grow moderately from 20 km up to ~ 40 km in April and May and show a remarkable increase up to 60 km. Between 40 km and 60 km the $\langle E_p \rangle^\circ$ profile and the conservative growth curves are very much aligned in May. This zone with approximately conservative growth rates persists until September and extends further down covering the height range 30 – 50 km. In winter, the altitude range ~ 30 – 50 km shows noticeably smaller conservative growth rates than below and above. In October, $\langle E_p \rangle^\circ$ grows up to 40 km similar to winter months but reaches a local minimum at 55 km, only to grow above again. In the same time E_p geometric standard deviations are exceptionally large in the upper stratosphere.

The extreme energy profiles shown in [Figure 4.9](#) suggest that individual wave events can lead to E_p values that are five times larger than the monthly average in summer and up to 10 times larger in winter. The extreme energy profile in April is remarkable, with $E_p > 50 \text{ J kg}^{-1}$ over the entire altitude range and even $> 100 \text{ J kg}^{-1}$ from 30 km to over 80 km. In May and June GW potential energies do not always increase monotonically. The anomalous maximum potential energy at about 60 km demonstrates what happens when a large-amplitude wave with $\lambda_z > 15$ km is incorrectly assumed to be part of the background in the energy analysis. A very large wave-induced negative temperature gradient leads to a very low buoyancy frequency at that altitude, which results in E_p taking on very large values. In September, the extreme energy profile indicates growth rates larger than the conservative growth rate in the lower stratosphere.

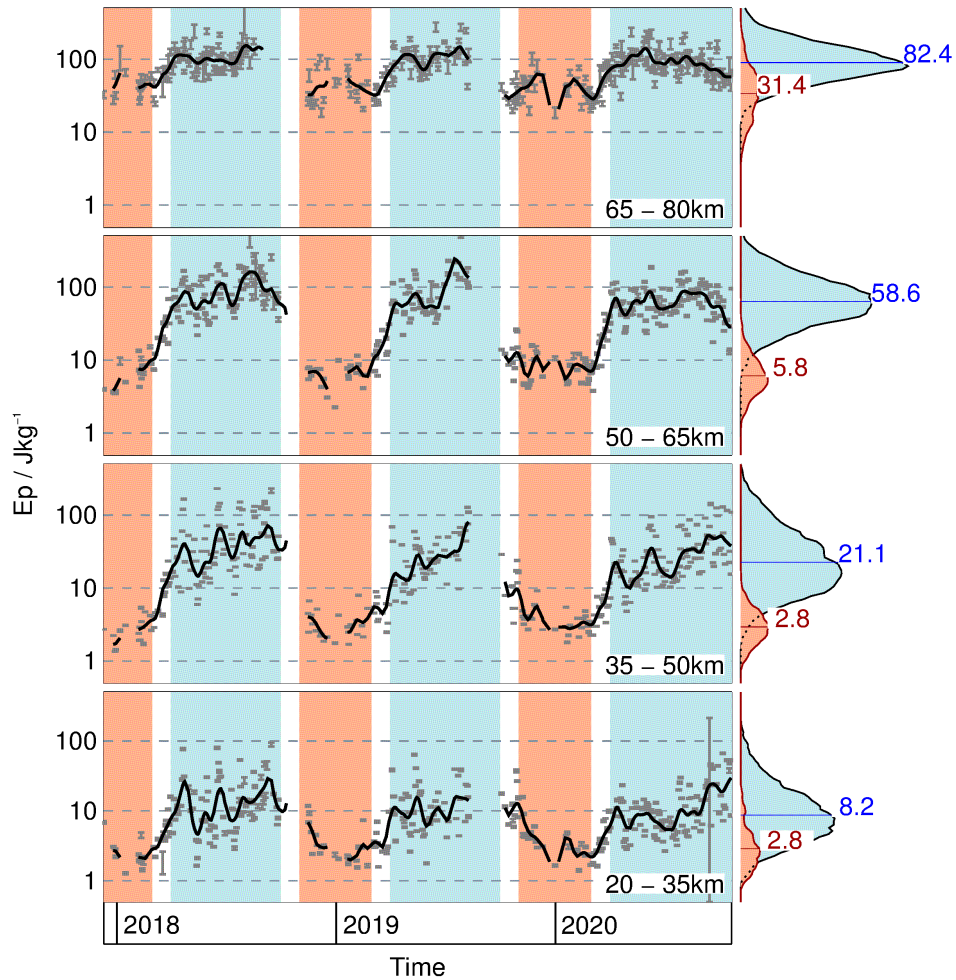


Figure 4.8: Time series of $\langle E_p \rangle^\diamond$ for four different altitude regions. The black line represents Hann smoothed $\langle E_p \rangle^\diamond$ with a window length of 30 days. The blue areas mark winter (Apr – Sep), red areas summer (Nov – Feb) and white areas transition months (Mar and Oct). Histograms represent wintertime (blue) and summertime (red) E_p distributions. The horizontal blue and red lines mark the geometric averages of the distributions. Please note the logarithmic y-axis which is also valid for the histograms. See text for details.

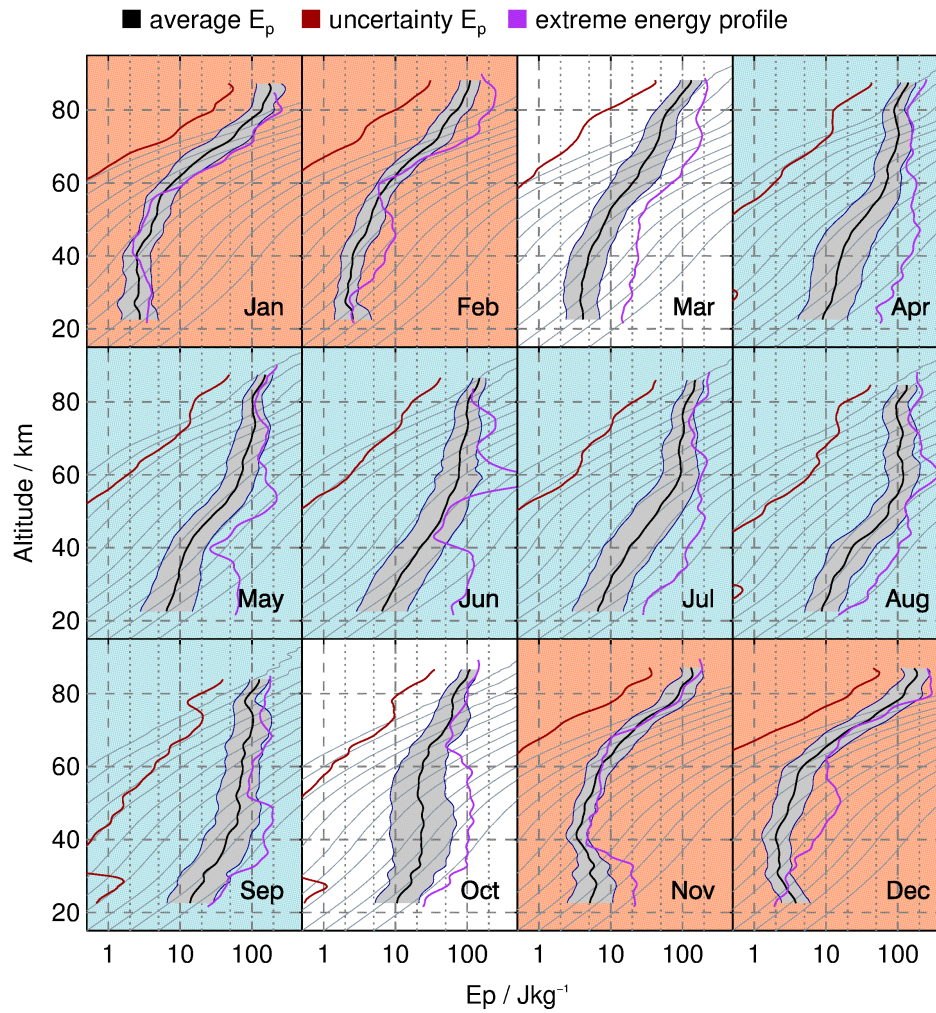


Figure 4.9: Illustrated are monthly mean $\langle E_p \rangle^\circledast$ profiles (black solid), extreme energy profiles (purple solid) and monthly mean E_p uncertainty profiles (red solid). The shaded area indicates the geometric standard deviation of E_p values and the grey hairlines mark conservative growth curves $\sim \exp(z/H_s(z))$. Dashed lines mark the following intervals: 2, 5, 20, 50 and 200 J kg⁻¹. See text for details.

4.3 Discussion

4.3.1 Distribution of Vertical Wavelengths

Most lidar studies dealing with GWs have focused on temperature perturbations with vertical scales $\leq 15 - 20$ km. In contrast to that, many satellite studies show GWs with larger vertical wavelengths (e.g. Preusse et al., 2002). In this work vertical wavelengths are investigated based on the sub-seasonal temperature perturbations which were only detrended by subtracting the annual and semiannual oscillations. Therefore, WAVELET-SCAN results show a broad distribution of vertical wavelengths with values between 5 km and 30 km. The presence of waves with vertical wavelengths in the range 20 – 30 km confirms previous satellite observations. In fact, the majority of detected GWs (58% of the waves) exhibits vertical wavelengths longer than 15 km (Fig. 4.6).

This finding has important implications for the interpretation of previous ground-based analysis: If a dominant wave with $\lambda_z > \lambda_{\text{cut}}$ occurs, its potential energy is underestimated. This affects the E_p distribution such that $\langle E_p \rangle^\circ$ is underestimated and might even result in an underestimation of σ° , γ° , and I_g , as waves of larger scales can exhibit larger amplitudes before they become convectively unstable. The transition from $\lambda_z < \lambda_{\text{cut}}$ to $\lambda_z > \lambda_{\text{cut}}$ and vice versa occurs most often at the location of the local horizontal wind maximum, i.e. at 40 km to 50 km. In addition, the latitudinal position of the PNJ over the Southern Andes can change significantly over the course of several weeks. As the PNJ is responsible for the refraction of waves towards larger vertical wavelengths, this mechanism in combination with a fixed λ_{cut} might also affect the derivation of GW potential energies.

4.3.2 Gravity Wave Activity in the Stratosphere

For upward MW propagation, the wind speed in the direction of wave propagation must not become zero as this would lead to wave breaking (Lindzen, 1981). The filtering of MWs in the summer lower stratosphere is mostly responsible for the observed seasonal modulation of GW potential energy in the stratosphere (Fig. 4.8). The presence of a stratospheric wind minimum between March and May is likely the reason why energies increase only moderately in this transition period. When the u' -amplitude of a wave approaches the background wind speed, for instance at this stratospheric wind minimum, self-induced instability occurs and leads to the deposition of momentum and a decrease or stagnation of wave amplitudes. This stratospheric wind minimum is referred to as *valve layer* as it acts as a valve regulating the vertical transport of GW momentum (Kruse et al., 2016). When the polar vortex starts to break down, the mesospheric wind reversal shifts from 80 km in October down to ~ 30 km in November. The resulting variability is likely the reason for large E_p standard deviations in the stratosphere in October. The downward shift of the breaking level causes also an earlier decrease of energies at higher altitudes (Kaifler et al., 2015b). This is well perceived by the end of winter 2018 in Figure 3.2b. An exception occurred in September and October of 2019 when a SSW occurred and forced the circulation to reverse about one month earlier than usual (e.g. Dörnbrack et al., 2020, Rapp et al., 2021, Yamazaki et al., 2020).

An annual variation of E_p was also observed above Rothera (67°S, 68°W) (Yamashita et al., 2009). In contrast to CORAL's location with respect to the main mountain ridge,

the study at Rothera was conducted on the upstream side of the mountains of the Antarctic Peninsula. Qualitatively, the annual cycle of stratospheric E_p above Rothera is the same as above Río Grande with a maximum in winter and the minimum in summer. Although E_p values cannot be compared one-to-one because the spectra of the GWs contributing to the calculated E_p differ and averaging is different, it is still argued that the GW activity above Río Grande is considerably larger than above Rothera. This is consistent with the assumption that MWs primarily propagate above and downstream of the mountains. Hence, smaller E_p values are expected upstream.

Wintertime E_p histograms in the lower and upper stratosphere (Fig. 4.8) exhibit tails towards large values which are indicative of enhanced GW intermittency. The standard deviation and skewness of the E_p lognormal distribution and the Gini coefficient have their maximum in the winter stratosphere, suggesting that GW intermittency is largest there. Enhanced GW intermittency in the winter stratosphere points to the occurrence of few high-energy events that contribute a large portion of the total potential energy which is in line with Kaifler et al. (2020b). In the summer lower stratosphere σ° , γ° , and I_g are smaller than in the winter lower stratosphere but still larger than in the summer upper stratosphere. This is most likely due to considerable wave events detected in the lower stratosphere in November when the MW breaking level is still at about 30 km.

E_p profiles are compared with those from previous studies in Figure 4.10a. In the case of the study by Chu et al. (2018), a mean profile is computed over the months of May to September. In addition, all E_p profiles are Hann smoothed with a window length of 10 km. Please note that the profile from Wright et al. (2016) is based on SABER measurements in the spatial domain $49^\circ - 59^\circ$ S and $58^\circ - 78^\circ$ W, while the other profiles are based on lidar data at fixed locations.

The $\langle E_p \rangle^\circ$ profile from Río Grande and the study by Wright et al. (2016) are very similar. While Wright et al. (2016) detect waves with $4 \text{ km} < \lambda_z < 30 \text{ km}$ (see Fig. 4.10b), they are only sensitive to waves with $\lambda_h > 500 \text{ km}$. In this work, on the other hand, waves with $2 \text{ km} < \lambda_z < 15 \text{ km}$ are detected regardless of their horizontal wavelength. Almost congruent profiles are probably a coincidence and may result from differences in spectral sensitivity. About two times larger energies are found in the stratosphere and lower mesosphere above Río Grande in comparison to Davis station (Alexander et al., 2011, Kaifler et al., 2015b). The spectral coverage in the studies by Alexander et al. (2011) and Kaifler et al. (2015b) is shifted towards longer vertical wavelengths in comparison to CORAL's data, which might contribute to the observed factor of 2 difference. There is a factor of 5 difference between energies from Chu et al. (2018) and this work that is probably due to the fact that Chu et al. (2018) consider only GWs with ground-based periods between 3 h and 9 h. The study by Mzé et al. (2014) includes GWs at the high-frequency end of the spectrum with vertical wavelengths between 1 km and 10 km and ground-based periods $> 1 \text{ h}$. The deviations are largest in the stratosphere where energies are about 5 times larger at Río Grande than at Haute Provence, but at 80 km the profiles are almost identical. This decreasing difference in GW potential energy might be explained by different GW source spectra at the two locations. In addition to varying spectral coverages, it is argued that the large energies in this work compared to other studies are the result of larger wave amplitudes at Río Grande due to stronger MW forcing and favourable propagation conditions.

As is evident from [Figure 2.4](#), the winter stratosphere over Río Grande is an extremely perturbed place. Both the thermal and the wind structure provide ideal growth conditions for MWs. The growth rates are the largest ever reported in the climatological mean. Individual cases (see e.g. extreme energy profile in April in [Figure 4.9](#)) already show potential energies exceeding 100 Jkg^{-1} at 30 km, an E_p value that is considered to be the saturation limit in the mesosphere (see [Section 4.3.3](#)). These extraordinary cases have a large impact on the E_p distribution and hence are responsible for enhanced GW intermittency ($I_g = 0.46$). It is likely that strong MW forcing and the relatively stable connection of the PNJ to the tropospheric jet (e.g. [Vaugh et al., 2017](#)) lead to the observed extreme wave amplitudes that make this region the world's largest stratospheric GW hotspot.

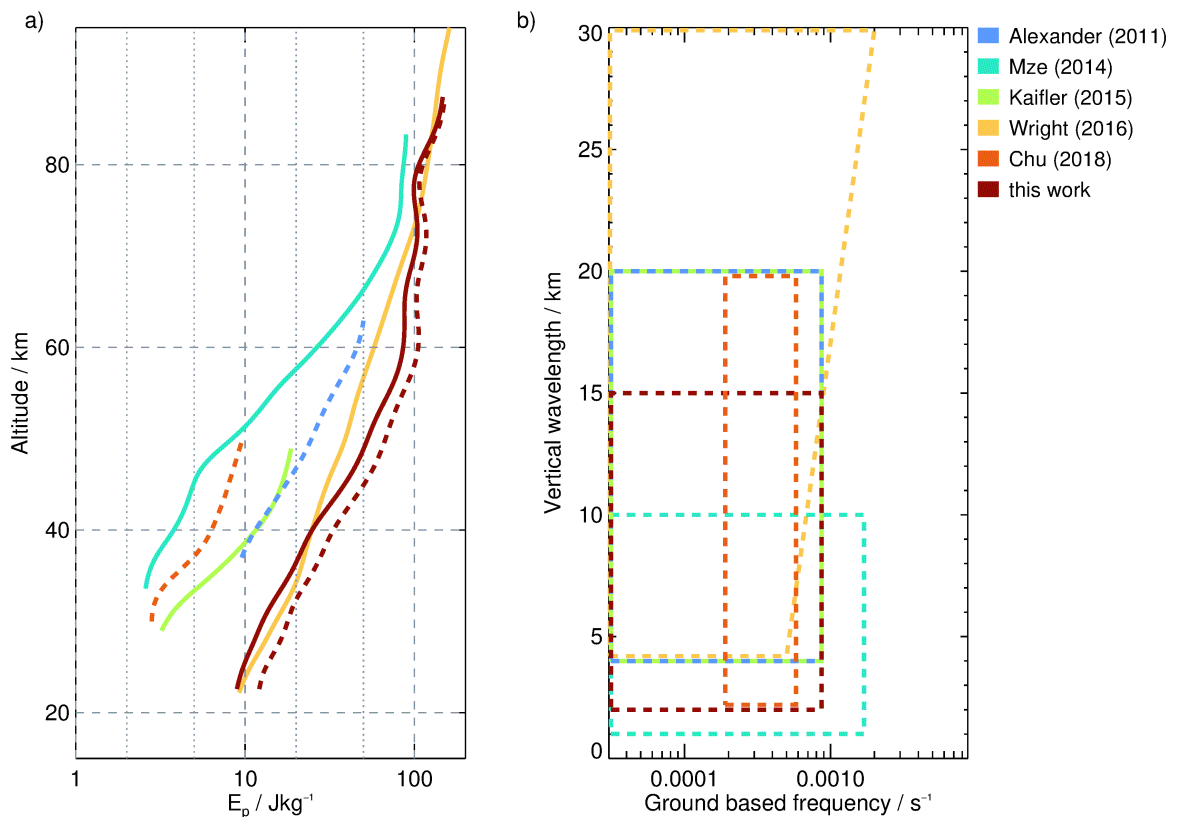


Figure 4.10: Shown are winter median/geometric mean (solid) and arithmetic mean (dashed) E_p profiles from different publications (a) and respective spectral ranges (b).

4.3.3 Gravity Wave Activity in the Mesosphere

In addition to the stratosphere, annual variations in wave activity are also observed in the mesosphere with a semiannual variation superimposed. The summer peak of $\langle E_p \rangle^\diamond$ in the upper mesosphere is best explained by non-orographic GWs, as orographic waves are filtered in the lower stratosphere. Their sources may include convection in the troposphere ([Taylor and Hapgood, 1988](#), [Sato, 1993](#), [Alexander and Pfister, 1995](#), [Dewan et al., 1998](#)), shear instabilities in the jet exit region ([Bühler et al., 1999](#), [Bühler and McIntyre, 1999](#)),

and geostrophic adjustment (e.g. [Fritts and Luo, 1992](#)). A close alignment of the $\langle E_p \rangle^\diamond$ profile with conservative growth curves in January and December indicates a conservative propagation of waves in the summer mesosphere. The $\langle E_p \rangle^\diamond$ minima in the transition months are probably due to small wind speeds close to zero over a wide range of heights which can lead to self-induced shear instabilities by GWs ([Wilson et al., 1991](#)). A semi-annual pattern of wave activity is also reported by [Krebsbach and Preusse \(2007\)](#) based on SABER measurements. Most recently [Sedlak et al. \(2020\)](#) found that the semiannual variation of wave activity at ~ 85 km is primarily due to short period GWs (1.0 – 3.5 h) whereas the annual variation is due to long period GWs (3.5 – 8.0 h). The 2D wavelet analysis reveals that the winter peak of $\langle E_p \rangle^\diamond$ in CORAL data is mainly due to MWs, but an increasing number of apparently upward and downward propagating waves also contributes to enhanced GW potential energies ([Tab. 4.1](#)).

The constant $\langle E_p \rangle^\circledast$ profiles above 60 km in winter (see [Fig. 4.9](#)) suggest that wave amplitudes cannot grow any further and the GW spectrum is saturated. This is in line with wintertime observations of turbulence covering the entire mesosphere (60 km – 100 km) above the Andøya Rocket Range in northern Norway ([Lübken, 1997](#)). To examine the observed saturation in more detail, the power spectral density (PSD) is determined in the stratosphere (20 – 50 km) and mesosphere (50 – 80 km) for summer and winter separately ([Figure 4.11](#)). The PSD is calculated as $F(m) = \frac{\delta z^2}{\Delta z} |\hat{x}(m)|^2$ where $\delta z = 0.1$ km, $\Delta z = 30$ km, and $\hat{x}(m)$ is the FFT of the relative sub-seasonal temperature perturbations $\frac{T'}{T_0}$ scaled with g/N^2 ([Smith et al., 1987](#), [Wilson et al., 1991](#), [Alexander et al., 2011](#)). In addition, the saturation limit $\frac{N^2}{10m^3}$ is calculated following [Fritts and Alexander \(2003\)](#) and [Alexander et al. \(2011\)](#). For this, monthly mean temperature profiles from [Figure 2.5](#) are averaged over summer and winter, respectively, and N is computed according to [\(1.1\)](#). In a second step, N is averaged over stratospheric and mesospheric altitudes.

In the summer stratosphere, there is an order of magnitude difference between the average PSD and the saturation limit for short vertical scales around 2 km. The difference increases gradually to two orders of magnitude at vertical scales of 20 km. In winter the behaviour is qualitatively the same but the differences are smaller by a factor of two, which is due to stronger stratospheric wave activity. [Wilson et al. \(1991\)](#) observed the same difference in PSD in the summer stratosphere (30 – 45 km) but also found a similarly low PSD in winter above Haute Provence. At Río Grande, in the summer mesosphere the mean PSD is rather close to the saturation limit for small vertical scales. The saturation limit is actually within the 1σ range at scales ranging from 1.8 km to 5 km, but for large scales a difference of one order of magnitude remains. In winter, however, the mean PSD is very close to the saturation limit and is within the 1σ range at all scales between 1.8 km and 20 km. [Wilson et al. \(1991\)](#) observed saturation for scales up to 8 km in the altitude range 60 – 75 km in winter. [Alexander et al. \(2011\)](#) showed that only small scales (4 km) reach the saturation limit in the winter mesosphere (49 – 59 km) above Davis Station. In contrast, [Figure 4.11](#) reveals that the GW spectrum at Río Grande is saturated for all vertical wavelengths of up to 20 km. This is an outstanding result as no other study has yet shown saturation up to these large scales. It is concluded that the strongly saturated GW spectrum is a combination of both strong forcing and favourable vertical propagation at the GW hotspot in the Southern Andes region.

E_p standard deviations, skewnesses, and Gini coefficients for the winter mesosphere in-

indicate a decreasing GW intermittency from 50 km to 80 km (Tab. 4.2). In contrast, increasing σ° and I_g suggest an increasing GW intermittency in summer from 50 km to 80 km. Hence, it is concluded that saturation of the GW spectrum influences the GW intermittency in the mesosphere. In a saturated spectrum, GW amplitudes cannot grow anymore with altitude, as larger amplitudes cause self-induced instabilities and thus can exist for short periods of time only. If, in the stratosphere, GW amplitudes are modulated in time due to the intermittency of GWs, this means that for large-amplitude waves, saturation of the GW spectrum occurs already at lower altitudes than would be the case for low-amplitude waves. However, the amplitudes in the altitude region where the spectrum is saturated remain at approximately the same level. Hence, it is expected that the temporal variability of E_p in the saturation zone is strongly reduced in comparison to the variability at lower altitudes. This behavior is clearly visible in the data which suggests a saturation limit of $\sim 100 \text{ J kg}^{-1}$. The E_p profile by Mz e et al. (2014) indicates a saturation limit of $\sim 90 \text{ J kg}^{-1}$ above 75 km (Figure 4.10a), but a saturation zone starting at 60 km was not yet observed. The SABER winter median E_p profile from Wright et al. (2016) shows further increasing values towards 100 km altitude, but differences between the SABER profile and CORAL data are probably due to different observational filters (Alexander, 1998).

The winter mesosphere above R o Grande is characterized by GW dissipation. This becomes evident, for instance, from the extreme wave profiles in Figure 2.5 which show unstable temperature gradients. However, constant GW potential energies above 60 km and the PSDs shown in Figure 4.11 indicate a saturated GW spectrum up to scales of 20 km, resulting in the deposition of wave momentum and energy at these altitudes. A fraction of this momentum is likely used to generate SGWs (Vadas et al., 2018). This conclusion is supported by the increasing portion of apparently upward and downward propagating waves (Tab. 4.1).

4.3.4 Comparison of Wave Energies based on different Cutoffs

Separating GW-induced temperature perturbations from the background is a crucial step in the determination of GW potential energies (Equ. 4.19). Ehard et al. (2015) compared a number of separation methods and concluded that a 5th order Butterworth high-pass filter (Sec. 3.1.2) applied to temperature profiles would best filter MW signals. This filter is applied with a cutoff wavelength of 15 km as described in Section 3.1.2. This cutoff might be appropriate in the northern hemisphere where typical vertical wavelengths of GWs are significantly shorter than in the southern hemisphere (Yan et al., 2010, Ern et al., 2011). However, Figure 1.2 and the extreme wave profiles in Figure 2.5 show vertical wavelengths in the range of 15 – 20 km, a finding that confirms previous satellite measurements in the Southern Andes region and casts doubt on the appropriateness of the choice of $\lambda_{\text{cut}} = 15 \text{ km}$ in the GW analysis. The analysis of vertical wavelengths (Sec. 4.2.2) also reveals that 50 % of detected waves exhibit vertical wavelengths longer than 16.5 km. It becomes evident that the wave energies presented in Section 4.2.3 and Section 4.2.4 are underestimated.

Yet, realistic wave energies cannot be retrieved by simply increasing the cutoff wavelength. The temperature structure of the stratopause and mesopause contains instantaneous high-

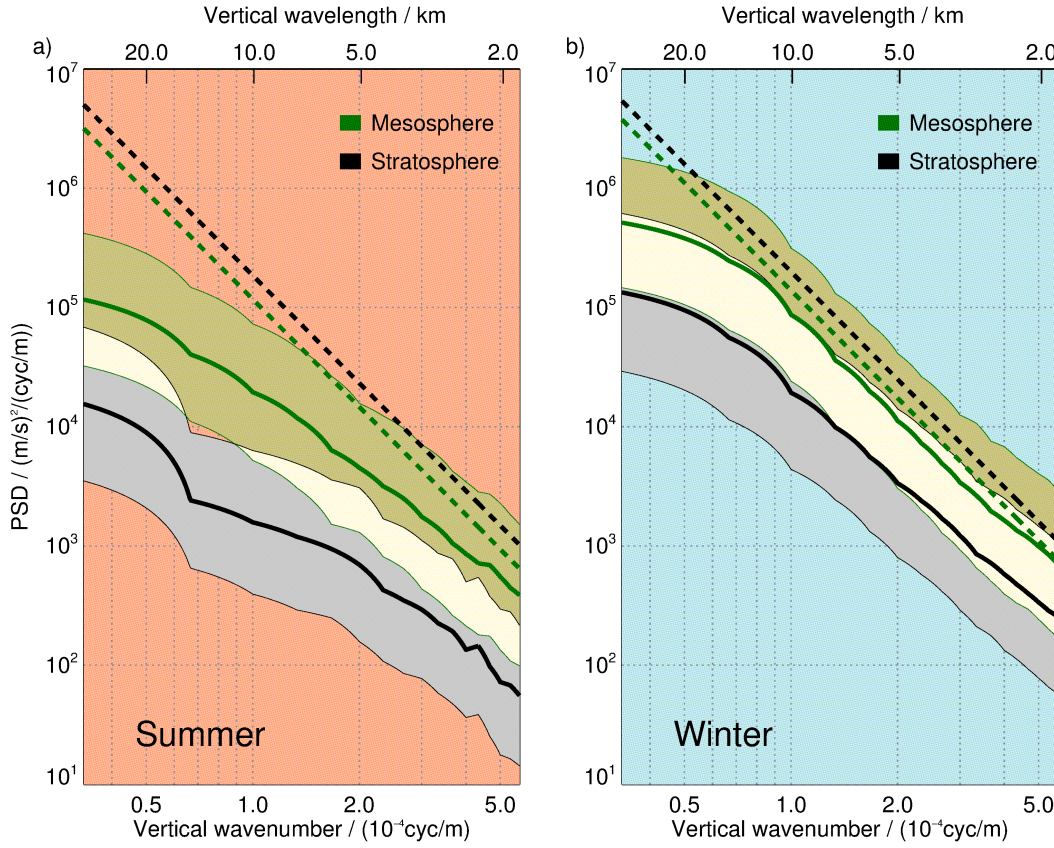


Figure 4.11: Depicted are average power spectral densities in the stratosphere (black) and the mesosphere (green) for summer (a) and winter (b). Saturation limits (dashed lines) are computed according to $\frac{N^2}{10m^3}$. Shaded areas in the background indicate standard deviations.

frequency components that might result in a spectral leakage of variance into retrieved temperature perturbations. The same holds true for PWs and tides (see also Fig. 3.1). Therefore, and only because CORAL’s high cadence of measurements allows for it, the DT-R2D fit presented in Section 3.1.2 was developed that allows for a more realistic determination of the temperature background and thus estimation of more realistic GW signals. Figure 4.12 illustrates the difference between λ_{15km} - and realistic-wave amplitudes. It shows two consecutive measurements during two nights in late May 2018, which include the temperature profile shown in Figure 1.2. In Figure 4.12a the Butterworth filter with $\lambda_{cut} = 15$ km is applied in the vertical resulting in a nightly mean maximum amplitude of 8.9 K. In Figure 4.12b the temperature background as defined in Chapter 3 is subtracted, which results in a nightly mean maximum amplitude of 17.8 K. Preusse et al. (2008) state

$$T_{\max} = \frac{\bar{T}N^2}{mg} \quad (4.40)$$

which is the temperature amplitude saturation limit that a wave can reach before it becomes convectively unstable. With a background temperature of about 260 K, a strato-

spheric $N = 0.02 \text{ s}^{-1}$, and a vertical wavelength of $\sim 20 \text{ km}$, a saturation amplitude of $T_{\text{max}} = 33.7 \text{ K}$ is computed. The maximum amplitude of realistic temperature perturbations at 04 UTC on 31 May 2018 is 32.2 K (see Fig. 4.12b) which indicates that the detected MW has reached its saturation amplitude and breaks.

In this example (Fig. 4.12), $\lambda_{15\text{km}}$ - and realistic-wave amplitudes differ by a factor of ~ 2 and thus by a factor of ~ 4 in wave energies. On the other hand, structures in Figure 4.12b above $\sim 80 \text{ km}$ are very likely due to SDTs and therefore lead to an overestimation of wave energies there.

In Figure 4.13 profiles of GW potential energy are presented for summer and winter where three different scale separation schemes are used. The first profile represents the $\lambda_{15\text{km}}$ -case as the scale separation is achieved via the application of the Butterworth high-pass filter with a cutoff wavelength of 15 km . In a similar way, the second profile includes vertical scales up to 30 km and is referred to as the $\lambda_{30\text{km}}$ -case. The third profile, called realistic-case, is based on the scale separation via the determined temperature background and the additional application of a Butterworth high-pass filter with a cutoff at 30 km . The high-pass filtering is necessary to exclude any scales larger than 30 km that might remain from the subtraction of the determined temperature background and to make it comparable to the $\lambda_{30\text{km}}$ -case. The $\lambda_{15\text{km}}$ winter profile of E_p is identical to the one shown in Figure 4.10a. While there is a factor of 5 between the $\lambda_{15\text{km}}$ - and the $\lambda_{30\text{km}}$ -profiles in the lower stratosphere, there is only a factor of 2.5 left in the mesosphere. This suggests that in winter vertical scales between 15 km and 30 km are more prominent in the stratosphere than in the mesosphere. This is to be expected due to the large horizontal wind speeds at the altitude of the PNJ ($\sim 45 \text{ km}$). The realistic E_p profile shows twice as much energy at all altitudes in comparison to the $\lambda_{15\text{km}}$ -profile. This is an important result because it means that statements about e.g. wave dissipation or the saturation limit, which are based on the $\lambda_{15\text{km}}$ -profile, still hold. The doubling of energy is presumably due to the fact that GWs with vertical wavelengths larger than 15 km are now considered. However, please note that above 50 km a small fraction of the energy is likely due to SDTs that were not fully extracted by the DT-R2D fit. The large difference (factor of 2.5) between the realistic E_p profile and the $\lambda_{30\text{km}}$ -profile in the stratosphere indicates that the DT-R2D fit successfully identifies background features with vertical scales larger than 15 km . In the mesosphere, the difference between the two profiles decreases to a factor of 0.25 which might be due to the fact that fewer large-scale features are present or that the DT-R2D fit fails to capture large-scale features at these altitudes (e.g. SDTs).

In summer, E_p is dominated by vertical scales between 15 km and 30 km or even larger scales at all altitudes. The $\lambda_{15\text{km}}$ -profile is at about $1/3$ of the $\lambda_{30\text{km}}$ -profile in the lower stratosphere, and its contribution decreases to $1/5$ at 70 km . The realistic energy profile shows again about twice as much energy as the $\lambda_{15\text{km}}$ -profile. However, because the summer measurement cadence is too low the realistic energy profile contains contributions from DTs that were not properly captured by the DT-R2D fit. Therefore, true wave energies are probably below the realistic energy profile.

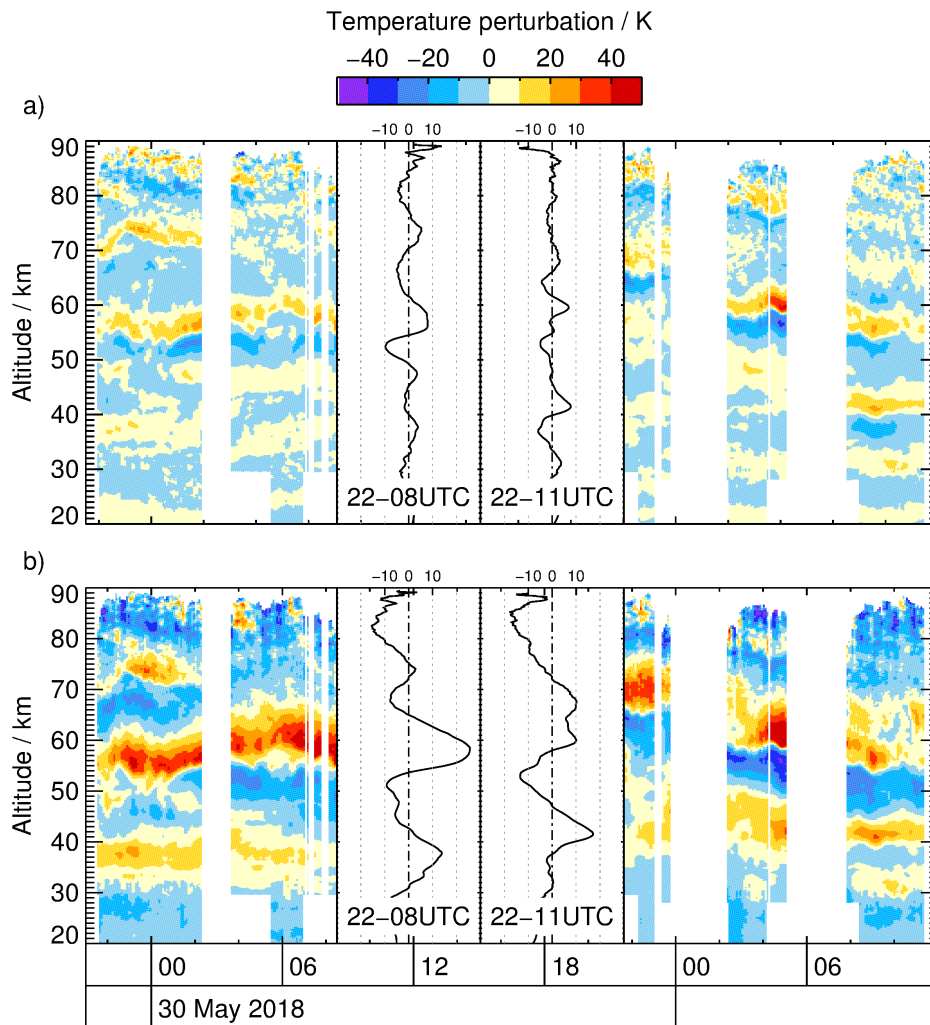


Figure 4.12: (t, z) -cross sections of temperature perturbations are illustrated for two consecutive nights in late May 2018 retrieved from the application of a 5th order Butterworth filter with $\lambda_{\text{cut}} = 15$ km (a) and retrieved via the subtraction of the temperature background as defined in [Chapter 3](#) (b). Between (t, z) -cross sections nightly mean perturbation profiles are shown.

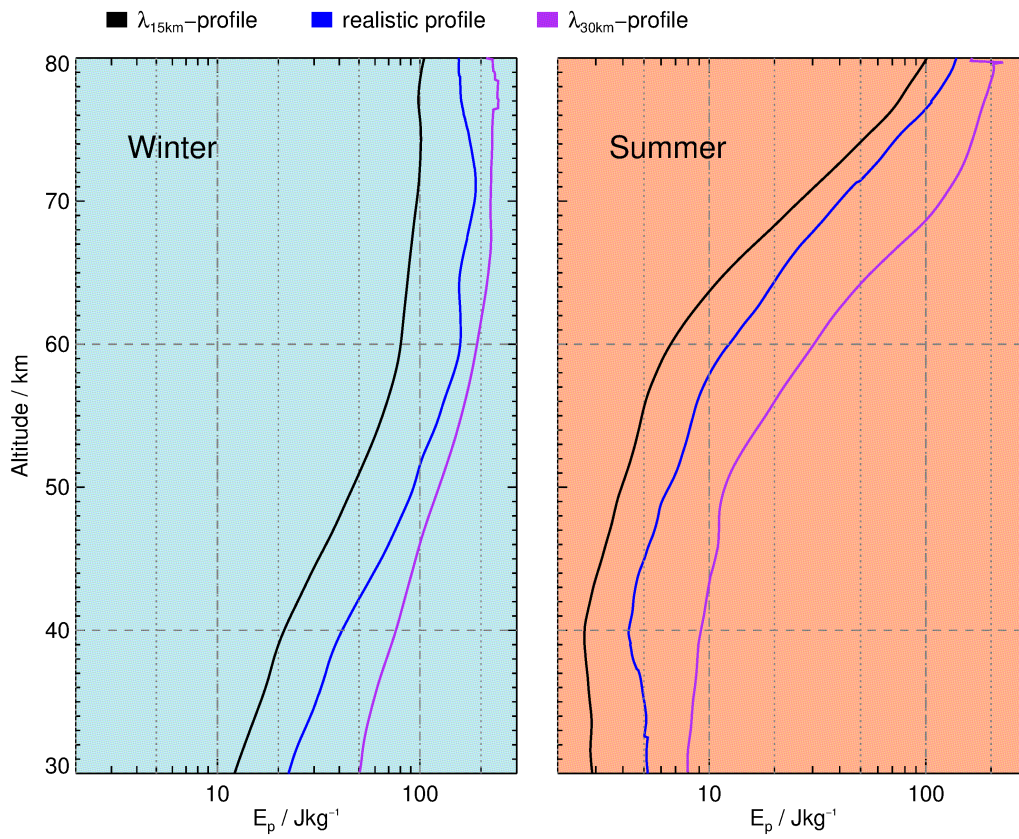


Figure 4.13: Seasonal mean E_p profiles are shown for $\lambda_{\text{cut}} = 15$ km (black), $\lambda_{\text{cut}} = 30$ km (purple) and for realistic GW signatures (blue).

4.4 Summary and Answer to Research Question (R2)

The CORAL lidar system has been deployed in close vicinity of the strongest stratospheric GW hotspot in the world. The research question was posed:

(R2) What is the signature of the world’s strongest stratospheric gravity wave hotspot in high-cadence CORAL temperature data?

Fraction of MWs

Steady phase lines lasting 3 – 15 h dominate (53.4%) the observed temperature perturbations at all altitudes (see [Tab. 4.1](#) or exemplary [Fig. 4.5](#)), indicating that orographic forcing is the predominant source of GWs detected by CORAL in the lee of the Andes. As higher mountain peaks are distant, the hypothesis was formulated that the observed MWs belong to the hydrostatic rotating wave regime as defined by [Queney \(1948\)](#) and [Gill \(1982\)](#) (see [Fig. 1.4](#)). If this were indeed the case, air flow across the entire southern Andean ridge can be considered as the waves’ source of excitation. Similar observations of the leeward and downstream propagation of MWs with large horizontal wavelengths ($\lambda_h > 100$ km) have been made in the northern hemisphere ([Dörnbrack et al., 1999](#), [Kivi et al., 2020](#)), and published comparisons with ECMWF model results ([Kaifler et al., 2020b](#), [Gupta et al., 2021](#), [Rapp et al., 2021](#)) support these observational findings. In addition to steady phase lines, the increasing contribution of apparently upward and downward propagating waves with altitude might be an indication of SGWs at mesospheric altitudes ([Vadas et al., 2018](#)) or convectively generated GWs from tropical regions ([Yue et al., 2014](#), [Yuan et al., 2016](#)), to name possible interpretations.

Seasonal variability of GW potential energy

The GW potential energies over Río Grande show a seasonal variability (see [Fig. 4.8](#)) as seen in other studies ([Yamashita et al., 2009](#), [Kaifler et al., 2015b](#), [Baumgarten et al., 2017](#), [Chu et al., 2018](#), [Llamedo et al., 2019](#)). The seasonal variation of the GW potential energy is most noticeable in the lower mesosphere. At this altitude, E_p up to 10 times larger are measured in winter than in summer (see [Tab. 4.2](#)). In addition, the measurements also show a semi-annual variation of the GW potential energy in the upper mesosphere as also observed by [Mzé et al. \(2014\)](#) and [Sedlak et al. \(2020\)](#).

Conservative wave propagation

GW potential energies in the winter stratosphere are the largest ever reported which is most likely due to strong excitation resulting in very large initial wave amplitudes and favorable propagation conditions. In the winter stratosphere, GWs propagate conservatively in the climatological mean (see [Fig. 4.9](#)), i.e. their vertical and downstream propagation can be approximately described by linear theory. This is in agreement with previous findings ([Alexander et al., 2011](#), [Kaifler et al., 2015b](#), [Mzé et al., 2014](#), [Wright et al., 2016](#)). In individual cases, the stratospheric increase of E_p seems to exceed conservative growth

rates, a potential indication of lateral propagation of waves through CORAL's field of view. Above 60 km altitude, the identification of an E_p saturation limit on the order of $\sim 100 \text{ J kg}^{-1}$ suggests major wave dissipation and saturation in winter. A saturated GW spectrum is also evident from the PSD (see Fig. 4.11). A saturation limit of the same magnitude was also found in Haute Provence but only for altitudes above about 75 km (Mzé et al., 2014). In individual cases, the occurrence of constant profiles of GW potential energy close to the saturation limit is indicative of wave dissipation in the entire observational volume. A likely and very plausible explanation is the breaking of MWs excited by an exceptional strong forcing and excellent propagation conditions.

GW intermittency

GW intermittency above Río Grande is largest in the winter stratosphere and decreases with altitude (see Tab. 4.2). The decrease is likely related to the saturation of the GW spectrum in the winter mesosphere. This finding is in contrast to the results by Wright et al. (2013), who found almost constant intermittency between 25 km and 65 km based on SABER data. Different results with regard to GW intermittency are probably due to different observational filters. Every winter month, there is at least one temperature profile with exceptionally large stratospheric temperature deviations from the monthly mean by 25 K to 55 K (see Fig. 2.5). Even if these amplitudes are not caused by GWs alone but presumably by superposition with PWs, they are the largest perturbations ever measured. First, these large values are indicative of the exceptional wave energies that can be achieved over the Andes. Second, their presence in the CORAL data set underscores the advantage of high-resolution and high-cadence ground-based lidar measurements.

Distribution of vertical wavelengths

With the assistance of the novel diagnostic tool WAVELET-SCAN, the distribution of vertical wavelengths was investigated without focusing only on dominant modes (see Fig. 4.6). The majority of waves exhibit vertical wavelengths larger than 15 km, a value which was used as cutoff wavelength in the E_p analysis in many previous studies. This result suggests that derived GW potential energies based on a cutoff at 15 km are underestimated.

Realistic GW potential energies

The comparison of λ_{15km} , λ_{30km} and realistic GW potential energies reveals that the λ_{15km} E_p analysis, the method traditionally used in literature, underestimates realistic wave energies by a factor of ~ 2 (see Fig. 4.12 and Fig. 4.13). This is connected to the fact that vertical wavelengths are often longer than 15 km in the Southern Andes region. However, simply increasing the spectral cutoff to 30 km leads to an overestimation of realistic wave energies due to instantaneous high-frequency ($\lambda_z \leq 30 \text{ km}$) components in the temperature background such as in SDTs. The prior determination of the temperature background in Chapter 3 was crucial for a realistic estimation of GW potential energies. The mentioned saturation limit should actually be considered to be at $\sim 180 \text{ J kg}^{-1}$. The GW intermittency remains unaltered.

Chapter 5

Propagation of Hydrostatic Rotating Mountain Waves

CORAL measurements in the middle atmosphere above Río Grande reveal extraordinary stratospheric GW potential energies. In individual cases, energies increase drastically within a very confined altitude range and this increase might be the result of quasi-stationary MWs propagating horizontally through CORAL's FOV. The horizontal propagation of MWs is not only predicted by theory (Queney, 1948, Gill, 1982) but also observed in satellite data (Hindley et al., 2015) and has been shown in raytracing studies (Preusse et al., 2009, Sato et al., 2012). In this work also a raytracing approach is chosen to study the horizontal propagation, but the novelty is the comparison with measurements. The combination of measurements and results from raytracing enables the investigation of the forcing and propagation conditions of MWs in an idealized linear propagation environment and in the real atmosphere.

5.1 Ray Theory

Let's approximate a GW locally as sinusoidal such that an arbitrary atmospheric variable q can be expressed as

$$q = Q(\vec{x}, t) \exp(i\tau(\vec{x}, t)) \quad (5.1)$$

with amplitude Q and phase τ as functions of space \vec{x} and time t . Wave frequency and wavenumbers can then be written as

$$\omega = \frac{\partial \tau}{\partial t} \quad \text{and} \quad k_i = -\frac{\partial \tau}{\partial x_i}. \quad (5.2)$$

After computing the time derivative of \vec{k} and the spatial gradient of ω , combining both formulas yields

$$\frac{\partial k_i}{\partial t} + \frac{\partial \omega}{\partial x_i} = 0. \quad (5.3)$$

As ω is generally a function of \vec{k} and \vec{x} , one can write

$$\frac{\partial k_i}{\partial t} + \frac{\partial \omega}{\partial k_j} \frac{\partial k_i}{\partial x_j} = -\frac{\partial \omega}{\partial x_i} \quad (5.4)$$

$$\frac{\partial k_i}{\partial t} + \vec{c}_g \cdot \vec{\nabla} k_i = -\frac{\partial \omega}{\partial x_i}. \quad (5.5)$$

Please note that in (5.4) Einstein's summation convention is used. The derivative of ω with respect to wavenumber is familiar from (4.16) and (4.17) and represents the wave group velocity, i.e. the speed at which wave energy propagates. The left side of (5.4) represents the Lagrangian derivative of \vec{k} such that (5.4) can be written as

$$\frac{Dk_i}{Dt} = -\frac{\partial \omega}{\partial x_i}. \quad (5.6)$$

Equation (5.6) specifies the refraction of wave energy. It describes how the orientation of the wave vector changes along the path of energy propagation, i.e. along *rays*. The interested reader is referred to Lighthill (1978).

5.2 GROGRAT Simulations

Raytracing can be used to simulate the four dimensional propagation of individual GWs (e.g. Preusse et al., 2002, Ehard et al., 2017, Geldenhuys et al., 2021) and to infer global distributions of wave momentum flux (Preusse et al., 2009). A well established tool is the Gravity wave Regional Or Global RAY Tracer (GROGRAT) (Eckermann, 1992, Marks and Eckermann, 1995). GROGRAT is based on the nonhydrostatic, rotational GW dispersion relation (4.10). The full set of equations is given by Marks and Eckermann (1995) and here recalled:

$$\frac{dx}{dt} = u + \frac{k(N^2 - \hat{\omega}^2)}{\hat{\omega}\Delta} \quad (5.7)$$

$$\frac{dy}{dt} = v + \frac{l(N^2 - \hat{\omega}^2)}{\hat{\omega}\Delta} \quad (5.8)$$

$$\frac{dz}{dt} = -\frac{m(N^2 - \hat{\omega}^2)}{\hat{\omega}\Delta} \quad (5.9)$$

$$\frac{dk}{dt} = -ku_x - lv_x - \frac{1}{2\hat{\omega}\Delta} \left[N_x^2(k^2 + l^2) - \alpha_{h,x}^2(\hat{\omega}^2 - f^2) \right] \quad (5.10)$$

$$\frac{dl}{dt} = -ku_y - lv_y - \frac{1}{2\hat{\omega}\Delta} \left[N_y^2(k^2 + l^2) - \alpha_{h,y}^2(\hat{\omega}^2 - f^2) \right] - \frac{ff_y}{\hat{\omega}\Delta} (m^2 + \alpha_h^2) \quad (5.11)$$

$$\frac{dm}{dt} = -ku_z - lv_z - \frac{1}{2\hat{\omega}\Delta} \left[N_z^2(k^2 + l^2) - \alpha_{h,z}^2(\hat{\omega}^2 - f^2) \right] \quad (5.12)$$

The symbol Δ is given as $\Delta^2 = k^2 + l^2 + m^2 + \alpha_h^2$. More generally, due to transient conditions, ω is also a function of time, and one last equation is added to the raytracing equations (Eckermann and Marks, 1996):

$$\frac{d\omega}{dt} = ku_t + lv_t + \frac{1}{2\hat{\omega}\Delta} \left[N_z^2(k^2 + l^2) - \alpha_{h,z}^2(\hat{\omega}^2 - f^2) \right] \quad (5.13)$$

The subscripts refer to partial derivatives. Please note that $\omega = \hat{\omega} + \vec{u} \cdot \vec{k}$ and therefore Equations (5.7) – (5.13) describe the propagation of waves with respect to a ground-relative inertial system.

Initially, a wave vector is prescribed by defining the set $\{\omega, k, l\}$ and placed at location (λ, ϕ, z) in a smooth background atmosphere. From (4.10) the initial m is determined. Equations (5.7) – (5.13) yield the new position (λ, ϕ, z) and a new set $\{\omega, k, l, m\}$ after the time step δt . By solving the equation system for multiple time steps, one obtains coordinate points as function of time or wave trajectories.

In the absence of wave dissipation, the wave action density $\mathcal{A} = E/\hat{\omega}$ is conserved along the rays and wave amplitudes are computed accordingly.

In this study, the background atmosphere is given by 6-hourly ERA5 data which are interpolated on a three-dimensional grid with $0.2^\circ \times 0.2^\circ$ horizontal resolution and 0.5 km vertical resolution. In order to exclude model-resolved GWs, ERA5 data are spectrally truncated at zonal wavenumber 18 and subsequently smoothed in the meridional and vertical by means of a Savitzky-Golay filter (see Strube et al., 2020). An 11 point fourth-order polynomial is used for the vertical filter, and a 25 point third order polynomial is used for the meridional filter. Rays are launched every 6 h at an altitude of 1.5 km. The simulation is performed up to an altitude of 64.5 km.

Even though the background atmosphere is smoothed, it may happen that the WKB assumption breaks down and the behaviour of simulated waves becomes unphysical. To check this, the WKB parameter, which is given as

$$\delta = \frac{1}{m^2} \left| \frac{\partial m}{\partial z} \right| \approx \left| \frac{1}{c_{gz} m^2} \frac{dm}{dt} \right| \quad (5.14)$$

is determined in each time step. The ray integration is stopped if $\delta \geq 1$, which happens when the wave approaches a reflection level or a critical level, i.e. $m \rightarrow \infty$.

5.2.1 Approximation of the Mountain Ridge of the Southern Andes

To define initial wave positions the Southern Andes mountain ridge is approximated in the following manner. First, the peaks of the topography as seen from a center point Z (initially Río Grande) are identified, and the distance d to the mountain peaks is determined as function of cardinal direction ς . Figure 5.1a shows that the distance to the highest mountain peaks increases approximately quadratically as ς varies from the south to the northwest. Mountain peaks are highest at $\sim 310^\circ$.

The center point is then moved northwards in steps of $\delta\phi = 0.1^\circ$, and an ellipse is fitted to the distance between the mountain peaks and Z . The radius of an ellipse as function of direction is defined as

$$R_e(\varsigma) = \sqrt{R_\lambda^2 \sin(\varsigma)^2 + R_\phi^2 \cos(\varsigma)^2}, \quad (5.15)$$

where R_λ and R_ϕ represent the radius of the ellipse in longitudinal and latitudinal direction, respectively. For each step $\delta\phi$, $R_e(\varsigma)$ is subtracted from d and the standard deviation is computed. When the standard deviation reaches a minimum, the ellipse

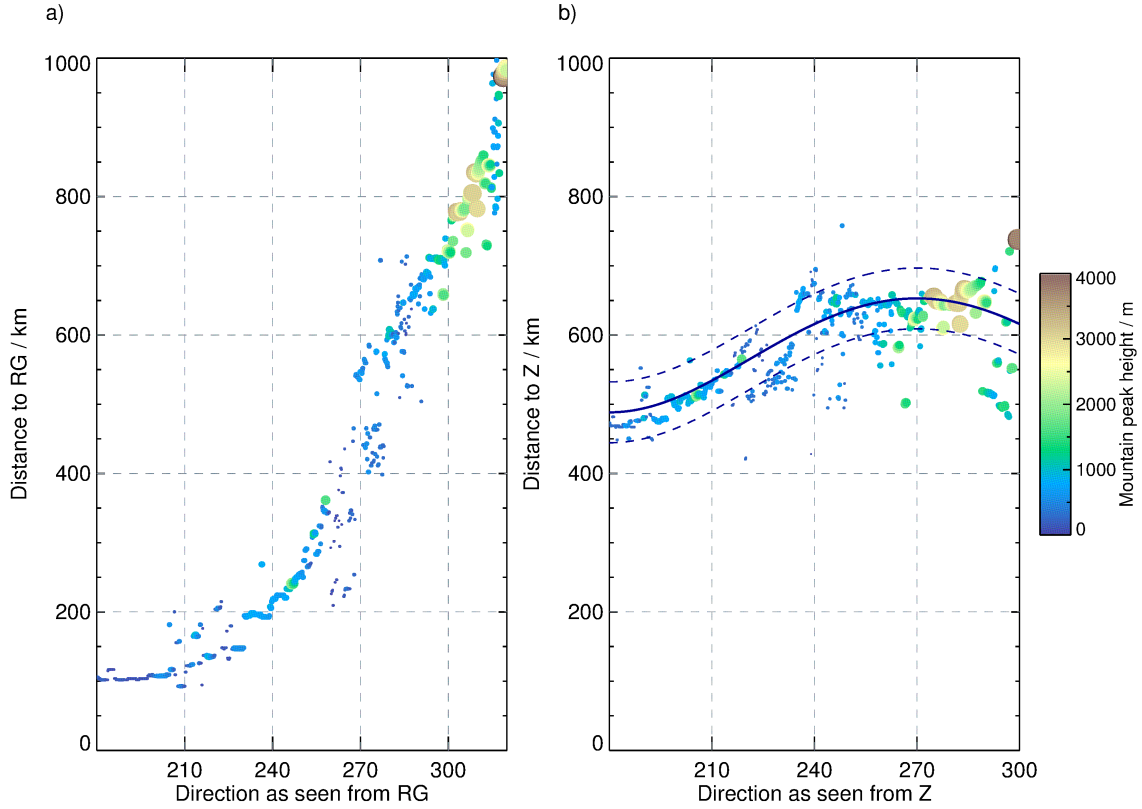


Figure 5.1: Shown is the distance d to mountain peaks as function of cardinal direction ζ as seen from Río Grande (a) and as seen from the center Z of a derived ellipse with $R_\lambda = 506$ km and $R_\phi = 425$ km (b). Colors and point diameter indicate the altitude of mountain peaks. The distance between the center Z and the approximated mountain ridge (solid) and standard deviation (dashed) is sketched.

that best approximates the mountain ridge is found. The distance to Z is shown in [Figure 5.1b](#). The longitudinal radius of the ellipse is $R_\lambda = 506$ km, and the latitudinal radius is $R_\phi = 425$ km. [Figure 5.2](#) illustrates the position of Río Grande in relation to Z as well as the ellipse itself. Please note that as Z is north of Río Grande, the peaks appear at different cardinal directions as seen from Río Grande. In the following analysis, the approximated mountain ridge is considered between 180° and 300° as seen from Z and shown in [Figure 5.2](#).

5.2.2 Initialization of Waves

The approximated mountain ridge is discretized into 120 equidistant locations and the normal vectors are determined on the ellipse. These normal vectors represent the direction of initialized MWs. Wave vectors initialized at 270° point westward from location Z , while vectors initialized at 180° point southward. In addition to the pointing of the wave vector, the spectrum of horizontal wavelengths is sampled by initializing wave vectors with horizontal wavelengths of $\{100, 200, 300, 400, 500, 600\}$ km at each point. Initial wave

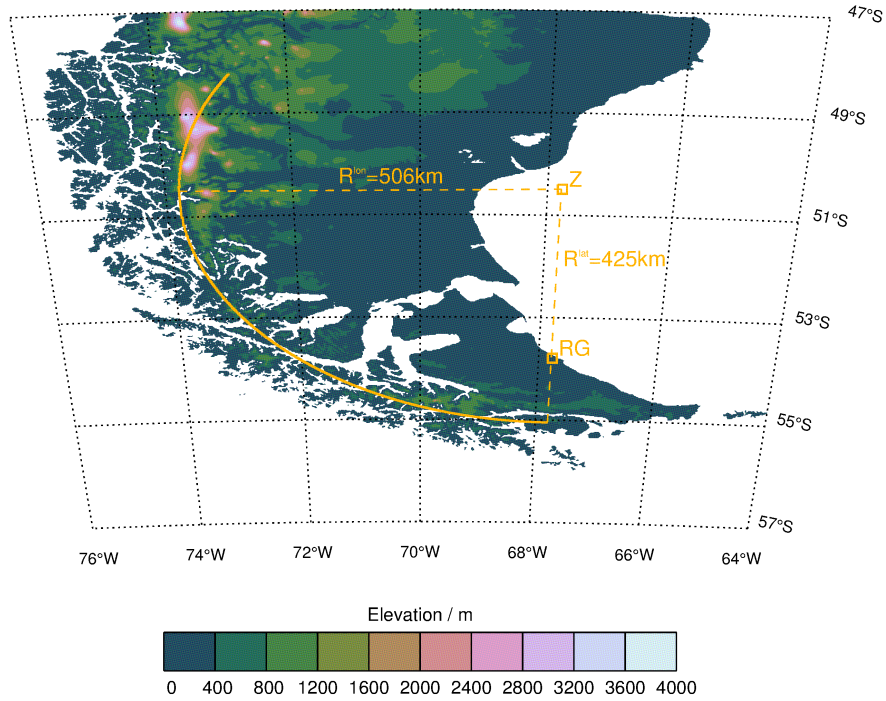


Figure 5.2: The topography of the Southern Andes is illustrated. ETOPO1 data is taken from the National Geophysical Data Center. The orange arc depicts the approximated mountain ridge with center point at Z .

amplitudes are computed according to $u' = N\zeta$, where ζ is the vertical displacement which is assumed to be equal to the height of the closest mountain peak. The amplitudes are very likely overestimated because blocking, which often occurs in this region, reduces the effective vertical displacement (Bacmeister et al., 1990). However, if wave amplitudes are overestimated, i.e. larger than maximum possible temperature amplitudes T_{max} (see 4.40), GROGRAT simply dampens them down to T_{max} . The observed frequency is initially $\omega = 0$. GROGRAT runs are carried out for the time periods March to October for each of the years 2018, 2019 and 2020. Hence, only the winter months are covered when deep propagation of MWs is expected.

5.2.3 Ray Analysis

GROGRAT provides 52 output parameters of which the following are used:

- (λ, ϕ, z, t) , the coordinates of the wave.
- (k, l, m, ω) , the wavenumbers and frequency of the wave.
- (u, v, N, T) , the background horizontal wind, stability, and temperature.
- T' , the saturated temperature amplitude of the wave. Whenever the conservative temperature amplitude would exceed the saturation amplitude (4.40) T' is set to the saturation amplitude.

All parameters are provided along the rays. In addition, the saturated temperature amplitude is reduced by a factor of $\sqrt{2}$ and E_p is computed along the ray using (4.19). The reduction in GROGRAT temperature amplitudes is necessary to make the potential energies comparable to the CORAL energies. The factor $\sqrt{2}$ is the ratio of ordinary amplitude and effective amplitude as determined by the RMS.

Prior to the analysis of GROGRAT data, a subset of rays is defined. CORAL measurements start at $z_i = 15$ km altitude and take place between the start time t_i and stop time t_f . The measurement is a point measurement in the horizontal plane. The rays also describe the simulated waves as points moving along a trajectory. The requirement that the launched waves cross CORAL's FOV is practically impossible to fulfill. To identify rays whose properties will later be compared with CORAL measurements, a window is defined based on the FOV. It is assumed that a wave extends over at least one oscillation in the horizontal and thus the following condition is required: $d_r < \lambda_h/2$, where d_r is the horizontal distance between the ray and Río Grande. Figure 5.3 illustrates rays of waves with $\lambda_h = 500$ km fulfilling the required condition. It becomes evident that only the northernmost waves cross CORAL's FOV and waves launched more southerly propagate quickly southwards not even reaching 15 km altitude. Since waves are launched only every 6 hours, in addition, it is required that $t_i - 3 \text{ h} < t < t_f + 3 \text{ h}$. A large number of rays is found fulfilling these criteria which suggests that the approach is reasonable, and the results confirm that large-scale MWs propagate horizontally from the approximated Southern Andes mountain ridge over Río Grande. The observed downwind propagation of large-scale MWs was shown in previous raytracing studies (e.g. Preusse et al., 2002, Sato et al., 2012) but not yet quantitatively investigated.

5.3 Forcing of Mountain Waves and Subsequent Propagation

It was shown in Section 4.2.1 that more than half of the sub-seasonal temperature perturbations are caused by quasi-steady \tilde{T} phase lines indicating quasi-stationary MWs. However, Río Grande is at least 100 km away from the closest mountain peak (Fig. 5.1a). It is located on the east coast of Tierra del Fuego and surrounded in the west by the southern foothills of the Andes (Fig. 5.2). Smaller mountains (~ 1000 m peak altitude)

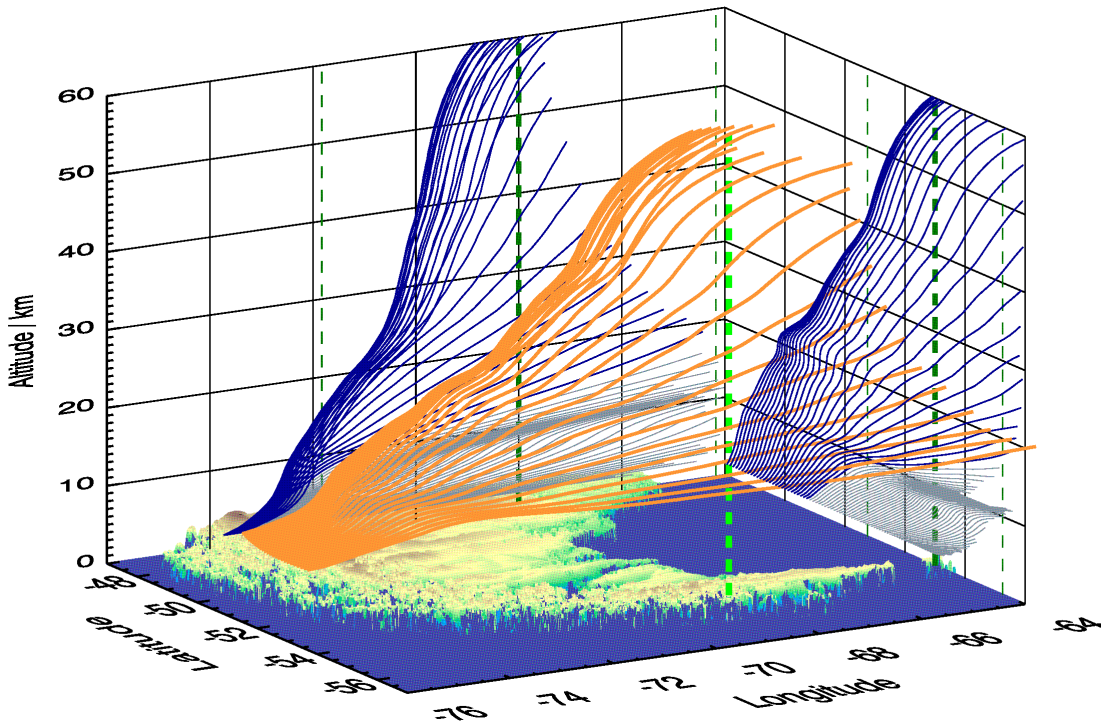


Figure 5.3: Illustrated is the topography of the southern tip of South America with rays of waves with $\lambda_h = 500$ km above (orange). Also, CORAL's laser beam is shown above Río Grande (dashed light green). The blue lines are projections of the rays on the (ϕ, z) -plane and (λ, z) -plane, respectively, to improve the 3D impression. Dashed lines in the (ϕ, z) -plane and (λ, z) -plane mark a distance equal to 500 km to illustrate the considered FOV ($d_r < \lambda_h/2$). The thin grey lines show the projection of rays of waves with $\lambda_h = 500$ km which do not reach 15 km altitude in the region under consideration.

are located in the south and west (one exception is Mt Darwin, with a peak altitude of 2488 m at ~ 150 km distance) while higher mountain peaks (e.g. Mt. Fitz Roy with a peak altitude of 3405 m at ~ 600 km distance) are far to the northwest (see Fig. 1.4). So where do the observed waves originate assuming that they are MWs? Short-scale ($\lambda_h < 100$ km) waves excited by smaller mountains and hills near Río Grande are one possibility. These would propagate primarily vertically and likely extend into the observation volume because of the horizontal proximity of the sources. An indication of these waves is the observations of MWs with $\lambda_h < 50$ km in airglow images (Pautet et al., 2021). Another possibility is large-scale ($\lambda_h > 100$ km) waves generated by the entire Southern Andean ridge, which propagate horizontally through the observation volume. In the following the forcing and propagation conditions of these large-scale waves are recalled. Figure 4.7 shows profiles of monthly mean wind speeds and directions at Río Grande taken from ECMWF. The ERA5 wind data are spectrally truncated at wavenumber T21 in order to filter out contributions from model-resolved GWs and obtain a smooth background wind field. First of all, there have to be sufficiently large tropospheric winds perpendicular to the mountain ridge to excite MWs there (e.g. Dörnbrack et al., 1999,

Kaifler et al., 2015a, Bramberger et al., 2017). In addition, Dörnbrack et al. (1999) report that suitable excitation and propagation conditions prevail when the wind turns no more than 30° within the first 30 km. Monthly mean wind speeds in ERA5 data are about 15 ms^{-1} at ground level (500 m) at all times. The wind rotation within the first 30 km is $< 30^\circ$ during the months March to October with an average southwesterly ground level forcing. Thus, in the climatological mean MWs are excited and able to propagate deep into the middle atmosphere in the winter months. A strong wind rotation within the first 30 km of about 60° can only be observed in July 2020. At this time, and in accordance with the theoretical expectations, reduced GW energies at all altitude regions are observed by CORAL (Fig. 4.8). Moreover, for deep vertical propagation, the MWs should not encounter critical levels or turning levels where the intrinsic frequency approaches the buoyancy frequency (e.g. Schoeberl, 1985). These conditions occur in the core of the PNJ and filter out MWs with short horizontal wavelengths or lead to evanescent modes with a certain probability of tunneling through the PNJ (e.g. Mixa et al., 2021). Another obstacle for MWs is the stratospheric wind minimum where the waves' u' -amplitude may become equal to the horizontal wind speed and cause wave breaking. This wind minimum can act as a valve for vertically propagating MWs (Kruse et al., 2016). Figure 4.7 reveals that low wind speeds at ~ 25 km altitude occur from March to May. In the winter months, with positive temperature gradients above the tropopause (Figure 2.5) and large horizontal wind speeds (Fig. 4.7) up to 50 km altitude, generally good vertical propagation conditions for MWs can be expected. Above, shear instabilities and unstable lapse rates can lead to wave dissipation. It is known that the mesosphere is the favorable region for generation of SGWs (Vadas et al., 2018, Vadas and Becker, 2019, Heale et al., 2020, Kogure et al., 2020). Large contributions of apparently upward and downward propagating waves and reduced contributions of stationary waves (Tab. 4.1) at mesospheric altitudes might indicate the existence of SGWs above Río Grande.

For large-scale MWs, linear theory predicts that the height and width of the mountain, the thermal stratification, and the strength of the flow define the initial magnitude of the energy and momentum that is transported by these waves (Gill, 1982). Smith et al. (2016) found no linear relationship between low-level (4 km) forcing and vertical momentum fluxes in the lower stratosphere (12 km), but they concluded that the forcing provides an upper bound for vertical momentum fluxes. Large-amplitude mesospheric GWs observed over New Zealand are correlated with both moderate to weak low-level tropospheric forcing (Fritts et al., 2016, Kaifler et al., 2015a) and with strong forcing (Bramberger et al., 2017). Kaifler et al. (2015a) have shown that mesospheric E_p that is associated with MWs increases significantly with larger stratospheric minimum wind speeds. Above the Andes, Smith et al. (2009) report on MWs in the mesosphere that were forced by a $\sim 70 \text{ m s}^{-1}$ tropospheric jet stream. In their studies, Kaifler et al. (2015a) and Smith et al. (2016) related the low-level wind to coincident wave energies and momentum fluxes in the middle atmosphere. However, the waves have a finite vertical group velocity, so time elapses between their excitation and observation. The time difference is proportional to $\lambda_h/u_{\parallel}^2$ and typically on the order of a few hours to one day (see Fig. 5.4c). Accordingly, the correlation between low-level forcing and wave energy or momentum flux is expected to be better when the horizontal wavelength is shorter and the horizontal wind is stronger. However, for large-scale waves ($\lambda_h > 100$ km), the correlation may break down because

first, they propagate more slowly in the vertical and second, their horizontal propagation is greater than their small-scale counterparts.

The raytracing simulations make it possible to precisely study the forcing of the observed MWs and to correlate the forcing with measured GW potential energies in the stratosphere. [Figure 5.4a](#) shows the horizontal wind projected onto the wave vector, i.e. $u_{||}$. The individual forcing u_f for a ray is defined as $u_{||}$ at 1.5 km altitude at the location and time of initialization. In other words, u_f is the horizontal wind that is perpendicular to the idealized mountain ridge. However, in the time window of a CORAL measurement, n rays are found entering CORAL's FOV, so the forcing is an average over all individual u_f associated with the n rays and thus most likely an average over different locations and times. The average forcing is denoted as \bar{u}_f . [Figure 5.4c](#) shows that waves with different horizontal wavelengths that superimpose in the stratosphere at a given point in time were excited with a time lag due to their different group velocities. In addition to forcing, the background atmosphere represents conditions that allow wave amplitudes to grow, stagnate, or shrink. The saturation amplitude (4.40) is used as a measure for the atmospheric background conditions which will be referred to in the following as *growth potential*. Profiles of growth potential are also illustrated in [Figure 5.4b](#). Plugging $m = N/u_{||}$ into (4.40) one gets

$$T_{\max} = \frac{u_{||}\bar{T}N}{g}. \quad (5.16)$$

The variables $u_{||}$, \bar{T} and N are all GROGRAT outputs along the rays. The average of T_{\max} along the ray between 2 km and an altitude of interest is computed to estimate the individual T_{\max} per ray. The overall $\overline{T_{\max}}$ describes the mean value over all individual saturation amplitudes per CORAL measurement night.

[Figure 5.5](#) shows the nightly mean GW potential energy $\langle E_p \rangle^\diamond$ computed from GROGRAT runs as function of forcing \bar{u}_f and growth potential $\overline{T_{\max}}$ for the altitude ranges of 20 – 35 km, 35 – 50 km and 50 – 65 km. In the stratosphere, $\langle E_p \rangle^\diamond$ increases with \bar{u}_f and $\overline{T_{\max}}$ ([Fig. 5.5a, b](#)). The latter is confirmed by the correlation coefficient which is almost 0.7 at all three altitude ranges. Hann smoothed $\langle E_p \rangle^\diamond$ in the upper stratosphere indicates that energies do not increase arbitrarily – there is a limit of $\bar{u}_f > 20 \text{ m s}^{-1}$ and $\overline{T_{\max}} > 25 \text{ K}$ ([Fig. 5.5b](#)). The correlation between $\langle E_p \rangle^\diamond$ and \bar{u}_f decreases in the lower mesosphere, meaning that variations in low-level forcing have less of an impact on mesospheric wave energies ([Fig. 5.5c](#)). In determining the correlation coefficients, the data were always reduced by one dimension. Thus, \bar{u}_f is neglected when determining the correlation between $\langle E_p \rangle^\diamond$ and $\overline{T_{\max}}$ and vice versa. However, since a non-negligible variance in $\langle E_p \rangle^\diamond$ occurs along the reduced dimension, a correlation coefficient of $r < 1$ is expected. Furthermore, the data show that $\overline{T_{\max}}$ influences $\langle E_p \rangle^\diamond$ more than \bar{u}_f . This is reflected in the larger correlation coefficients between wave energy and growth potential than between wave energy and forcing.

[Figure 5.6](#) shows the nightly mean GW potential energy derived from CORAL data as function of forcing and growth potential for the same altitude ranges as above and for 65 – 80 km. Please note that for this uppermost altitude range \bar{u}_f and $\overline{T_{\max}}$ are the same as for the altitude range 50 – 65 km since GROGRAT runs are terminated at about 65 km. That implies the assumption that waves which crossed the lower mesosphere would also enter

the upper mesosphere and do not exit the FOV of the lidar in between. Generally, the relationship between $\overline{u_f}$, $\overline{T_{\max}}$, and $\langle E_p \rangle^\diamond$ as retrieved from CORAL data is qualitatively similar to what is observed in GROGRAT runs. The wave energies increase with the strength of the forcing and with favorable background conditions. However, correlation coefficients are not as large as in the GROGRAT runs, and the increased variance might be a result of other phenomena that are not considered in GROGRAT simulations. In the upper mesosphere, the correlation between $\langle E_p \rangle^\diamond$ and $\overline{u_f}$ even becomes negative. If the correlation coefficient is not determined between $\langle E_p \rangle^\diamond$ and $\overline{T_{\max}}$, but between $\ln(\langle E_p \rangle^\diamond)$ and $\overline{T_{\max}}$, then r increases by about 0.2. This could be an indication of an exponential connection between wave energy and growth potential.

Wave energies in CORAL data are in the median a factor of 3.5 smaller than in GROGRAT data. In addition, a larger $\langle E_p \rangle^\diamond$ variance is observed in CORAL measurements. The discrepancies may arise due to the following reasons. First, GROGRAT models linear waves and does not account for any non-linear process such as dissipation or wave-wave-interaction. In reality though, waves interfere, which can temporarily lead to increased or reduced wave amplitudes. Second, MWs that have different horizontal wavelengths than the launched spectrum and that were excited at other locations also contribute to the measured GW potential energy. Non-orographic sources also contribute to measured $\langle E_p \rangle^\diamond$. This non-orographic $\langle E_p \rangle^\diamond$ contribution likely increases with altitude and thus reduces the correlation.

5.4 Horizontal Propagation of Quasi-Stationary Mountain Waves

When it comes to the horizontal propagation of quasi-stationary MWs, three aspects must be considered. First, as discussed above, the horizontal group velocity depends on the intrinsic frequency of the wave. As $\hat{\omega}$ approaches f , the wave propagates apparently more downwind. “Apparently” because the intrinsic propagation direction is still against the prevailing wind.

Because MWs satisfy $\hat{\omega} = -u_{||}k_h$, significant horizontal propagation takes place for small horizontal wind speeds and large wavelengths. However, the minimum wind speed must be $u_{||} > f/k_h$ which is known as the Jones critical level (Jones, 1967). Second, Sato et al. (2012) have shown that, if there is a component of the wind vector u_{\perp} that is perpendicular to the wave vector, a lateral propagation of the wave occurs. The corresponding figure from Sato et al. (2012) is presented in Figure 5.7. From the point of view of the intrinsic group velocity \hat{c}_g , the observed propagation c_g takes place perpendicular to the wave vector. This propagation is called lateral propagation. However, the sketch is not complete because it neglects the horizontal

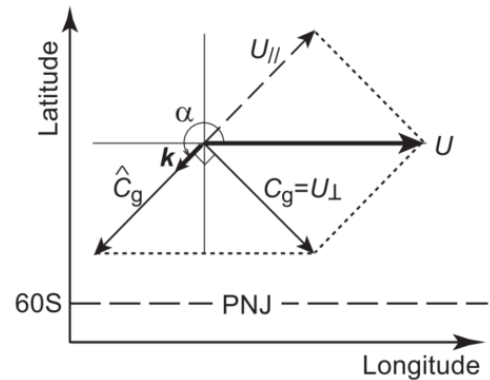


Figure 5.7: The figure is taken from Sato et al. (2012).

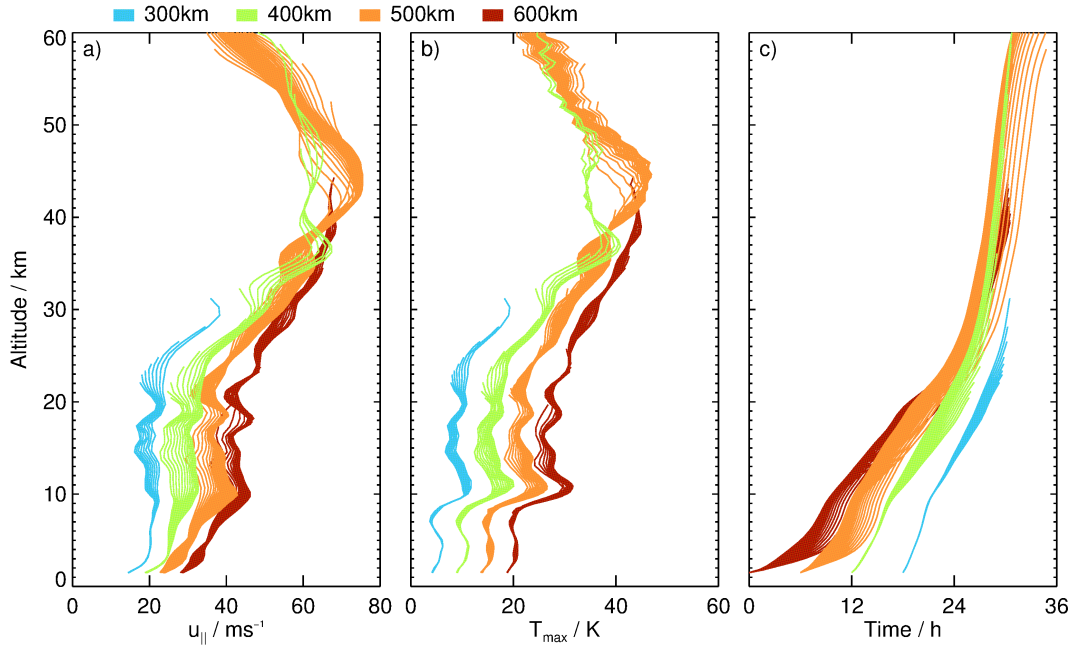


Figure 5.4: Depicted is the horizontal wind speed parallel to the wave vector (a), the saturation amplitude (b) and the rays in (t, z) -space (c) during propagation for all rays that are considered to enter CORAL’s FOV. The colors differentiate between horizontal wavelengths. For illustration reasons, the profiles in (a), (b), and (c) are shifted by 5 m s^{-1} , 5 K , and 6 h respectively.

propagation parallel to the wave vector into the lee (see [Equ. 4.17](#)). From the point of view of the wave vector, the wave propagates backwards. Therefore this propagation is called backward propagation in this work. Finally, from raytracing equations it is known that horizontal shears in the wind field cause wave vectors to turn. That in combination with the backward and lateral propagation causes MWs to extend over vast areas downstream of the mountains. It was found that MWs are mostly refracted into the PNJ ([Sato et al., 2012](#)). This was also earlier reported by [Dunkerton \(1984\)](#) and more recently by [Ehard et al. \(2017\)](#) who studied lidar observations in the vicinity of the Southern Alps of New Zealand.

In this work it is investigated how the waves propagate from their source regions to Río Grande and possibly beyond. Due to the preselection of the rays ([Sec. 5.2.3](#)), most rays exhibit southeastward propagation. However, the question arises: How exactly do the waves propagate, and what role do horizontal wind shears have? To investigate this further, two scenarios are considered, a northwesterly and a southwesterly forcing. At the same time, the analysis is restricted to the winter months of May through August, as this is when the meridional gradient in the zonal wind is strongest.

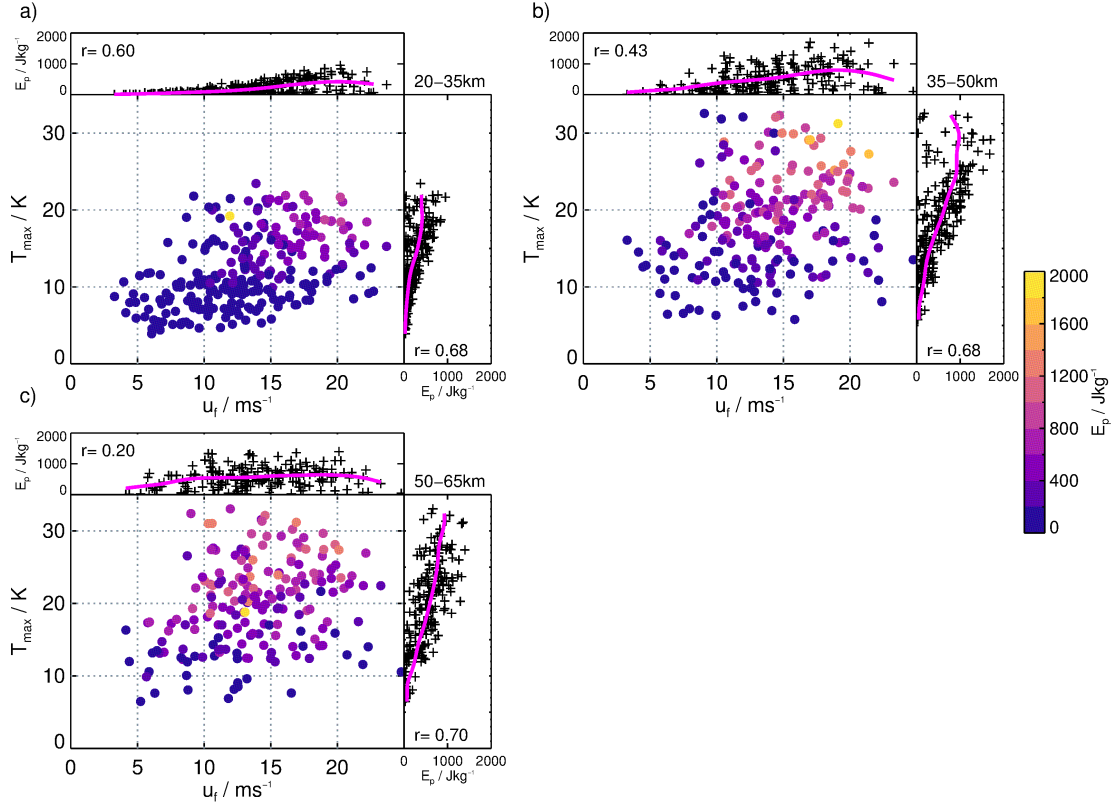


Figure 5.5: Depicted is the average GW potential energy per measurement night $\langle E_p \rangle^\diamond$ derived from GROGRAT runs as function of forcing wind speed \bar{u}_f and growth potential \bar{T}_{\max} and for altitude ranges 20 – 35 km (a), 35 – 50 km (b) and 50 – 65 km (c). To the right and top $\langle E_p \rangle^\diamond$ as function of \bar{u}_f and \bar{T}_{\max} is shown, respectively. Magenta curves show $\langle E_p \rangle^\diamond$ values that are Hann smoothed with window lengths of 8 m s^{-1} and 8 K , respectively. Pearson correlation coefficients r are given.

Figure 5.8 illustrates the mean propagation of MWs with $\lambda_h = 500 \text{ km}$ under southwesterly forcing conditions. From an intrinsic point of view, MWs propagate against the forcing wind in a southwestward direction at initialization ($z = 1.5 \text{ km}$), which results in an angle close to 180° between wave and wind vector. That results in very little lateral propagation such that the observed propagation is almost congruent with the backward propagation that is substantial at this altitude due to rather small horizontal wind speeds. At 10 km altitude, the wind speed doubles, and the wind direction turns slightly anti-clockwise such that the waves experience a northward shift. The situation changes drastically at 25 km altitude. The wind speed has doubled again and is now at about 60 m s^{-1} while the wind direction is approximately eastward. Yet, the wave vector barely alters its orientation, which causes an enhanced lateral propagation towards the southeast. This situation barely changes up to 40 km where wind speeds increase to 100 m s^{-1} , leading to an even faster observed group velocity. In the stratosphere, where winds become westerly, it is found that lateral propagation is up to ten times stronger than backward propagation. Figures 5.8c, d are very similar to the sketch from Sato et al. (2012) (Fig. 5.7) and make

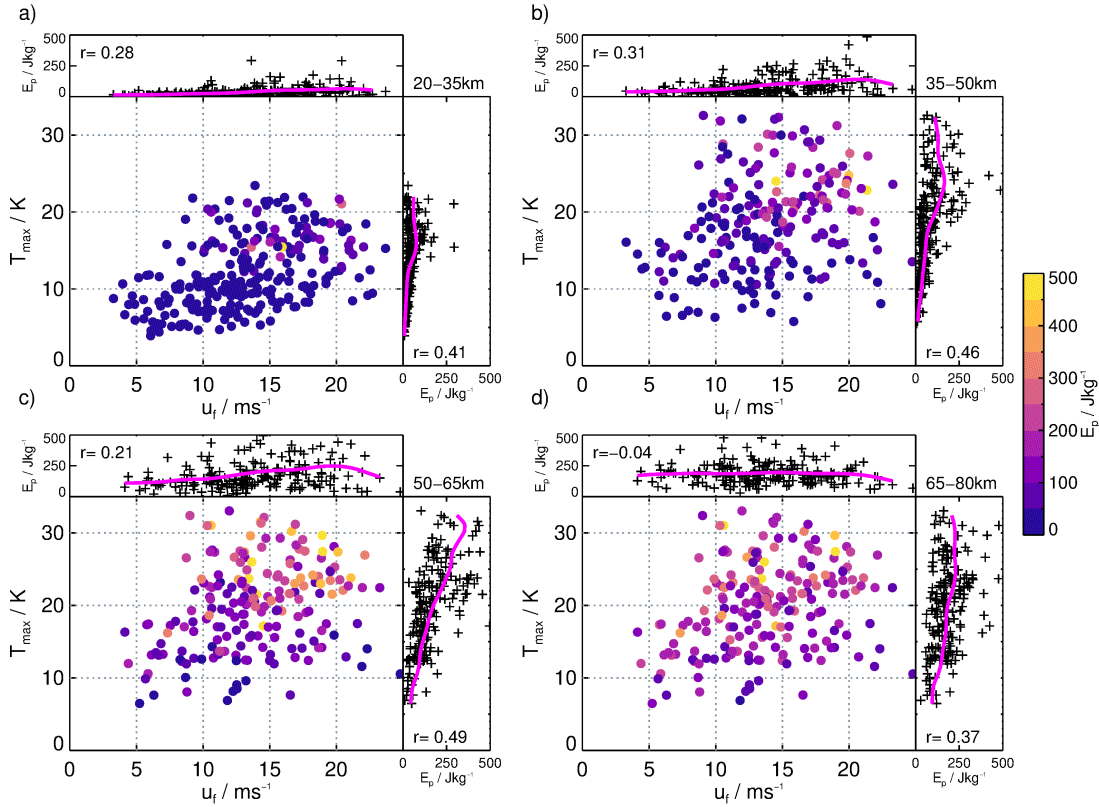


Figure 5.6: Same as [Figure 5.5](#) but for $\langle E_p \rangle^\diamond$ values derived from CORAL data. The additional altitude range 65 – 80 km is illustrated in (d). Therein $\overline{u_f}$ and $\overline{T_{\max}}$ are the same as for the altitude range 50 – 65 km.

it clear that backward propagation plays only a minor role in the case of southwesterly forcing.

[Figure 5.9](#) illustrates the mean propagation of MWs under northwesterly forcing conditions. At initialization ($z = 1.5$ km), wave vector and wind vector enclose an angle of about 150° which immediately produces lateral propagation and an observed group velocity in a southeastward direction. Up to 40 km altitude, the wind vector turns to a westerly direction and wind speeds increase to approximately 90 m s^{-1} . The enclosed angle remains at about 160° which results in an observed continuous southeastward propagation. In the entire altitude range, about two to three times more lateral propagation than backward propagation is observed. The net result is similar to [Figure 5.7](#). However, this time the backward propagation is more important because the angle between the wave and the wind vector is larger.

What is to be learned from this analysis? The forcing determines the orientation of the waves. At least waves with rather large horizontal wavelengths ($\lambda_h > 100$ km) alter their propagation directions only within a range of $\pm 10^\circ$ between the point of initialization at the approximated mountain ridge and 50 km altitude above Río Grande. The consequence is that a westerly forcing generates MWs that remain close to their source while a southwesterly forcing generates MWs that experience strong lateral propagation. These

results confirm what was found by Jiang et al. (2013) and Jiang et al. (2019).

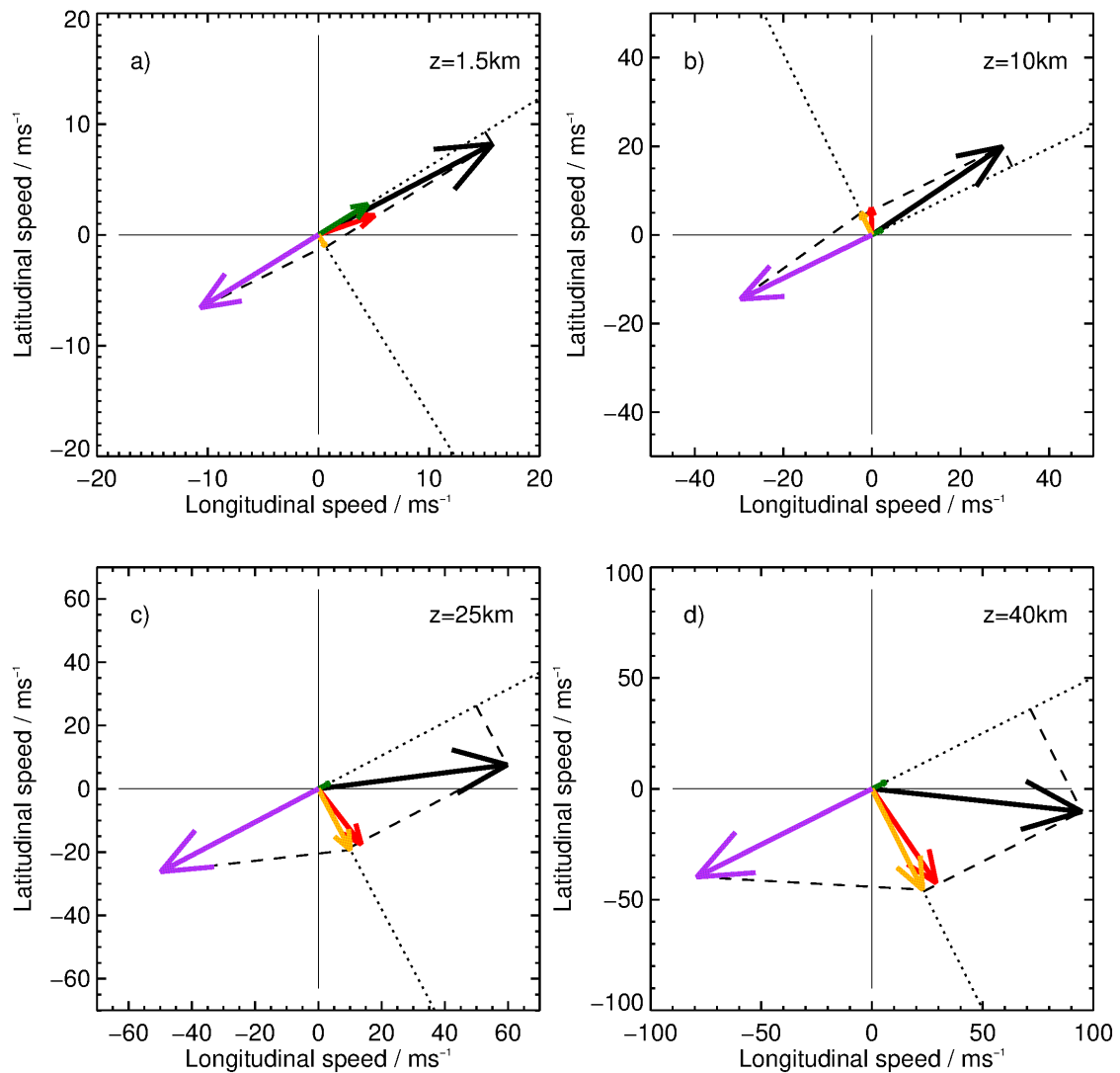


Figure 5.8: Illustrated is the propagation of MWs under southwesterly forcing conditions at altitudes of 1.5 km (a), 10 km (b), 25 km (c) and 40 km (d). Arrows depict the horizontal wind (black), intrinsic group velocity (purple), backward propagation (green), lateral propagation (orange) and observed propagation (red).

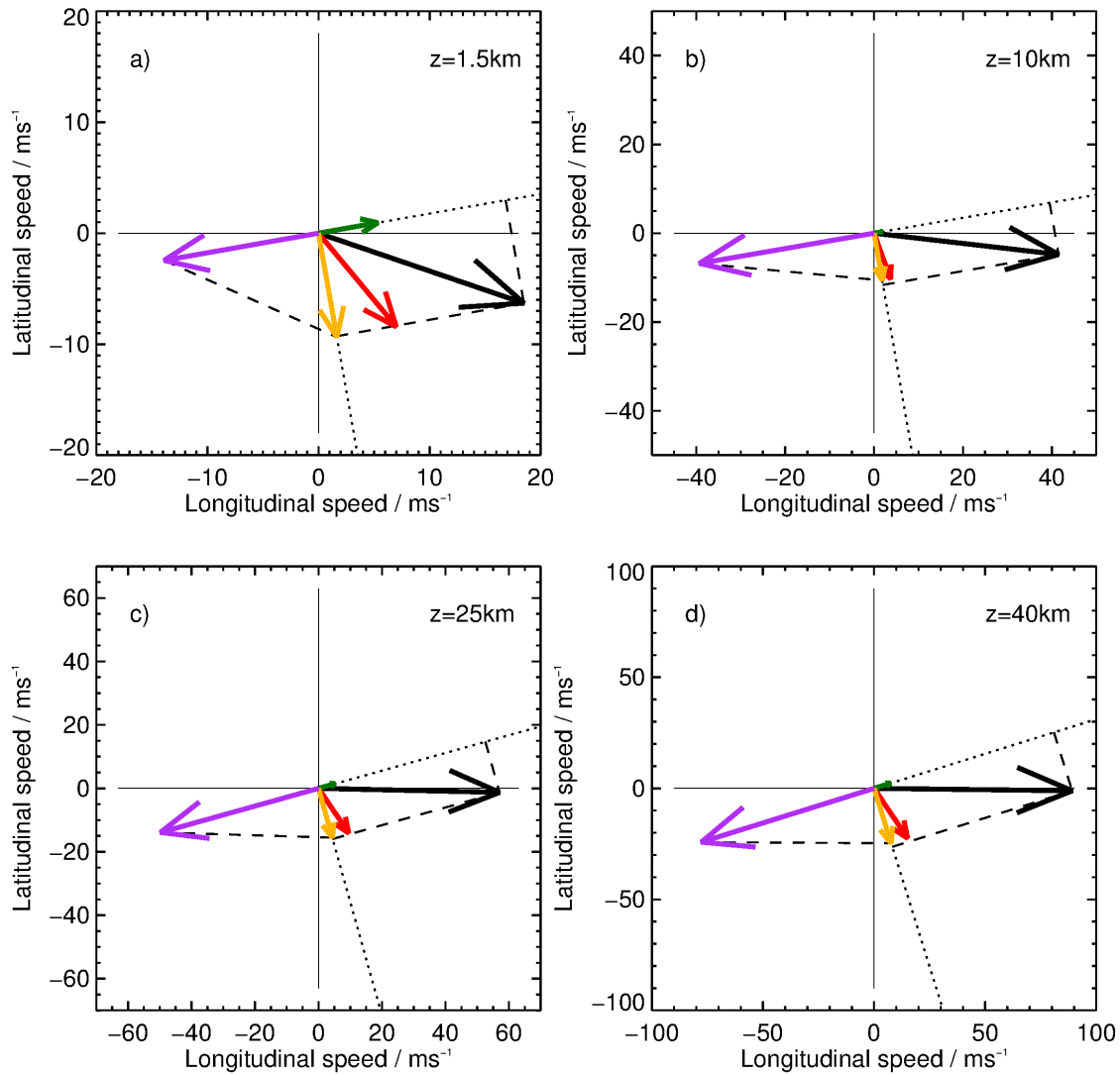


Figure 5.9: Same as Figure 5.8 but for northwesterly forcing conditions.

5.5 Summary and Answer to Research Question (R3)

The observation of MWs over Río Grande and the large distance to the mountain peaks of the Southern Andes can only be reconciled by assuming that the observed MWs are generally large-scale ($\lambda_h > 100\text{ km}$) waves, since only these can propagate horizontally over long distances. In a raytracing study it was investigated whether or not these large-scale waves can propagate from their source region to Río Grande. Furthermore, for the first time, excitation and propagation conditions derived from raytracing simulations

were related to measured middle atmospheric GW potential energies. The third research question is:

(R3) What are the forcing and propagation conditions of observed quasi-stationary mountain waves over Río Grande? How do the modelled gravity wave potential energies compare with the CORAL observations?

1. Measured GW potential energies in CORAL data are in the median 3.5 times smaller than GW potential energies derived from GROGRAT runs. This might be attributed to overestimated initial wave amplitudes in GROGRAT simulations, since in their calculation the mountain ridge height ($\zeta_{\max} = 3400$ m) was used as the initial vertical displacement amplitude. However, due to low-level flow blocking (Bacmeister et al., 1990) the effective initial wave amplitude is certainly smaller than the one that was used in the simulations. Besides, GROGRAT does not account for non-linear processes such as wave-wave-interaction which leads to wave interference and therefore could result in dampened wave amplitudes.
2. From the GROGRAT runs good linear correlation ($r = 0.7$) was found between GW potential energy and growth potential at all altitudes (Fig. 5.5). On the other hand, the linear correlation between low-level forcing wind speed and GW potential energy decreases with altitude. Hence, it is concluded that in the linear GROGRAT picture, the variation of GW potential energy is dictated by the background atmosphere and not by the forcing conditions.
The correlation between measured GW potential energies in CORAL data and the low-level forcing is not strong and weakens with altitude, which is probably due to interference between waves and an increasing contribution from non-orographic GWs. This result is similar to what was observed by Kaifler et al. (2015a) and Smith et al. (2016).
3. The logarithm of measured GW potential energy in CORAL data shows a good linear correlation ($r = 0.65$) with the growth potential in the lower and upper stratosphere and lower mesosphere, which is indicative of an exponential connection between wave energy and growth potential (Fig. 5.6). For the GROGRAT runs, no change in the correlation coefficient was observed by taking the logarithm of the wave energy. It is concluded that under linear wave theory assumptions wave energy and growth potential show a linear correlation while in reality both variables are exponentially linked.
4. The forcing determines the initial wave orientation in the horizontal plane (Fig. 5.9). Horizontal wind shears along the ray do not significantly change the orientation at least for the considered large-scale ($\lambda_h > 100$ km) waves. Consequentially, the ratio between lateral and backwards propagation is about 10:1 in case of a southwesterly forcing. This case is comparable to the trailing waves in (Jiang et al., 2013). In the case of a northwesterly forcing, the ratio between lateral and backwards propagation is about 3:1. The (Sato et al., 2012)-picture is incomplete in this case as it neglects the backwards propagation.

Chapter 6

Conclusions and Outlook

Three years of high-cadence ground-based lidar temperature data were analyzed from the middle atmosphere acquired at Río Grande, an Argentinian town at the southern tip of South America. This PhD thesis focused on the investigation of GW signatures in those data which were known to occur frequently at this location and with exceptionally large amplitudes in austral winter. The autonomous operation of the lidar system CORAL in combination with good weather conditions in the lee of the Southern Andes led to a unique data set of over 3,000 h duration covering the altitude range of 15 km – 90 km (see [Fig. 2.4](#), [Fig. 2.5](#) and [Tab. 2.1](#)). The aim of this thesis was to characterize GWs at this hotspot region by inferring their properties such as their amplitudes and vertical wavelengths from the temperature soundings. It was hypothesized that the observed waves in austral winter can be attributed to the hydrostatic rotating wave regime as individual mountain peaks which would serve as sources for hydrostatic nonrotating waves are at least 150 km away (see [Fig. 1.4](#)). Before addressing this, it was wondered if the high cadence of measurements was sufficient to define a reliable temperature background incorporating seasonal oscillations, PWs, and tides. The difference between this background and the original measurements would then reveal realistic GW signals.

In order to retrieve DTs from irregularly sampled CORAL and regularly gridded ERA5 data, the DT-R2D fit was developed ([Sec. 3.1.2](#)). Reasonable agreement was found between the DT properties in CORAL and ERA5 data in the stratosphere ([Fig. 3.11](#)). The results were also consistent with previous findings at mid- to high-latitudes (e.g. [Lübken et al., 2011](#), [Pancheva and Mukhtarov, 2011](#), [Kopp et al., 2015](#), [Baumgarten and Stober, 2019](#)). However, in the mesosphere, DT amplitudes in CORAL data exceeded amplitudes in SABER data ([Pancheva and Mukhtarov, 2011](#)) which might be due to a local anomaly. On the other hand, it remains unclear to which degree large-scale ($\lambda_z > 15$ km) GWs and semi-diurnal and ter-diurnal tides affect the DT-R2D fit. Measurement nights that are too short do not allow for a reliable retrieval of DT properties in austral summer. After all, DTs are not the focus of this work; they only contribute a part to the determination of the temperature background.

Temperature perturbations with periods between 9 days and 45 days in CORAL data agree well with ERA5 data ([Fig. 3.13](#)). A dominant period in the order of ~ 30 days was identified as a quasi-stationary wave-1 which is regularly observed in the southern hemisphere mid- to high-latitudes ([Randel, 1988](#)). Larger wavenumbers like wave-2 are reported to

occur too, but they have not been studied in detail in this work. Wavenumbers beyond 2 are likely prohibited to propagate vertically due to strong stratospheric zonal mean zonal winds.

The investigation of seasonal oscillations revealed two maxima in the amplitude of the AO which are weaker than previously reported (Fig. 3.14). On the other hand, SAOs are found to have larger amplitudes than reported so far. It is argued that deviations are due to tidal aliasing as well as local phenomena. Also, enhanced wave-1 activity at the beginning and end of the winter season causes leakage of variance to the SAO (Gao et al., 1987, Randel, 1988).

It should be considered to make CORAL daylight-capable in the near future to increase the measurement cadence further in order to derive tides and PWs with higher accuracy and thus decrease aliased amplitudes of seasonal oscillations. This would lead to better constraints on the temperature background and thus to more precise measurements of GWs in the middle atmosphere. Besides, identifying tides in lidar data is key to quantifying their interaction with GWs since tides do not only alter the buoyancy frequency (Preusse et al., 2001) but also the background wind field (Baumgarten and Stober, 2019). Most recently Pautet et al. (2021) reported on the interaction of tides and observed MWs in the MLT region above Río Grande from measurements in the OH-airglow layer.

After the temperature background is defined, the observed GWs were characterized. The proximity to the Andean mountain ridge suggests that the majority of observed GWs are MWs. In order to confirm this, the 2D wavelet transform is used to investigate the orientation of phase lines in CORAL's temperature data. It turns out that in the majority of cases phase lines are steady in time-height cross sections, indicating that MWs dominate over transient waves at all altitudes in the climatological mean (Tab. 4.1). This is different from the results in Kaifler et al. (2015a) where the MW fraction decreases with altitude. In the analysis of GW potential energies three scale separation schemes were compared. In the first, temperature perturbations were derived via the application of a high-pass Butterworth filter on temperature profiles with a cutoff wavelength of 15 km (λ_{15km} -scheme). For reasons of comparison with previous studies the GW potential energy and its evolution was analyzed based on this λ_{15km} -scheme in time (Fig. 4.8) and altitude (Fig. 4.9). Also, statistical parameters like the Gini coefficient, the geometric standard deviation, and the skewness of wave energy distributions were computed based on the λ_{15km} -scheme (Tab. 4.2). In the second scale separation scheme, temperature perturbations were derived in a similar way to the first but setting the cutoff wavelength to 30 km (λ_{30km} -scheme). GW potential energies based on the λ_{30km} -scheme contain a significant contribution from tides and PWs (see also Fig. 3.1). In the third separation scheme, the predefined temperature background including DTs and PWs was subtracted from original temperature measurements (realistic-scheme). Subsequently, a high-pass filtering with a cutoff wavelength of 30 km was applied to make derived wave energies comparable to the λ_{30km} -scheme. It became evident that GW potential energies in the realistic-scheme were about a factor of 2 larger than in the λ_{15km} -scheme at all altitudes (Fig. 4.13). The following statements are based on the realistic-scheme. A factor of 10 between measured GW potential energies in summer and winter was found in the lower mesosphere. This is connected to unprecedented large wave energies at this altitude in austral winter, which

were found to reach a saturation limit on the order of $\sim 180 \text{ J kg}^{-1}$ at 60 km altitude. No other study to date has demonstrated reaching a saturation limit at an altitude as low as 60 km. It is argued that saturation at such low altitudes is due to strong forcing and excellent propagation conditions. Reaching the saturation limit at low altitudes (see also Fig. 4.11) might also be responsible for the observed decrease in GW intermittency at mesospheric altitudes. These results are in line with the wintertime observations of a turbulent mesosphere at high northern latitudes (Lübken, 1997). A factor of 2 between wave energies in the realistic and the λ_{15km} -scheme is attributed to the occurrence of waves with vertical wavelengths significantly longer than 15 km. In order to investigate the distribution of vertical wavelengths, the novel diagnostic tool WAVELET-SCAN was developed which does not focus solely on dominant spectral amplitudes but also differentiates between superimposed wave packets (Sec. 4.1.7). WAVELET-SCAN revealed that more than 50% of detected waves exhibit vertical wavelengths larger than 16.5 km (Fig. 4.6). Due to very strong horizontal winds above Río Grande in austral winter, MWs can reach very long vertical wavelengths which make it difficult to distinguish them from e.g. SDTs. Generally speaking, MWs superimpose with non-orographic GWs, tides, PWs, and the atmospheric background which results in a complex pattern. If wave amplitudes become large enough, the waves break and cannot be described by linear theory anymore. For the spatio-spectral analysis of large-amplitude GWs, other more sophisticated tools have to be developed that can be applied to non-linear and non-stationary data.

Exceptional growth rates of GW potential energy, a dominance of stationary phase lines, and wave events lasting a whole week (see Kaifler et al., 2020b) are indications for hydrostatic rotating MWs. In the last chapter of this thesis, the propagation of these quasi-stationary large-scale ($\lambda_h > 100 \text{ km}$) MWs was investigated accounting for their horizontal structure. A comprehensive raytracing study was carried out and forcing conditions, i.e. low-level horizontal wind parallel to the initialized wave vectors, were correlated with measured GW potential energies in the realistic-scheme (Fig. 5.6). A strong correlation between forcing and wave energy was not found but rather a weakening of the correlation with altitude is observed. In addition, the correlation of wave energies was studied with the saturation temperature amplitude, i.e. the amplitude when the wave becomes convectively unstable. This proxy that is called growth potential was used in the correlation analysis as it is based on background variables reflecting atmospheric conditions such as temperature, thermal stability, and horizontal wind. An exponential relationship could be found between the growth potential and measured GW potential energies in the stratosphere and lower mesosphere. The major differences between computed wave energies from CORAL and from the raytracer GROGRAT (factor of 3.5) are assigned to an overestimation of initial wave amplitudes due to the disregard of low-level flow blocking. Also, GROGRAT does not account for non-linear wave physics such as dissipation or wave-wave interaction. In addition, it was shown that the low-level forcing defines the orientation of waves even if the wind turns with altitude (Fig. 5.8). Besides, even large horizontal shear is generally not sufficient to rotate the wave vector by more than 10° . Therefore, trailing wave events usually occur under southwestward forcing conditions with prevailing westerlies in the stratosphere.

In conclusion, the results from the raytracing analysis support the central hypothesis.

Many simulated MWs cross CORAL's FOV and are observable above Río Grande. But then there is this observation of stationary GWs in OH-airglow directly over Río Grande by (Pautet et al., 2021). Either these are primary short-scale waves excited by smaller hills in the immediate vicinity of Río Grande, or - and this would be a physically exciting mechanism - they are stationary SGWs generated by large-scale breaking primary waves. Either way, the observation of these short-scale waves casts doubt on whether only hydrostatic rotating MWs exist in the lee of the southern Andes.

A lidar system such as CORAL is a remote sensing instrument with future potential. While future lidar systems will certainly have higher temporal and vertical resolution and reach greater altitudes, they will continue to perform only a point measurement in the (λ, ϕ) -plane. Making reliable statements about GWs manifesting in 4D space based solely on time-height cross sections of temperature is not possible. Not only is wind information missing, but also the horizontal structure of GWs, which provide information about momentum fluxes and potential Doppler shifts. Although lidar systems exist that can measure the horizontal wind in the middle atmosphere (Von Zahn et al., 2000), the horizontal structure of GWs remains obscured.

In case studies, lidar data are usually complemented with model data, ray-tracing analyses, etc. , in order to obtain an overall picture (e.g. Ehard et al., 2017). However, global model data usually have too low horizontal and temporal resolution and are increasingly unreliable above the stratopause (Gisinger et al., 2021). As discussed in Chapter 5, linear ray tracers are also of debatable utility at higher altitudes.

Nonlinear wave physics in the middle atmosphere can be studied with high-resolution numerical simulations (e.g. Mixa et al., 2021). Rather than inferring wave processes from lidar measurements, one should ask how wave processes manifest themselves in lidar measurements. The first steps in this direction have already been taken. Dörnbrack et al. (2017) investigated the effect of a Doppler shift on the interpretation of lidar data using the three-dimensional nonhydrostatic, compressible flow solver EULAG (Prusa et al., 2008). MWs of different regimes were also modeled in 2D to simulate lidar temperature profiles. Many more idealized scenarios still need to be simulated. Numerical modeling could thus be used to create a catalog of artificial lidar measurements that would serve as a basis for interpreting real lidar measurements.

Acronyms

AIRS	Atmospheric Infrared Sounder
AO	Annual Oscillation
CORAL	Compact Rayleigh Autonomous Lidar
COI	Cone of Influence
CWT	Continuous Wavelet Transform
DBSCAN	Density Based Spatial Clustering Algorithm with Noise
DT	Diurnal tides
EARG	Estación Astronómica Río Grande
ECMWF	European Center for Medium-Range Weather Forecasts
FFT	Fast Fourier Transform
GCM	General Circulation Model
GW	Gravity Wave
KDE	Kernel Density Estimation
LMSAO	Lower Mesospheric Semi-Annual Oscillation
MW	Mountain Wave
MSAO	Mesospheric Semi-Annual Oscillation
PDF	Probability Density Function
PNJ	Polar Night Jet
PSD	Power Spectral Density
PW	Planetary Wave
SABER	Sounding of the Atmosphere using Broadband Emission Radiometry

SAAMER	Southern Argentina Agile MEteor Radar
SAO	Semi-Annual Oscillation
SDT	Semi-diurnal tide
SouthTRAC-GW	Southern Hemisphere Transport, Dynamics, and Chemistry - Gravity Waves
SNR	Signal-to-Noise Ratio
SSAO	Stratospheric Semi-Annual Oscillation
WAVELET-SCAN	WAVELET analysis with subsequent density based Spatial Clustering Algorithm with Noise

Symbols

Sign	Description	Unit
A	Area of the telescope	m^2
\mathcal{A}	Wave action density	J s
a	Radius of the Earth	m
B_{AO}	Temperature amplitude of the annual oscillation	K
B_{DT}	Temperature amplitude of the diurnal tide	K
B_{SAO}	Temperature amplitude of the semiannual oscillation	K
C	Lidar system constant	
c	Velocity of light	m s^{-1}
c_{gz}	Vertical group velocity	m s^{-1}
c_{pz}	Vertical phase velocity	m s^{-1}
c_p	Heat capacity of dry air at constant pressure	$\text{J kg}^{-1} \text{K}^{-1}$
D	Temperature offset in R2D-fit	K
\vec{D}	Forcing term	m s^{-2}
d	Distance between Z and mountain peaks	m
d_r	Distance between rays and Río Grande	m
D_h	Half-day length	rad
E	Total GW energy per mass	J kg^{-1}
E_p	Gravity wave potential energy	J kg^{-1}
ΔE_p	Gravity wave potential energy uncertainty	J kg^{-1}
\mathbb{E}_p	Cumulative sum over E_p	J kg^{-1}
f	Coriolis parameter	s^{-1}
F	Temporal temperature rate	K s^{-1}
F_{Ph}	Vertical flux of horizontal pseudomomentum	J m^{-3}
G	Vertical temperature rate	K m^{-1}
g	Gravitational acceleration	m s^{-2}
H	Butterworth transfer function	
h	Bandwidth	
H_s	Density scale height	m
h_n	Equivalent depth	
I_g	Gini coefficient	
I_p	Laser pulse intensity	W m^{-2}
I_r	Received intensity	W m^{-2}

Sign	Description	Unit
J	Heating per unit mass	J kg^{-1}
K_h	Kernel	
K	Carrying capacity	J kg^{-1}
k	Zonal wave number	m^{-1}
k_h	Horizontal wave number	m^{-1}
k_B	Boltzmann constant	J K^{-1}
l	Meridional wave number	m^{-1}
L	Lower boundary	J kg^{-1}
M	Mean mass of one mol of the atmosphere	g mol^{-1}
m	vertical wave number	m^{-1}
minPts	Minimum number of points	
N	Brunt-Väisälä frequency	s^{-1}
n_d	Number density	m^{-3}
n_k	Refractive index	
n	Translation parameter	
n	Meridional index	
n_t	Number of grid points in time	
n_z	Number of grid points in altitude	
$O(r)$	Overlap function of the laser beam and the telescope's FOV	
o	Order of the Butterworth filter	
o_f	Forcing offset	s m^{-1}
o_T	T_{\max} offset	K
p	Pressure	Pa
p_s	Seeding pressure	Pa
P_0	Initial power of the laser pulse	W
P_r	Received power	W
Q	Forcing term	K s^{-1}
Q_s	Solar radiation	W m^{-2}
\bar{q}_ϕ	meridional gradient in potential vorticity	PVU m^{-1}
R	Universal gas constant	$\text{J mol}^{-1} \text{K}^{-1}$
R_λ	Radius of an ellipse in longitude direction	m
R_ϕ	Radius of an ellipse in latitude direction	m
R_e	Radius of an ellipse	m
\mathcal{R}_ϑ	Rotation matrix in 2D	
r	Distance between lidar and scattering molecule	m
r_f	Growth rate in forcing direction	s m^{-1}
r_T	Growth rate in T_{\max} direction	K^{-1}
s	Zonal wavenumber	

Sign	Description	Unit
t	Time	s
δt	Temporal resolution	s
Δt	Temporal window width	s
T	Temperature	K
T_0	Temperature background	K
\bar{T}	Climatological mean temperature	K
\tilde{T}	Large-scale temperature perturbations	K
T'	Temperature perturbations with vertical scales smaller than 15 km	K
T''	Temperature perturbations with vertical scales larger than 15 km	K
ΔT	Temperature uncertainty	K
T_{SO}	Temperature due to seasonal oscillations	K
T_{max}	Saturation amplitude	K
T_{PW}	Temperature perturbations due to PWs	K
T_{DT}	Temperature perturbations due to diurnal tides	K
u	Zonal wind	m s^{-1}
\vec{u}	Wind vector	m s^{-1}
\bar{u}	Zonal mean zonal wind	m s^{-1}
u'	Zonal wind perturbation amplitude	m s^{-1}
u_{h}	Horizontal wind	m s^{-1}
u_{f}	Forcing horizontal wind	m s^{-1}
u_{c}	Rossby critical velocity	m s^{-1}
v	Meridional wind	m s^{-1}
v'	Meridional wind perturbation amplitude	m s^{-1}
V	Illuminated volume of the laser pulse	m^3
w	Vertical wind	m s^{-1}
w'	Vertical wind perturbation amplitude	m s^{-1}
W	Spectral amplitudes	
$W_n(s)$	Wavelet transform	
\vec{x}	Position vector	m
Z	Center of idealized mountain ridge	
z	Altitude	m
δz	Vertical resolution	m
Δz	Vertical window width	m

Sign	Description	Unit
α_e	Extinction coefficient	
α_h	$\frac{1}{2H_s}$	m^{-1}
β	Backscatter coefficient	
Γ	Lidar system efficiency	
γ	Skewness	
δ	Solar declination	rad
ϵ	Ecliptic	rad
ε	Laplace's tidal equation eigenvalue	
ζ	Vertical displacement	m
η	Nondimensional time	
η	(System efficiency)	
θ	Transmission of the atmosphere	
ϑ	Orientation of the 2D Wavelet	rad
Θ	Cardinal direction	rad
Θ	Potential temperature	K
κ	$\frac{R}{c_p} \approx 2/7$	
λ	Longitude	$^\circ$
λ_{cut}	Cutoff wavelength	m
λ_h	Horizontal wavelength	m
λ_z	Vertical wavelength	m
μ	CWT scaling parameter	
ν	Angular frequency of PWs	s^{-1}
ξ	Phaseshift between winter solstice and the 1st of January	rad
ϱ	Density	kg m^{-3}
ϱ_0	Background density	kg m^{-3}
ϱ'	Density perturbation amplitude	kg m^{-3}
σ	Standard deviation	
σ	longitudinal wavenumber	
τ_{AO}	Phase of annual oscillation	s
τ_{DT}	Phase of diurnal tide	s
τ_{SAO}	Phase of semiannual oscillation	s
τ_L	Temporal pulse length	s
Υ	Divergence of the laser beam	rad
ν	Neighborhood radius in DBSCAN	
ϕ	Latitude	$^\circ$
Φ	Perturbation geopotential	J kg^{-1}
χ	Relative uncertainty of E_p	
Ψ_0	Mother wavelet function	
Ψ	Daughter wavelet function	
ω_0	Nondimensional frequency	
ω	Ground-based frequency	s^{-1}
$\hat{\omega}$	Intrinsic frequency	s^{-1}
Ω	Earth's angular frequency	s^{-1}
$\hat{\Omega}$	Earth's angular frequency around the sun	s^{-1}

Appendix A

CORAL's workflow

CORAL's workflow is as follows. In order to take one of the following actions, *start*, *remain on*, *stop* and *remain off*, a couple of parameters are requested (Fig. A.1). If the lidar is off, it will be switched on if the sun's elevation angle is below -7° and no rain or no strong wind is locally detected. To start and stop the lidar does not only mean switching the laser, detector, and data acquisition computer on and off, but also opening and closing the telescope hatch, which protects the sensitive telescope optics from rain. In addition, the lidar only starts operation if either the number of stars detected in all-sky images is large enough, i.e. the fraction of clouds in the night sky is small enough, or the forecasted cloud cover is less than 50% and accumulated precipitation over the next 2 h is less than 0.1 mm. Local high-resolution forecasts of the Integrated Forecast System (IFS) are automatically uploaded from the ECMWF. Once the lidar is switched on, it will remain on if the lidar return signal is larger than 70% of the maximum count rate, the sun's elevation angle is below -7° , and no rain or strong wind is locally detected. If the return signal is less than 70%, the lidar will also remain on if forecasted precipitation is < 0.1 mm. However, the lidar will stop if the return signal is less than 20% over the course of 15 min regardless of forecasted precipitation. The parameters as well as their thresholds are illustrated as a flowchart in Figure A.1. All the above listed decisions are taken by CORAL's software without the intervention of human operators.

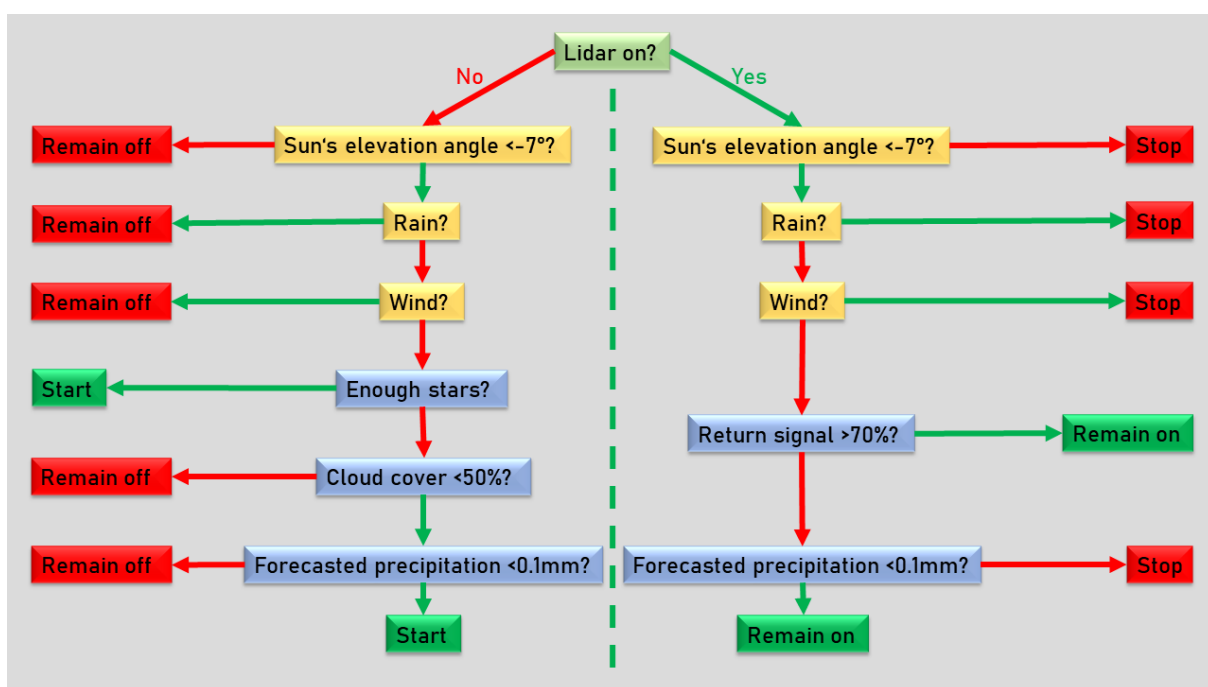


Figure A.1: Flowchart visualizes the start/stop decision algorithm of CORAL. Affirmation (negation) is indicated with a green (red) arrow.

Appendix B

Testing of WAVELET-SCAN with artificial temperature data

WAVELET-SCAN combines the CWT with DBSCAN in order to retrieve coherent wave packets from lidar temperature data. To validate its performance, WAVELET-SCAN is applied to a test case with artificial temperature data. The artificial wave field is composed of a stationary MW with a variable vertical wavelength and amplitude as well as one superimposed propagating wave:

$$\begin{aligned} T_{\text{art}}(t, z) = & \frac{A_{\text{sw}}}{1 - \exp\left(-\frac{z - z_{\text{sw}}}{2H_s}\right)} \sin\left(\int_0^z m_{\text{sw}}(\tilde{z}) d\tilde{z}\right) \\ & + A_{\text{pw}} \exp\left(-\frac{z - z_{\text{pw}}}{2\sigma_z^2} - \frac{t - t_{\text{pw}}}{2\sigma_t^2}\right) \cos(m_{\text{pw}}z - \omega_{\text{pw}}t) \\ & + \Delta T_{\text{art}} \end{aligned} \quad (\text{B.1})$$

with $A_{\text{sw}} = 20$ K, $z_{\text{sw}} = 30$ km, $H_s = 7.4$ km, $m_{\text{sw}}(z) = 2\pi/\lambda_{\text{sw}}(z)$, $A_{\text{pw}} = 8$ K, $z_{\text{pw}} = 60$ km, $t_{\text{pw}} = 15$ h, $m_{\text{pw}} = 2\pi/8$ km, $\omega_{\text{pw}} = 2\pi/3$ h, $\sigma_z = 10$ km, $\sigma_t = 5$ h, ΔT_{art} is random noise with a standard deviation of 1 K. The vertical wavelength of the stationary wave varies according to

$$\lambda_{\text{sw}}(z) = \begin{cases} 5 \text{ km} + 0.4z & \text{for } z \leq 50 \text{ km} \\ 35 \text{ km} - 0.2z & \text{for } z > 50 \text{ km.} \end{cases} \quad (\text{B.2})$$

Figure B.1 shows the artificial temperature perturbations, retrieved vertical wavelengths as well as the two wave packets separated by WAVELET-SCAN.

This validation demonstrates that WAVELET-SCAN is capable of separating superimposed wave packets very accurately. Although the modeled linear increase and decrease of λ_z seems correct, the exact values differ from the input. With $\omega_0 = 4$ the CWT has a good spectral resolution but on the cost of spatial resolution. Hence, if vertical wavelengths change rapidly with height, retrieved wavelengths must be seen as an average over an altitude range in the order of one vertical wavelength.

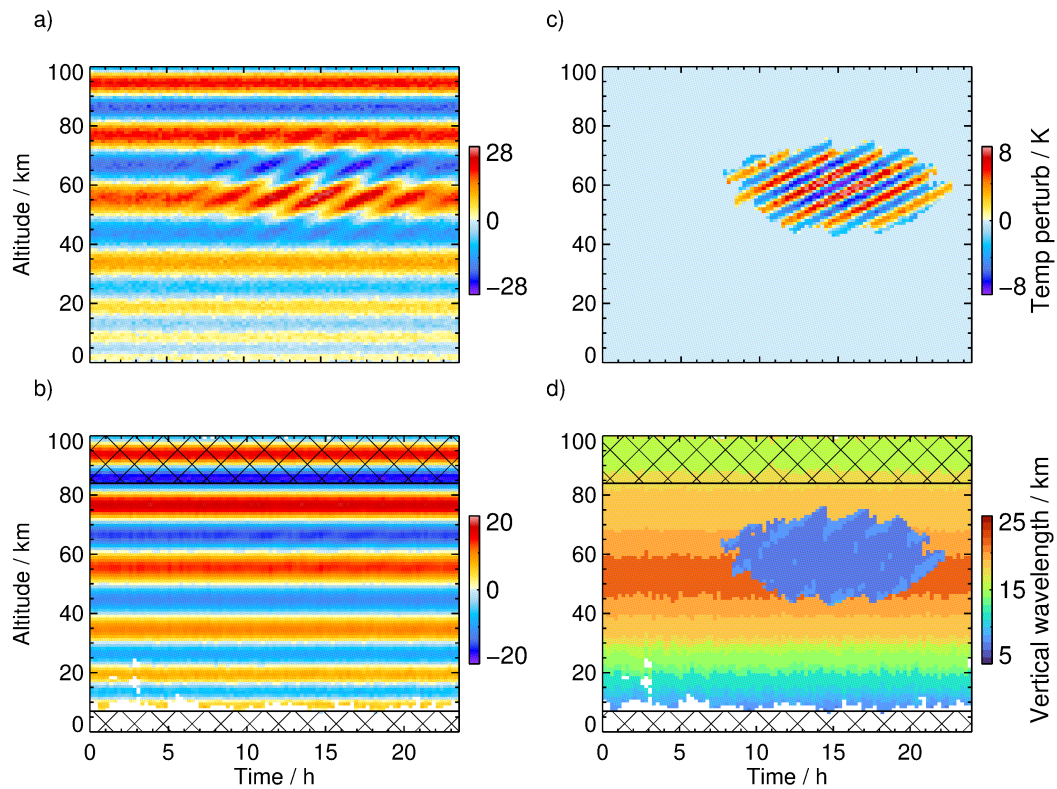


Figure B.1: Artificial temperature perturbations (a), reconstructed stationary wave (b), reconstructed propagating wave (c) and retrieved vertical wavelengths (d). Hatched areas mark the COI. This figure is reproduced from (Reichert et al., 2021).

Appendix C

Uncertainty calculations

To find out how the temperature error due to photon noise is distributed between the temperature perturbations and the temperature background, a Monte Carlo simulation is performed. It became apparent that about 1/9 of the temperature uncertainty introduced is reflected in the background and 8/9 in the disturbances. Therefore it is defined,

$$\Delta T' = \sqrt{\frac{8}{9}} \Delta T \quad \text{and} \quad (\text{C.1})$$

$$\Delta T_{\text{BG}} = \sqrt{\frac{1}{9}} \Delta T + \Delta \bar{T} \quad (\text{C.2})$$

where the additional term $\Delta \bar{T}$ accounts for the uncertainty due to the subtraction of seasonal oscillations. The uncertainty of the squared relative temperature perturbations is then given as

$$\Delta T'_r = \frac{2}{T_{\text{BG}}} \left(\frac{|T'|}{T_{\text{BG}}} \Delta T' + \frac{T'^2}{T_{\text{BG}}^2} \Delta T_{\text{BG}} \right). \quad (\text{C.3})$$

The uncertainty of the squared Brunt Väisälä frequency is given as

$$\Delta N^2 = \frac{\Delta T_{\text{BG}}}{T_{\text{BG}}} \left(N^2 + \frac{\sqrt{2}g}{\delta z} \right). \quad (\text{C.4})$$

Finally, the uncertainty of GW potential energy is defined as

$$\Delta E_p = E_p \frac{\Delta N^2}{N^2} + \frac{1}{2} \frac{g^2}{N^2} \overline{\Delta T'_r}, \quad (\text{C.5})$$

where the overbar denotes that $\Delta T'_r$ is averaged as in (4.20) and divided by $\sqrt{n_t n_z}$.

Bibliography

- M. J. Alexander. Interpretations of observed climatological patterns in stratospheric gravity wave variance. *Journal of Geophysical Research: Atmospheres*, 103(D8):8627–8640, 1998.
- M. J. Alexander and C. Barnet. Using Satellite Observations to Constrain Parameterizations of Gravity Wave Effects for Global Models. *Journal of the Atmospheric Sciences*, 64(5):1652–1665, 2007. doi: 10.1175/JAS3897.1. URL <https://doi.org/10.1175/JAS3897.1>.
- M. J. Alexander and L. Pfister. Gravity wave momentum flux in the lower stratosphere over convection. *Geophysical Research Letters*, 22(15):2029–2032, 1995.
- S. P. Alexander, T. Tsuda, and Y. Kawatani. COSMIC GPS observations of Northern Hemisphere winter stratospheric gravity waves and comparisons with an atmospheric general circulation model. *Geophysical research letters*, 35(10), 2008.
- S. P. Alexander, A. R. Klekociuk, and D. J. Murphy. Rayleigh lidar observations of gravity wave activity in the winter upper stratosphere and lower mesosphere above Davis, Antarctica (69° S, 78° E). *Journal of Geophysical Research: Atmospheres*, 116(D13), 2011. doi: 10.1029/2010JD015164. URL <https://agupubs.onlinelibrary.wiley.com/doi/abs/10.1029/2010JD015164>.
- S. P. Alexander, K. Sato, S. Watanabe, Y. Kawatani, and D. J. Murphy. Southern Hemisphere extratropical gravity wave sources and intermittency revealed by a middle-atmosphere general circulation model. *Journal of the Atmospheric Sciences*, 73(3): 1335–1349, 2016.
- J. T. Bacmeister, M. R. Schoeberl, L. R. Lait, P. A. Newman, and B. Gary. ER-2 mountain wave encounter over Antarctica: Evidence for blocking. *Geophysical research letters*, 17(1):81–84, 1990.
- P. Bauer, P. D. Dueben, T. Hoefler, T. Quintino, T. C. Schulthess, and N. P. Wedi. The digital revolution of Earth-system science. *Nature Computational Science*, 1(2): 104–113, 2021.
- A. J. G. Baumgaertner and A. J. McDonald. A gravity wave climatology for Antarctica compiled from Challenging Minisatellite Payload/Global Positioning System (CHAMP/GPS) radio occultations. *Journal of Geophysical Research: Atmospheres*, 112(D5), 2007.

- G. Baumgarten. Doppler Rayleigh/Mie/Raman lidar for wind and temperature measurements in the middle atmosphere up to 80 km. *Atmospheric Measurement Techniques*, 3(6):1509–1518, 2010.
- K. Baumgarten and G. Stober. On the evaluation of the phase relation between temperature and wind tides based on ground-based measurements and reanalysis data in the middle atmosphere. In *Annales geophysicae*, volume 37, pages 581–602. Copernicus GmbH, 2019.
- K. Baumgarten, M. Gerding, and F.-J. Lübken. Seasonal variation of gravity wave parameters using different filter methods with daylight lidar measurements at midlatitudes. *Journal of Geophysical Research: Atmospheres*, 122(5):2683–2695, 2017.
- A. Behrendt. Temperature measurements with lidar. In *Lidar*, pages 273–305. Springer, 2005.
- M. Bramberger, A. Dörnbrack, K. Bossert, B. Ehard, D. C. Fritts, B. Kaifler, C. Mallaun, A. Orr, P.-D. Pautet, M. Rapp, et al. Does strong tropospheric forcing cause large-amplitude mesospheric gravity waves? A DEEPWAVE case study. *Journal of Geophysical Research: Atmospheres*, 122(21):11–422, 2017.
- G. P. Brasseur and S. Solomon. *Aeronomy of the middle atmosphere: Chemistry and physics of the stratosphere and mesosphere*, volume 32. Springer Science & Business Media, 2006.
- O. Bühler. *Waves and mean flows*. Cambridge University Press, 2014.
- O. Bühler and M. E. McIntyre. On shear-generated gravity waves that reach the mesosphere. Part II: Wave propagation. *Journal of the atmospheric sciences*, 56(21):3764–3773, 1999.
- O. Bühler, M. E. McIntyre, and J. F. Scinocca. On shear-generated gravity waves that reach the mesosphere. Part I: Wave generation. *Journal of the atmospheric sciences*, 56(21):3749–3763, 1999.
- N. Butchart, A. J. Charlton-Perez, I. Cionni, S. C. Hardiman, P. H. Haynes, K. Krüger, P. J. Kushner, P. A. Newman, S. M. Osprey, J. Perlwitz, et al. Multimodel climate and variability of the stratosphere. *Journal of Geophysical Research: Atmospheres*, 116(D5), 2011.
- S. Butterworth et al. On the theory of filter amplifiers. *Wireless Engineer*, 7(6):536–541, 1930.
- S. Chapman and R. Lindzen. Atmospheric tides. Thermal and gravitational. *Dordrecht: Reidel*, 1970.
- J. G. Charney and P. G. Drazin. Propagation of planetary-scale disturbances from the lower into the upper atmosphere. *Journal of Geophysical Research*, 66(1):83–109, 1961.

- C. Chen and X. Chu. Two-dimensional Morlet wavelet transform and its application to wave recognition methodology of automatically extracting two-dimensional wave packets from lidar observations in Antarctica. *Journal of Atmospheric and Solar-Terrestrial Physics*, 162:28–47, 2017.
- X. Chu, J. Zhao, X. Lu, V. L. Harvey, R. M. Jones, E. Becker, C. Chen, W. Fong, Z. Yu, B. R. Roberts, et al. Lidar observations of stratospheric gravity waves from 2011 to 2015 at McMurdo (77.84° S, 166.69° E), Antarctica: 2. potential energy densities, lognormal distributions, and seasonal variations. *Journal of Geophysical Research: Atmospheres*, 123(15):7910–7934, 2018.
- R. T. H. Collis. Lidar observation of cloud. *Science*, 149(3687):978–981, 1965.
- J. F. Conte, J. L. Chau, G. Stober, N. Pedatella, A. Maute, P. Hoffmann, D. Janches, D. C. Fritts, and D. J. Murphy. Climatology of semidiurnal lunar and solar tides at middle and high latitudes: Interhemispheric comparison. *Journal of Geophysical Research: Space Physics*, 122(7):7750–7760, 2017.
- J. Daintith. *A Dictionary of Physics* - . OUP Oxford, New York, London, 2009. ISBN 978-0-199-23399-1.
- E. M. Dewan, R. H. Picard, R. R. O’Neil, H. A. Gardiner, J. Gibson, J. D. Mill, E. Richards, M. Kendra, and W. O. Gallery. MSX satellite observations of thunderstorm-generated gravity waves in mid-wave infrared images of the upper stratosphere. *Geophysical Research Letters*, 25(7):939–942, 1998.
- A. Dörnbrack. Stratospheric mountain waves trailing across northern Europe. *Journal of the Atmospheric Sciences*, 78(9):2835–2857, 2021.
- A. Dörnbrack and C. J. Nappo. A note on the application of linear wave theory at a critical level. *Boundary-Layer Meteorology*, 82(3):399–416, 1997.
- A. Dörnbrack, M. Leutbecher, R. Kivi, and E. Kyrö. Mountain-wave-induced record low stratospheric temperatures above northern Scandinavia. *Tellus A: Dynamic Meteorology and Oceanography*, 51(5):951–963, 1999.
- A. Dörnbrack, S. Gisinger, and B. Kaifler. On the interpretation of gravity wave measurements by ground-based lidars. *Atmosphere*, 8(3):49, 2017.
- A. Dörnbrack, S. Gisinger, N. Kaifler, T. C. Portele, M. Bramberger, M. Rapp, M. Gerdling, J. Söder, N. Žagar, and D. Jelić. Gravity waves excited during a minor sudden stratospheric warming. *Atmospheric Chemistry and Physics*, 18(17):12915–12931, 2018. doi: 10.5194/acp-18-12915-2018. URL <https://www.atmos-chem-phys.net/18/12915/2018/>.
- A. Dörnbrack, B. Kaifler, N. Kaifler, M. Rapp, N. Wildmann, M. Garhammer, K. Ohlmann, J. M. Payne, M. Sandercock, and E. J. Austin. Unusual appearance of mother-of-pearl clouds above El Calafate, Argentina (50° 21’ S, 72° 16’ W). *Weather*, 75(12):378–388, 2020.

- T. J. Duck, D. P. Sipler, J. E. Salah, and J. W. Meriwether. Rayleigh lidar observations of a mesospheric inversion layer during night and day. *Geophysical research letters*, 28(18):3597–3600, 2001.
- T. Dunkerton. On the mean meridional mass motions of the stratosphere and mesosphere. *Journal of Atmospheric Sciences*, 35(12):2325–2333, 1978.
- T. J. Dunkerton. Wave transience in a compressible atmosphere. Part III: the saturation of internal gravity waves in the mesosphere. *Journal of the Atmospheric Sciences*, 39(5):1042–1051, 1982.
- T. J. Dunkerton. Inertia–gravity waves in the stratosphere. *Journal of the atmospheric sciences*, 41(23):3396–3404, 1984.
- S. D. Eckermann. Ray-tracing simulation of the global propagation of inertia gravity waves through the zonally averaged middle atmosphere. *Journal of Geophysical Research: Atmospheres*, 97(D14):15849–15866, 1992.
- S. D. Eckermann and C. J. Marks. An idealized ray model of gravity wave-tidal interactions. *Journal of Geophysical Research: Atmospheres*, 101(D16):21195–21212, 1996.
- S. D. Eckermann and P. Preusse. Global measurements of stratospheric mountain waves from space. *Science*, 286(5444):1534–1537, 1999.
- B. Ehard, B. Kaifler, N. Kaifler, and M. Rapp. Evaluation of methods for gravity wave extraction from middle-atmospheric lidar temperature measurements. *Atmospheric Measurement Techniques*, 8(11):4645–4655, 2015. doi: 10.5194/amt-8-4645-2015. URL <http://www.atmos-meas-tech.net/8/4645/2015/>.
- B. Ehard, B. Kaifler, A. Dörnbrack, P. Preusse, S. D. Eckermann, M. Bramberger, S. Gisinger, N. Kaifler, B. Liley, J. Wagner, et al. Horizontal propagation of large-amplitude mountain waves into the polar night jet. *Journal of Geophysical Research: Atmospheres*, 122(3):1423–1436, 2017.
- M. Ern, P. Preusse, M. J. Alexander, and C. D. Warner. Absolute values of gravity wave momentum flux derived from satellite data. *Journal of Geophysical Research: Atmospheres*, 109(D20), 2004.
- M. Ern, P. Preusse, J. C. Gille, C. L. Hepplewhite, M. G. Mlynczak, J. M. Russell III, and M. Riese. Implications for atmospheric dynamics derived from global observations of gravity wave momentum flux in stratosphere and mesosphere. *Journal of Geophysical Research: Atmospheres*, 116(D19), 2011.
- M. Ester, H.-P. Kriegel, J. Sander, X. Xu, et al. A density-based algorithm for discovering clusters in large spatial databases with noise. In *Kdd*, volume 96, pages 226–231, 1996.
- M. Farge. Wavelet transforms and their applications to turbulence. *Annual review of fluid mechanics*, 24(1):395–458, 1992.

- D. R. Feldman, W. D. Collins, P. J. Gero, M. S. Torn, E. J. Mlawer, and T. R. Shippert. Observational determination of surface radiative forcing by CO₂ from 2000 to 2010. *Nature*, 519(7543):339–343, 2015.
- E. L. Fleming, S. Chandra, J. J. Barnett, and M. Corney. Zonal mean temperature, pressure, zonal wind and geopotential height as functions of latitude. *Advances in Space Research*, 10(12):11–59, 1990.
- B. Fogle and B. Haurwitz. Noctilucent clouds. *Space Science Reviews*, 6(3):279–340, 1966.
- J. M. Forbes et al. Tidal and planetary waves. *The Upper Mesosphere and Lower Thermosphere: A Review of Experiment and Theory, Geophys. Monogr. Ser.*, 87:67–87, 1995.
- D. C. Fritts and M. J. Alexander. Gravity wave dynamics and effects in the middle atmosphere. *Reviews of geophysics*, 41(1), 2003.
- D. C. Fritts and Z. Luo. Gravity wave excitation by geostrophic adjustment of the jet stream. Part I: Two-dimensional forcing. *Journal of the Atmospheric Sciences*, 49(8): 681–697, 1992.
- D. C. Fritts, R. B. Smith, M. J. Taylor, J. D. Doyle, S. D. Eckermann, A. Dörnbrack, M. Rapp, B. P. Williams, P.-D. Pautet, K. Bossert, et al. The Deep Propagating Gravity Wave Experiment (DEEPWAVE): An airborne and ground-based exploration of gravity wave propagation and effects from their sources throughout the lower and middle atmosphere. *Bulletin of the American Meteorological Society*, 97(3):425–453, 2016.
- X.-H. Gao, W.-B. Yu, and J. L. Stanford. Global features of the semiannual oscillation in stratospheric temperatures and comparison between seasons and hemispheres. *Journal of Atmospheric Sciences*, 44(7):1041–1048, 1987.
- C. S. Gardner and M. J. Taylor. Observational limits for lidar, radar, and airglow imager measurements of gravity wave parameters. *Journal of Geophysical Research: Atmospheres*, 103(D6):6427–6437, 1998.
- M. Geldenhuys, M. Ern, P. Preusse, F. Friedl-Vallon, J. Ungermann, M. Riese, C. Zülicke, I. Krisch, and I. Polichtchouk. A new mechanism for spontaneous imbalance exciting large-area gravity waves. *43rd COSPAR Scientific Assembly. Held 28 January-4 February*, 43:721, 2021.
- E. P. Gerber, P. Martineau, B. Ayarzagüena, D. Barriopedro, T. J. Bracegirdle, A. H. Butler, N. Calvo, S. C. Hardiman, P. Hitchcock, M. Iza, et al. Extratropical stratosphere-troposphere coupling. *Stratosphere-troposphere processes and their role in climate (SPARC) reanalysis intercomparison project (S-RIP)*, edited by: Fujiwara, M., Manney, GL, Gray, L., and Wright, JS, 2021.
- M. Gerding, J. Höffner, J. Lautenbach, M. Rauthe, and F.-J. Lübken. Seasonal variation of nocturnal temperatures between 1 and 105 km altitude at 54° N observed by lidar. *Atmospheric Chemistry and Physics*, 8(24):7465–7482, 2008.

- A. E. Gill. *Atmosphere-Ocean Dynamics*. Academic Press, 1982.
- S. Gisinger, I. Polichtchouk, A. Dörnbrack, R. Reichert, B. Kaifler, N. Kaifler, M. Rapp, and I. Sandu. Gravity-Wave-Driven Seasonal Variability of Temperature Differences between ECMWF IFS and Rayleigh Lidar Measurements in the Lee of the Southern Andes. *Earth and Space Science Open Archive*, page 34, 2021. doi: 10.1002/essoar.10508969.1. URL <https://doi.org/10.1002/essoar.10508969.1>.
- A. Gupta, T. Birner, A. Dörnbrack, and I. Polichtchouk. Importance of gravity wave forcing for springtime southern polar vortex breakdown as revealed by ERA5. *Geophysical Research Letters*, 48(10):e2021GL092762, 2021.
- J. E. Harries, H. E. Brindley, P. J. Sagoo, and R. J. Bantges. Increases in greenhouse forcing inferred from the outgoing longwave radiation spectra of the Earth in 1970 and 1997. *Nature*, 410(6826):355–357, 2001.
- A. Hauchecorne and M.-L. Chanin. Density and temperature profiles obtained by lidar between 35 and 70 km. *Geophysical Research Letters*, 7(8):565–568, 1980. ISSN 1944-8007. doi: 10.1029/GL007i008p00565. URL <http://dx.doi.org/10.1029/GL007i008p00565>.
- A. Hauchecorne and M.-L. Chanin. Mid-latitude Lidar observations of planetary waves in the middle atmosphere during the winter of 1981–1982. *Journal of Geophysical Research: Oceans*, 88(C6):3843–3849, 1983.
- C. J. Heale, K. Bossert, S. L. Vadas, L. Hoffmann, A. Dörnbrack, G. Stober, J. B. Snively, and C. Jacobi. Secondary Gravity Waves Generated by Breaking Mountain Waves Over Europe. *Journal of Geophysical Research: Atmospheres*, 125(5):e2019JD031662, 2020.
- J. H. Hecht, D. C. Fritts, L. Wang, L. J. Gelinias, R. J. Rudy, R. L. Walterscheid, M. J. Taylor, P.-D. Pautet, S. Smith, and S. J. Franke. Observations of the breakdown of mountain waves over the Andes Lidar Observatory at Cerro Pachon on 8/9 July 2012. *Journal of Geophysical Research: Atmospheres*, 123(1):276–299, 2018.
- A. Hertzog, M. J. Alexander, and R. Plougonven. On the intermittency of gravity wave momentum flux in the stratosphere. *Journal of the Atmospheric Sciences*, 69(11):3433–3448, 2012.
- M. O. G. Hills and D. R. Durran. Nonstationary trapped lee waves generated by the passage of an isolated jet. *Journal of the atmospheric sciences*, 69(10):3040–3059, 2012.
- N. P. Hindley, C. J. Wright, N. D. Smith, and N. J. Mitchell. The southern stratospheric gravity wave hot spot: individual waves and their momentum fluxes measured by COSMIC GPS-RO. *Atmospheric Chemistry & Physics*, 15(14), 2015.
- N. P. Hindley, C. J. Wright, L. Hoffmann, T. Moffat-Griffin, and N. J. Mitchell. An 18-year climatology of directional stratospheric gravity wave momentum flux from 3-D satellite observations. *Geophysical Research Letters*, page e2020GL089557, 2020.

- I. Hirota, T. Hirooka, and M. Shiotani. Upper stratospheric circulations in the two hemispheres observed by satellites. *Quarterly Journal of the Royal Meteorological Society*, 109(461):443–454, 1983.
- L. Hoffmann, X. Xue, and M. J. Alexander. A global view of stratospheric gravity wave hotspots located with Atmospheric Infrared Sounder observations. *Journal of Geophysical Research: Atmospheres*, 118(2):416–434, 2013.
- P. Hoffmann, E. Becker, W. Singer, and M. Placke. Seasonal variation of mesospheric waves at northern middle and high latitudes. *Journal of Atmospheric and Solar-Terrestrial Physics*, 72(14-15):1068–1079, 2010.
- J. R. Holton. *An introduction to dynamic meteorology*. International Geophysics Series. Elsevier Academic Press, Burlington, MA, 4 edition, 2004. ISBN 9780123540157. URL <http://books.google.com/books?id=fhW5oDv3EPsC>.
- N. E. Huang, Z. Wu, S. R. Long, K. C. Arnold, X. Chen, and K. Blank. On instantaneous frequency. *Advances in adaptive data analysis*, 1(02):177–229, 2009.
- E. O. Hulburt. Observations of a searchlight beam to an altitude of 28 kilometers. *JOSA*, 27(11):377–382, 1937.
- J. H. Jiang, D. L. Wu, S. D. Eckermann, and J. Ma. Mountain waves in the middle atmosphere: Microwave limb sounder observations and analyses. *Advances in Space Research*, 32(5):801–806, 2003.
- Q. Jiang, J. D. Doyle, A. Reinecke, R. B. Smith, and S. D. Eckermann. A modeling study of stratospheric waves over the Southern Andes and Drake Passage. *Journal of the atmospheric sciences*, 70(6):1668–1689, 2013.
- Q. Jiang, J. D. Doyle, S. D. Eckermann, and B. P. Williams. Stratospheric trailing gravity waves from New Zealand. *Journal of the Atmospheric Sciences*, 76(6):1565–1586, 2019.
- W. L. Jones. Propagation of internal gravity waves in fluids with shear flow and rotation. *Journal of Fluid Mechanics*, 30(3):439–448, 1967.
- B. Kaifler and N. Kaifler. A Compact Rayleigh Autonomous Lidar (CORAL) for the middle atmosphere. *Atmospheric Measurement Techniques Discussions*, 2020:1–24, 2020. doi: 10.5194/amt-2020-418. URL <https://amt.copernicus.org/preprints/amt-2020-418/>.
- B. Kaifler, N. Kaifler, B. Ehard, A. Dörnbrack, M. Rapp, and D. C. Fritts. Influences of source conditions on mountain wave penetration into the stratosphere and mesosphere. *Geophysical Research Letters*, 42(21):9488–9494, 2015a.
- B. Kaifler, F.-J. Lübken, J. Höffner, R. J. Morris, and T. P. Viehl. Lidar observations of gravity wave activity in the middle atmosphere over Davis (69° S, 78° E), Antarctica. *Journal of Geophysical Research: Atmospheres*, 120(10):4506–4521, 2015b. doi: 10.1002/2014JD022879. URL <https://agupubs.onlinelibrary.wiley.com/doi/abs/10.1002/2014JD022879>.

- B. Kaifler, D. Rempel, P. Roßi, C. Büdenbender, N. Kaifler, and V. Baturkin. A technical description of the Balloon Lidar Experiment (BOLIDE). *Atmospheric Measurement Techniques*, 13(10):5681–5695, 2020a.
- N. Kaifler, B. Kaifler, B. Ehard, S. Gisinger, A. Dörnbrack, M. Rapp, R. Kivi, A. Kozlovsky, M. Lester, and B. Liley. Observational indications of downward-propagating gravity waves in middle atmosphere lidar data. *Journal of Atmospheric and Solar-Terrestrial Physics*, March 2017. URL <http://elib.dlr.de/111473/>.
- N. Kaifler, B. Kaifler, H. Wilms, M. Rapp, G. Stober, and C. Jacobi. Mesospheric temperature during the extreme mid-latitude noctilucent cloud event on 18/19 July 2016. *Journal of Geophysical Research: Atmospheres*, 0(ja), 2018. doi: 10.1029/2018JD029717. URL <https://agupubs.onlinelibrary.wiley.com/doi/abs/10.1029/2018JD029717>.
- N. Kaifler, B. Kaifler, A. Dörnbrack, M. Rapp, J. L. Hormaechea, and A. de la Torre. Lidar observations of large-amplitude mountain waves in the stratosphere above Tierra del Fuego, Argentina. *Scientific Reports*, 10(1):1–10, 2020b.
- S. Kalisch, P. Preusse, M. Ern, S. D. Eckermann, and M. Riese. Differences in gravity wave drag between realistic oblique and assumed vertical propagation. *Journal of Geophysical Research: Atmospheres*, 119(17):10–081, 2014.
- A. Kasahara. Normal modes of ultralong waves in the atmosphere. *Monthly Weather Review*, 104(6):669–690, 1976.
- R. Kivi, A. Dörnbrack, M. Sprenger, and H. Vömel. Far-Ranging Impact of Mountain Waves Excited Over Greenland on Stratospheric Dehydration and Rehydration. *Journal of Geophysical Research: Atmospheres*, 125(18):e2020JD033055, 2020.
- M. Kogure, J. Yue, T. Nakamura, L. Hoffmann, S. L. Vadas, Y. Tomikawa, M. K. Ejiri, and D. Janches. First Direct Observational Evidence for Secondary Gravity Waves Generated by Mountain Waves Over the Andes. *Geophysical Research Letters*, 47(17):e2020GL088845, 2020.
- M. Kopp, M. Gerding, J. Höffner, and F.-J. Lübken. Tidal signatures in temperatures derived from daylight lidar soundings above Kühlungsborn (54° N, 12° E). *Journal of Atmospheric and Solar-Terrestrial Physics*, 127:37–50, 2015.
- M. Krebsbach and P. Preusse. Spectral analysis of gravity wave activity in SABER temperature data. *Geophysical research letters*, 34(3), 2007.
- C. G. Kruse, R. B. Smith, and S. D. Eckermann. The Midlatitude Lower-Stratospheric Mountain Wave “Valve Layer”. *Journal of the Atmospheric Sciences*, 73(12):5081–5100, 2016.
- Q. Li, H.-F. Graf, and M. A. Giorgetta. Stationary planetary wave propagation in Northern Hemisphere winter-climatological analysis of the refractive index. *Atmospheric Chemistry and Physics*, 7(1):183–200, 2007.

- J. Lighthill. Waves in fluids. *Cambridge*, 1978.
- R. S. Lindzen. Turbulence and stress owing to gravity wave and tidal breakdown. *Journal of Geophysical Research: Oceans*, 86(C10):9707–9714, 1981.
- H.-L. Liu. Quantifying gravity wave forcing using scale invariance. *Nature communications*, 10(1):1–12, 2019.
- P. Llamedo, J. Salvador, A. de la Torre, J. Quiroga, P. Alexander, R. Hierro, T. Schmidt, A. Pazmino, and E. Quel. 11 Years of Rayleigh Lidar Observations of Gravity Wave Activity Above the Southern Tip of South America. *Journal of Geophysical Research: Atmospheres*, 124(2):451–467, 2019.
- F.-J. Lübken. Seasonal variation of turbulent energy dissipation rates at high latitudes as determined by in situ measurements of neutral density fluctuations. *Journal of Geophysical Research: Atmospheres*, 102(D12):13441–13456, 1997.
- F.-J. Lübken. Thermal structure of the Arctic summer mesosphere. *Journal of Geophysical Research: Atmospheres*, 104(D8):9135–9149, 1999. ISSN 2156-2202. doi: 10.1029/1999JD900076. URL <http://dx.doi.org/10.1029/1999JD900076>.
- F.-J. Lübken, K.-H. Fricke, and M. Langer. Noctilucent clouds and the thermal structure near the Arctic mesopause in summer. *Journal of Geophysical Research: Atmospheres*, 101(D5):9489–9508, 1996.
- F.-J. Lübken, J. Höffner, T. P. Viehl, B. Kaifler, and R. J. Morris. First measurements of thermal tides in the summer mesopause region at Antarctic latitudes. *Geophysical research letters*, 38(24), 2011.
- C. J. Marks and S. D. Eckermann. A Three-Dimensional Nonhydrostatic Ray-Tracing Model for Gravity Waves: Formulation and Preliminary Results for the Middle Atmosphere. *Journal of the Atmospheric Sciences*, 52(11):1959–1984, 1995. doi: 10.1175/1520-0469(1995)052<1959:ATDNRT>2.0.CO;2. URL [https://doi.org/10.1175/1520-0469\(1995\)052<1959:ATDNRT>2.0.CO;2](https://doi.org/10.1175/1520-0469(1995)052<1959:ATDNRT>2.0.CO;2).
- C. McLandress, T. G. Shepherd, S. Polavarapu, and S. R. Beagley. Is missing orographic gravity wave drag near 60° S the cause of the stratospheric zonal wind biases in chemistry–climate models? *Journal of the Atmospheric Sciences*, 69(3):802–818, 2012.
- Y. Minamihara, K. Sato, and M. Tsutsumi. Intermittency of gravity waves in the Antarctic troposphere and lower stratosphere revealed by the PANSY radar observation. *Journal of Geophysical Research: Atmospheres*, 125(15):e2020JD032543, 2020.
- T. Mixa, A. Dörnbrack, and M. Rapp. Nonlinear Simulations of Gravity Wave Tunneling and Breaking over Auckland Island. *Journal of the Atmospheric Sciences*, 78(5):1567–1582, 2021.
- N. Mzé, A. Hauchecorne, P. Keckhut, and M. Thétis. Vertical distribution of gravity wave potential energy from long-term Rayleigh lidar data at a northern middle-latitude site.

- Journal of Geophysical Research: Atmospheres*, 119(21):12,069–12,083, 2014. doi: 10.1002/2014JD022035. URL <https://agupubs.onlinelibrary.wiley.com/doi/abs/10.1002/2014JD022035>.
- C. J. Nappo. *An Introduction to Atmospheric Gravity Waves*. Number Bd. 1 in An Introduction to Atmospheric Gravity Waves. Academic Press, 2002. ISBN 9780125140829. URL <https://books.google.de/books?id=I6KDVUU3myoC>.
- G. D. Nastrom and D. C. Fritts. Sources of mesoscale variability of gravity waves. Part I: Topographic excitation. *Journal of Atmospheric Sciences*, 49(2):101–110, 1992.
- K. Ohneiser, A. Ansmann, H. Baars, P. Seifert, B. Barja, C. Jimenez, M. Radenz, A. Teisseire, A. Floutsi, M. Haarig, et al. Smoke of extreme Australian bushfires observed in the stratosphere over Punta Arenas, Chile, in January 2020: optical thickness, lidar ratios, and depolarization ratios at 355 and 532 nm. *Atmospheric Chemistry and Physics*, 20(13):8003–8015, 2020.
- T. Palmer and B. Stevens. The scientific challenge of understanding and estimating climate change. *Proceedings of the National Academy of Sciences*, 116(49):24390–24395, 2019.
- D. Pancheva and P. Mukhtarov. Atmospheric tides and planetary waves: recent progress based on SABER/TIMED temperature measurements (2002–2007). In *Aeronomy of the Earth's Atmosphere and Ionosphere*, pages 19–56. Springer, 2011.
- E. Parzen. On Estimation of a Probability Density Function and Mode. *The Annals of Mathematical Statistics*, 33(3):1065–1076, 1962. ISSN 00034851. URL <http://www.jstor.org/stable/2237880>.
- P.-D. Pautet, M. J. Taylor, W. R. Pendleton, Y. Zhao, T. Yuan, R. Esplin, and D. McLain. Advanced mesospheric temperature mapper for high-latitude airglow studies. *Appl. Opt.*, 53(26):5934–5943, Sep 2014. doi: 10.1364/AO.53.005934. URL <http://ao.osa.org/abstract.cfm?URI=ao-53-26-5934>.
- P.-D. Pautet, M. J. Taylor, D. C. Fritts, D. Janches, N. Kaifler, A. Dörnbrack, and J. L. Hormaechea. Mesospheric Mountain Wave Activity in the Lee of the Southern Andes. *Journal of Geophysical Research: Atmospheres*, 126(7):e2020JD033268, 2021.
- R. Plougonven, A. Hertzog, and L. Guez. Gravity waves over Antarctica and the Southern Ocean: Consistent momentum fluxes in mesoscale simulations and stratospheric balloon observations. *Quarterly Journal of the Royal Meteorological Society*, 139(670):101–118, 2013.
- R. A. Plumb. Planetary waves and the extratropical winter stratosphere. *The Stratosphere, Dynamics, Transport and Chemistry, Geophys. Monogr.*, 190:23–41, 2010.
- T. C. Portele, A. Dörnbrack, J. S. Wagner, S. Gisinger, B. Ehard, P.-D. Pautet, and M. Rapp. Mountain-wave propagation under transient tropospheric forcing: A DEEP-WAVE case study. *Monthly Weather Review*, 146(6):1861–1888, 2018.

- P. Preusse, S. Eckermann, J. Oberheide, M. Hagan, and D. Offermann. Modulation of gravity waves by tides as seen in CRISTA temperatures. *Advances in Space Research*, 27(10):1773–1778, 2001.
- P. Preusse, A. Dörnbrack, S. D. Eckermann, M. Riese, B. Schaeler, J. T. Bacmeister, D. Broutman, and K. U. Grossmann. Space-based measurements of stratospheric mountain waves by CRISTA 1. Sensitivity, analysis method, and a case study. *Journal of Geophysical Research: Atmospheres*, 107(D23):CRI–6, 2002.
- P. Preusse, S. D. Eckermann, and M. Ern. Transparency of the atmosphere to short horizontal wavelength gravity waves. *Journal of Geophysical Research: Atmospheres*, 113(D24), 2008.
- P. Preusse, S. D. Eckermann, M. Ern, J. Oberheide, R. H. Picard, R. G. Roble, M. Riese, J. M. Russell III, and M. G. Mlynczak. Global ray tracing simulations of the SABER gravity wave climatology. *Journal of Geophysical Research: Atmospheres*, 114(D8), 2009.
- P. Preusse, M. Ern, P. Bechtold, S. D. Eckermann, S. Kalisch, Q. T. Trinh, and M. Riese. Characteristics of gravity waves resolved by ECMWF. *Atmos. Chem. Phys*, 14(10):483–10, 2014.
- J. M. Prusa, P. K. Smolarkiewicz, and A. A. Wyszogrodzki. EULAG, a computational model for multiscale flows. *Computers & Fluids*, 37(9):1193–1207, 2008.
- P. Queney. The problem of air flow over mountains: A summary of theoretical studies. *Bulletin of the American Meteorological Society*, 29(1):16–26, 1948.
- P. Queney. Transfer and dissipation of energy by mountain waves. In *Dynamic meteorology*, pages 513–617. Springer, 1973.
- W. J. Randel. The seasonal evolution of planetary waves in the Southern Hemisphere stratosphere and troposphere. *Quarterly Journal of the Royal Meteorological Society*, 114(484):1385–1409, 1988.
- M. Rapp, J. Gumbel, and F.-J. Lübken. Absolute density measurements in the middle atmosphere. In *Annales Geophysicae*, volume 19, pages 571–580. Copernicus GmbH, 2001.
- M. Rapp, A. Dörnbrack, and B. Kaifler. An intercomparison of stratospheric gravity wave potential energy densities from METOP GPS radio occultation measurements and ECMWF model data. *Atmospheric Measurement Techniques*, 11(2):1031, 2018a.
- M. Rapp, A. Dörnbrack, and P. Preusse. Large midlatitude stratospheric temperature variability caused by inertial instability: A potential source of bias for gravity wave climatologies. *Geophysical research letters*, 45(19):10–682, 2018b.
- M. Rapp, B. Kaifler, A. Dörnbrack, S. Gisinger, T. Mixa, R. Reichert, N. Kaifler, S. Knobloch, R. Eckert, N. Wildmann, et al. SOUTHTRAC-GW: An airborne field

- campaign to explore gravity wave dynamics at the world's strongest hotspot. *Bulletin of the American Meteorological Society*, 102(4):E871–E893, 2021.
- M. Rauthe, M. Gerding, J. Höffner, and F.-J. Lübken. Lidar temperature measurements of gravity waves over Kühlungsborn (54° N) from 1 to 105 km: A winter-summer comparison. *Journal of Geophysical Research: Atmospheres*, 111(D24), 2006.
- M. Rauthe, M. Gerding, and F.-J. Lübken. Seasonal changes in gravity wave activity measured by lidars at mid-latitudes. *Atmospheric Chemistry and Physics*, 8(22):6775–6787, 2008.
- R. Reichert, B. Kaifler, N. Kaifler, M. Rapp, P.-D. Pautet, M. J. Taylor, A. Kozlovsky, M. Lester, and R. Kivi. Retrieval of intrinsic mesospheric gravity wave parameters using lidar and airglow temperature and meteor radar wind data. *Atmospheric Measurement Techniques*, 12(11):5997–6015, 2019.
- R. Reichert, B. Kaifler, N. Kaifler, A. Dörnbrack, M. Rapp, and J. L. Hormaechea. High-Cadence Lidar Observations of Middle Atmospheric Temperature and Gravity Waves at the Southern Andes Hot Spot. *Journal of Geophysical Research: Atmospheres*, page e2021JD034683, 2021.
- O. Reitebuch, C. Lemmerz, E. Nagel, U. Paffrath, Y. Durand, M. Endemann, F. Fabre, and M. Chaloupy. The airborne demonstrator for the direct-detection Doppler wind lidar ALADIN on ADM-Aeolus. Part I: Instrument design and comparison to satellite instrument. *Journal of Atmospheric and Oceanic Technology*, 26(12):2501–2515, 2009.
- E. E. Remsberg, P. P. Bhatt, and L. E. Deaver. Seasonal and longer-term variations in middle atmosphere temperature from HALOE on UARS. *Journal of Geophysical Research: Atmospheres*, 107(D19):ACL–18, 2002.
- M. Rosenblatt. Remarks on Some Nonparametric Estimates of a Density Function. *The Annals of Mathematical Statistics*, 27(3):832–837, 1956. ISSN 00034851. URL <http://www.jstor.org/stable/2237390>.
- T. Sakazaki, M. Fujiwara, and M. Shiotani. Representation of solar tides in the stratosphere and lower mesosphere in state-of-the-art reanalyses and in satellite observations. *Atmospheric Chemistry and Physics*, 18(2):1437–1456, 2018.
- K. Sato. Small-scale wind disturbances observed by the MU radar during the passage of Typhoon Kelly. *Journal of the Atmospheric Sciences*, 50(4):518–537, 1993.
- K. Sato, S. Watanabe, Y. Kawatani, Y. Tomikawa, K. Miyazaki, and M. Takahashi. On the origins of mesospheric gravity waves. *Geophysical Research Letters*, 36(19), 2009.
- K. Sato, S. Tateno, S. Watanabe, and Y. Kawatani. Gravity wave characteristics in the Southern Hemisphere revealed by a high-resolution middle-atmosphere general circulation model. *Journal of the Atmospheric Sciences*, 69(4):1378–1396, 2012.
- M. R. Schoeberl. The penetration of mountain waves into the middle atmosphere. *Journal of the atmospheric sciences*, 42(24):2856–2864, 1985.

- U. Schumann. The horizontal spectrum of vertical velocities near the tropopause from global to gravity wave scales. *Journal of the Atmospheric Sciences*, 76(12):3847–3862, 2019.
- R. Sedlak, A. Zuhr, C. Schmidt, S. Wüst, M. Bittner, G. G. Didebulidze, and C. Price. Intra-annual variations of spectrally resolved gravity wave activity in the upper mesosphere/lower thermosphere (UMLT) region. *Atmospheric Measurement Techniques*, 13(9):5117–5128, 2020.
- R. B. Smith, A. D. Nugent, C. G. Kruse, D. C. Fritts, J. D. Doyle, S. D. Eckermann, M. J. Taylor, A. Dörnbrack, M. Uddstrom, W. Cooper, et al. Stratospheric gravity wave fluxes and scales during DEEPWAVE. *Journal of the Atmospheric Sciences*, 73(7):2851–2869, 2016.
- S. Smith, J. Baumgardner, and M. Mendillo. Evidence of mesospheric gravity-waves generated by orographic forcing in the troposphere. *Geophysical Research Letters*, 36(8), 2009.
- S. A. Smith, D. C. Fritts, and T. E. Vanzandt. Evidence for a saturated spectrum of atmospheric gravity waves. *Journal of the Atmospheric Sciences*, 44(10):1404–1410, 1987.
- G. Stober, V. Matthias, C. Jacobi, S. Wilhelm, J. Höffner, and J. L. Chau. Exceptionally strong summer-like zonal wind reversal in the upper mesosphere during winter 2015/16. In *Annales Geophysicae*, volume 35, pages 711–720. Copernicus GmbH, 2017.
- I. Strelnikova, M. Almowafy, G. Baumgarten, K. Baumgarten, M. Ern, M. Gerding, and F.-J. Lübken. Seasonal Cycle of Gravity Wave Potential Energy Densities from Lidar and Satellite Observations at 54° and 69° N. *Journal of the Atmospheric Sciences*, 78(4):1359–1386, 2021.
- S. H. Strogatz. *Nonlinear dynamics and chaos*. 1996.
- W. G. Stroud, W. Nordberg, W. R. Bandeen, F. L. Bartman, and P. Titus. Rocket-grenade measurements of temperatures and winds in the mesosphere over Churchill, Canada. *Journal of Geophysical Research*, 65(8):2307–2323, 1960.
- C. Strube, M. Ern, P. Preusse, and M. Riese. Removing spurious inertial instability signals from gravity wave temperature perturbations using spectral filtering methods. *Atmospheric measurement techniques*, 13(9):4927–4945, 2020.
- E. H. Synge. XCI. A method of investigating the higher atmosphere. *The London, Edinburgh, and Dublin Philosophical Magazine and Journal of Science*, 9(60):1014–1020, 1930.
- M. J. Taylor and M. A. Hapgood. Identification of a thunderstorm as a source of short period gravity waves in the upper atmospheric nightglow emissions. *Planetary and space science*, 36(10):975–985, 1988.

- L. Teisserenc de Bort. Résultats des ascensions des trois ballons-sondes lancés à Trappes le 8 juin. *Comptes rendus de l'Académie des sciences*, pages 135–138, 1898.
- M. A. C. Teixeira. The physics of orographic gravity wave drag. *Frontiers in Physics*, 2: 43, 2014.
- C. Torrence and G. P. Compo. A Practical Guide to Wavelet Analysis. *Bulletin of the American Meteorological Society*, 79(1):61–78, 1998. doi: 10.1175/1520-0477(1998)079<0061:APGTWA>2.0.CO;2. URL [http://dx.doi.org/10.1175/1520-0477\(1998\)079<0061:APGTWA>2.0.CO;2](http://dx.doi.org/10.1175/1520-0477(1998)079<0061:APGTWA>2.0.CO;2).
- B. Torrèsani. Analyse continue par ondelettes. Éditions du CNRS. *EDP sciences*, 1995.
- M. A. Tuve, E. A. Johnson, and O. R. Wulf. A new experimental method for study of the upper atmosphere. *Terrestrial Magnetism and Atmospheric Electricity*, 40(4):452–454, 1935.
- S. L. Vadas and E. Becker. Numerical modeling of the generation of tertiary gravity waves in the mesosphere and thermosphere during strong mountain wave events over the Southern Andes. *Journal of Geophysical Research: Space Physics*, 124(9):7687–7718, 2019.
- S. L. Vadas, J. Zhao, X. Chu, and E. Becker. The excitation of secondary gravity waves from local body forces: Theory and observation. *Journal of Geophysical Research: Atmospheres*, 123(17):9296–9325, 2018.
- H. Volland. *Atmospheric Tidal and Planetary Waves*, volume 12. Springer Science & Business Media, 1988.
- U. von Zahn and J. Höffner. Mesopause temperature profiling by potassium lidar. *Geophysical Research Letters*, 23(2):141–144, 1996.
- U. Von Zahn, G. Von Cossart, J. Fiedler, K. H. Fricke, G. Nelke, G. Baumgarten, D. Rees, A. Hauchecorne, and K. Adolfsen. The ALOMAR Rayleigh/Mie/Raman lidar: objectives, configuration, and performance. In *Annales Geophysicae*, volume 18, pages 815–833. Copernicus GmbH, 2000.
- G. Walker. *An Ocean of Air: Why the Wind Blows and Other Mysteries of the Atmosphere*. Houghton Mifflin Harcourt, 2008.
- J. M. Wallace and P. V. Hobbs. *Atmospheric science: an introductory survey*, volume 92. Elsevier, 2006.
- J. W. Waters, K. F. Kunzi, R. L. Pettyjohn, R. K. L. Poon, and D. H. Staelin. Remote sensing of atmospheric temperature profiles with the Nimbus 5 microwave spectrometer. *Journal of Atmospheric Sciences*, 32(10):1953–1969, 1975.
- D. W. Waugh, A. H. Sobel, and L. M. Polvani. What is the polar vortex and how does it influence weather? *Bulletin of the American Meteorological Society*, 98(1):37–44, 2017.

- C. Weitkamp. *Lidar: range-resolved optical remote sensing of the atmosphere*, volume 102. Springer Science & Business, 2006.
- J. A. Whiteway and A. I. Carswell. Lidar observations of gravity wave activity in the upper stratosphere over Toronto. *Journal of Geophysical Research: Atmospheres*, 100(D7):14113–14124, 1995.
- J. A. Whiteway, T. J. Duck, D. P. Donovan, J. C. Bird, S. R. Pal, and A. I. Carswell. Measurements of gravity wave activity within and around the Arctic stratospheric vortex. *Geophysical research letters*, 24(11):1387–1390, 1997.
- R. Wilson, M. L. Chanin, and A. Hauchecorne. Gravity waves in the middle atmosphere observed by Rayleigh lidar: 2. Climatology. *Journal of Geophysical Research: Atmospheres*, 96(D3):5169–5183, 1991. doi: 10.1029/90JD02610. URL <https://agupubs.onlinelibrary.wiley.com/doi/abs/10.1029/90JD02610>.
- M. Wirth, A. Fix, P. Mahnke, H. Schwarzer, F. Schrandt, and G. Ehret. The airborne multi-wavelength water vapor differential absorption lidar WALES: system design and performance. *Applied Physics B*, 96(1):201–213, 2009.
- C. J. Wright, S. M. Osprey, and J. C. Gille. Global observations of gravity wave intermittency and its impact on the observed momentum flux morphology. *Journal of Geophysical Research: Atmospheres*, 118(19):10–980, 2013.
- C. J. Wright, N. P. Hindley, A. C. Moss, and N. J. Mitchell. Multi-instrument gravity-wave measurements over Tierra del Fuego and the Drake Passage—Part 1: Potential energies and vertical wavelengths from AIRS, COSMIC, HIRDLS, MLS-Aura, SAAMER, SABER and radiosondes. *Meas. Tech*, 9:877–908, 2016.
- C. J. Wright, N. P. Hindley, L. Hoffmann, M. J. Alexander, and N. J. Mitchell. Exploring gravity wave characteristics in 3-D using a novel S-transform technique: AIRS/Aqua measurements over the Southern Andes and Drake Passage. *Atmospheric chemistry and physics*, 17(13):8553–8575, 2017.
- C. Yamashita, X. Chu, H.-L. Liu, P. J. Espy, G. J. Nott, and W. Huang. Stratospheric gravity wave characteristics and seasonal variations observed by lidar at the South Pole and Rothera, Antarctica. *Journal of Geophysical Research: Atmospheres*, 114(D12), 2009.
- Y. Yamazaki, V. Matthias, Y. Miyoshi, C. Stolle, T. Siddiqui, G. Kervalishvili, J. Laštovička, M. Kozubek, W. Ward, D. R. Themens, et al. September 2019 Antarctic Sudden Stratospheric Warming: Quasi-6-Day Wave Burst and Ionospheric Effects. *Geophysical Research Letters*, 47(1):e2019GL086577, 2020.
- X. Yan, N. Arnold, and J. Remedios. Global observations of gravity waves from High Resolution Dynamics Limb Sounder temperature measurements: A yearlong record of temperature amplitude and vertical wavelength. *Journal of Geophysical Research: Atmospheres*, 115(D10), 2010.

- T. Yuan, C. J. Heale, J. B. Snively, X. Cai, P.-D. Pautet, C. Fish, Y. Zhao, M. J. Taylor, W. R. Pendleton Jr, V. Wickwar, et al. Evidence of dispersion and refraction of a spectrally broad gravity wave packet in the mesopause region observed by the Na lidar and Mesospheric Temperature Mapper above Logan, Utah. *Journal of Geophysical Research: Atmospheres*, 121(2):579–594, 2016.
- T. Yuan, S. C. Solomon, C.-Y. She, D. A. Krüeger, and H.-L. Liu. The long-term trends of nocturnal mesopause temperature and altitude revealed by Na lidar observations between 1990 and 2018 at midlatitude. *Journal of Geophysical Research: Atmospheres*, 124(12):5970–5980, 2019.
- J. Yue, S. D. Miller, L. Hoffmann, and W. C. Straka III. Stratospheric and mesospheric concentric gravity waves over tropical cyclone Mahasen: Joint AIRS and VIIRS satellite observations. *Journal of atmospheric and solar-terrestrial physics*, 119:83–90, 2014.
- W. Zdunkowski, T. Trautmann, and A. Bott. *Radiation in the Atmosphere - A Course in Theoretical Meteorology*. Cambridge University Press, Cambridge, 2007. ISBN 978-1-139-46460-4.
- R. E. Zeebe, A. Ridgwell, and J. C. Zachos. Anthropogenic carbon release rate unprecedented during the past 66 million years. *Nature Geoscience*, 9(4):325–329, 2016.
- Y. Zhang, Z. Sheng, H. Shi, S. Zhou, W. Shi, H. Du, and Z. Fan. Properties of the long-term oscillations in the middle atmosphere based on observations from TIMED/SABER instrument and FPI over Kelan. *Atmosphere*, 8(1):7, 2017.
- J. Zhao, X. Chu, C. Chen, X. Lu, W. Fong, Z. Yu, R. Michael Jones, B. R. Roberts, and A. Dörnbrack. Lidar observations of stratospheric gravity waves from 2011 to 2015 at McMurdo (77.84° S, 166.69° E), Antarctica: 1. Vertical wavelengths, periods, and frequency and vertical wave number spectra. *Journal of Geophysical Research: Atmospheres*, 122(10):5041–5062, 2017.
- Y. Zhao, M. J. Taylor, H.-L. Liu, and R. G. Roble. Seasonal oscillations in mesospheric temperatures at low-latitudes. *Journal of atmospheric and solar-terrestrial physics*, 69(17-18):2367–2378, 2007.

Acknowledgement

“If I have seen further it is by standing on the shoulders of Giants.” - Isaac Newton (1675)

I would like to echo this and thank my very own giants on whose shoulders I stand. Thank you, Markus Rapp, for getting me enthusiastic about gravity waves in the first place. I am very grateful that you gave me the opportunities to attend international conferences like the American and European Geoscience Unions and to do exciting trips to places like Kühlungsborn, Kiruna, São José dos Campos or to the end of the world, Río Grande. I would like to take this opportunity to thank the team at the EARG in Río Grande, where we installed CORAL, for their kind cooperation and noble hospitality. Without Bernd and Natalie Kaifler, the head and heart of CORAL, this work would never have been written. I truly appreciate that you have entrusted me with what I consider to be a genuinely unique data set. Thank you for your valuable time that you always invested in correcting my work. I assume it has not always been easy. Furthermore, I would like to thank the “Middle Atmosphere” matrix group at the IPA in Oberpfaffenhofen for countless discussions with colleagues such as Thomas Birner, Andreas Dörnbrack, Hella Garny, Sonja Gisinger, Stefanie Knobloch, Tyler Mixa and Henrike Willms. Thank you, Andreas, for taking me under your wings more and more during the course of my doctoral studies. I often felt like a writer visiting Gertrude Stein in her salon to have a conversation about his work. I am much obliged for the superb working atmosphere in the Lidar department and numerous discussions in the coffee kitchen with colleagues like Andreas Fix, Florian Ewald and Eleni Marinou. Exclusive thanks go to the so-called Lidar Justice League, which is composed of my (former) office colleagues, Quitterie Cazenave, Manuel Gutleben, Benedikt Urbanek and Sebastian Wolff. I remember many days, when the mood was fantastic in the office and we were drinking coffee, discussing latest news and rating others plots. Memories that are unfortunately already far too distant. I am grateful for fruitful discussions within the MS-GWaves community. Thanks to my colleagues from Jülich Forschungszentrum Markus Geldenhuys, Lukas Krasauskas, Peter Preusse and Sebastian Rhode who performed for me the GROGRAT runs. My final professional "thank you" goes to Dominique Pautet and Mike Taylor for assisting me with airglow data analysis, my former physics teacher, Stefan Rauscher and Felix Götde, who did not let up in trying to persuade me to attend Markus Rapp's LMU lecture on the middle atmosphere.

My emotional thanks go to my family, of course. Even though I rarely give the impression that I need help, I am grateful that I can always rely on you. I would also like to thank two other families who have given me a lot of stability and who have influenced me: The Steinbauer family and the Fischbacher family. Last but not least, thank you Sarah for accompanying me on this journey through life. You are my perfect match.

I hope one day to be a giant myself for future generations.